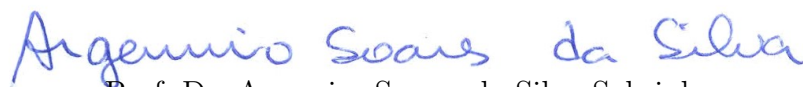


Dissertation presented to the Instituto Tecnológico de Aeronáutica, in partial fulfillment of the requirements for the degree of Master of Science in the Graduate Program of Física, Field of Física dos Plasmas.

**Lauren de Carvalho Leme**

**DEPOSITION AND CHARACTERIZATION OF  
AIN THIN FILMS FOR APPLICATION IN SAW  
DEVICES**

Dissertation approved in its final version by signatories below:



Prof. Dr. Argemiro Soares da Silva Sobrinho  
Advisor

Prof. Dr. Pedro Teixeira Lacava  
Pro-Rector of Graduate Courses

Campo Montenegro  
São José dos Campos, SP - Brazil  
2019

**Cataloging-in Publication Data  
Documentation and Information Division**

Leme, Lauren de Carvalho

Deposition and Characterization of AlN Thin Films for Application in SAW Devices / Lauren de Carvalho Leme.

São José dos Campos, 2019.

95f.

Dissertation of Master of Science – Course of Física. Area of Física dos Plasmas – Instituto Tecnológico de Aeronáutica, 2019. Advisor: Prof. Dr. Argemiro Soares da Silva Sobrinho.

1. Dispositivos de ondas acústicas superficiais. 2. Filmes finos. 3. Microscopia eletrônica. 4. Pulverização por magnetron. 5. Física. I. Instituto Tecnológico de Aeronáutica. II. Deposition and Characterization of AlN Thin Films for Application in SAW Devices

**BIBLIOGRAPHIC REFERENCE**

LEME, Lauren de Carvalho. **Deposition and Characterization of AlN Thin Films for Application in SAW Devices**. 2019. 95f. Dissertation of Master of Science – Instituto Tecnológico de Aeronáutica, São José dos Campos.

**CESSION OF RIGHTS**

AUTHOR'S NAME: Lauren de Carvalho Leme

PUBLICATION TITLE: Deposition and Characterization of AlN Thin Films for Application in SAW Devices.

PUBLICATION KIND/YEAR: Dissertation / 2019

It is granted to Instituto Tecnológico de Aeronáutica permission to reproduce copies of this dissertation and to only loan or to sell copies for academic and scientific purposes. The author reserves other publication rights and no part of this dissertation can be reproduced without the authorization of the author.

---

Lauren de Carvalho Leme  
Av. Campos Floridos, 810  
12.224-853 – São José dos Campos–SP

# DEPOSITION AND CHARACTERIZATION OF AIN THIN FILMS FOR APPLICATION IN SAW DEVICES

**Lauren de Carvalho Leme**

Thesis Committee Composition:

Prof. Dr. Gilberto Petraconi Filho	President	-	ITA
Prof. Dr. Argemiro Soares da Silva Sobrinho	Advisor	-	ITA
Prof. Dr. Douglas Marcel Gonçalves Leite	Intern Member	-	ITA
Prof. Dr. Marcos Massi	External Member	-	Mackenzie

À minha família.

Aos meus pais Joaquim e Odete.

A minha irmã Júlia.

Ao meu namorado Alefe.

# Acknowledgments

O mestrado me trouxe mais que conhecimentos, me trouxe oportunidades, amigos e uma nova família. De fato, eu não conseguiria obter êxito nessa jornada se não tivesse pessoas especiais ao meu lado, as quais dedico não só este trabalho, mas também meu respeito, carinho e admiração.

Ao meu orientador Prof. Dr. Argemiro Soares da Silva Sobrinho, por me acolher nesse desafio, por me nortear e contribuir imensamente nesse trabalho. Pelos conselhos, conversas, decisões, ensinamentos que fortaleceram o meu saber e por sempre me fazer acreditar na pesquisa. Pela confiança a mim depositada e pela incansável dedicação.

Ao Prof. Dr. Douglas Marcel Gonçalves Leite, por toda colaboração a este trabalho e por compartilhar suas experiências e sugestões para que este pudesse ter forma e sentido. Ao Prof. Dr. Gilberto Petraconi e Prof. Dr. Jayr Amorim pelos ensinamentos sobre descargas elétricas e plasmas.

À Dr.<sup>a</sup> Cristiane Stegemann e MSc. Flávia Pereira da Rocha por toda ajuda, incentivo e por contribuir tanto a este trabalho. Agradeço imensamente vocês, minhas amigas, que me apoiaram, sem dúvidas esse trabalho é nosso.

Ao Instituto Tecnológico de Aeronáutica (ITA) e ao Laboratório Plasmal por me acolherem como aluna. Aos amigos que ali formei que de alguma forma sempre me incentivaram. Aproveito agradecer ao LabMat pela infraestrutura e dedicação dos seus alunos para com as análises apresentadas nesse trabalho.

Ao Centro de Competência em Manufatura (CCM), família que me acolheu em meio a essa jornada, por todas as oportunidades a mim ofertadas, por acreditarem e confiarem em meu trabalho. Aos meus amigos que ali fiz, que não só agregaram em conhecimento no desenvolvimento desse trabalho, mas também me surpotaram, no sentido literal da palavra quando eu mais precisei deles. Em especial ao Grupo GMB: Pedro Teruel, Fábio Sena, Matheus Gomes, Guilherme Santos, Kalvin Sanches, Givan Macedo, Júlia Gil e André Schwanz. Em especial Wesley Poletto e MSc. Paula Montenegro pelas análises, revisões e sugestões para o desenvolvimento dessa pesquisa. À Janete Moreira por sua atenção e cuidado em todos os momentos.

---

Aos professores do CCM, Prof. Dr. Anderson Borille, Prof. Dr. Jefferson Gomes e Prof. Dr. Ronnie Rego, que me permitiram fazer parte dessa família e sempre me desafiaram, acreditando na minha pesquisa e reconhecendo meu trabalho.

Às minhas amigas não só de pesquisa e trabalho, mas de alma, que me apoiaram e incentivaram: Adriana Nunes, Carla Cunha, Corina Paiva e Nathianne Andrade. Em especial minha amiga-irmã, Natália D'Ávila, a qual devo onde estou, minha companheira de jornada, que deixou esse desafio muito mais fácil e feliz, a qual eu recorri quando mais precisei e sempre esteve disposta a me ajudar em tudo, acreditou junto a mim e me mostrou que o mundo é maior que eu imaginava. A vocês meninas todo meu amor.

Às minhas famílias, Carvalho, Leme e Peçanha, que são minha essência, os quais me ensinaram grandes princípios, me mostraram que só com a educação podemos fazer a diferença e sempre torceram por todas minhas conquistas. Aos meus bebês que são minha alegria João Lucas, Anna Sophia, Davi, Pedro, Lucas e Gustavo.

Ao meu namorado Alefe Fazio, meu maior incentivador para realizar a concretização desse mestrado, que cedeu sua cidade, São José dos Campos, para ser a nossa cidade. À essa pessoa maravilhosa, meu porto-seguro que me traz alegrias e sabe me fazer bem de um jeito único. À ele que esteve em todos os momentos ao meu lado, sempre foi compreensivo e me ajudou incansavelmente. Amo você meu amor.

Aos meus pais, José Joaquim Peçanha da Silva Leme e Odete Aparecida de Carvalho Leme, a minha irmã Júlia de Carvalho Leme, que durante esse período compreenderam minha ausência, mas sempre estiveram do meu lado, apoiando e torcendo por cada conquista. À eles que me deram mais do que educação, me deram princípios e fé, acreditaram quando eu desacreditei e jamais me deixaram desistir. À eles que me mostraram o valor da educação e dedicação, mas também me atentaram da incerteza do sucesso e ainda sim estiveram sempre em prontidão para ser meu esteio. À eles que tudo sou e tudo devo, à eles que dedico todas minhas conquistas e minha vida. Meus eternos amores, amo vocês incondicionalmente.

À DEUS pelo dom da vida, pela oportunidade de concretização de mais uma etapa e por ter me dado uma ótima família e grandes amigos.

À CAPES (Coordenação de Pessoal de Nível Superior) pela concessão da bolsa durante o período de realização deste mestrado.

*“Liberte as mariposas que dominam seu estômago,  
mas deixe seus casulos para que um dia  
borboletas possam deles fazer morada.”*

— CARLA CUNHA

# Abstract

The present work reports the growth of aluminum nitride (AlN) thin film aiming its application in the manufacturing of microsensors devices based on surface acoustic waves (SAW). The AlN thin films were deposited on p-type silicon (100) substrate by radio frequency magnetron sputtering technique. The plasma parameters were varied in order to investigate the best plasma conditions to growth AlN thin films for application in SAW devices. The parameters explored were residual pressure, nitrogen concentration and applied RF power. These parameters had strong influence in the structure and composition of the deposited AlN films. The deposition rate and morphology were characterized by mechanical and optical profilometries and the field emission gun scanning electron microscopy, respectively. The deposition rate linearly increases with the increase of the RF power up to about 240W. For higher RF power the deposition rate presents a less accentuated increase probably due to the retro-sputtering of the growing film caused by the high energetic species impinging the film surface. High nitrogen content (100%) in the gas mixture decreases the deposition rate by about 50% due to the target poisoning and the absence of argon. The crystalline structures of the deposited AlN thin films were analyzed by X-ray diffraction, Raman spectroscopy and variable angle spectroscopic ellipsometry. The film crystallinity and composition are tightly influenced by the residual pressure in the deposition chamber due to the elevated concentration of impurities, mainly oxygen. The increase of the applied RF power favors the growth of well oriented h-(002) hexagonal wurtzite type structure. The refractive index values obtained are in good agreement with the values described in the literature and the values increase with the improvement of the AlN crystallinity, that occurs with the increasing of the applied RF power. The bandgap energies values obtained by ellipsometry was slightly low compared with the bandgap energy values obtained by the Tauc-Lorentz method that is closer to the values cited in the literature. This difference was caused by the lack of good mathematical and/or geometrical model fit. The AlN film with the best set of properties for SAW application was grown with lower residual pressure in the plasma chamber, gas mixture containing 70% of N<sub>2</sub> and an RF power of 240W.

# Resumo

Neste trabalho descreve-se o crescimento do filme fino de nitreto de alumínio (AlN) visando sua aplicação na fabricação de dispositivos de microsensors baseados em ondas acústicas de superfície (SAW). Os dispositivos de SAW com boa qualidade e alta sensibilidade requerem filmes finos de AlN com elevadas propriedades piezoelétricas. Os filmes de AlN foram depositados em substrato de silício (100) do tipo-p pela técnica de magnetron sputtering de rádio-frequência. Os parâmetros de deposição foram variados para investigar a melhor condição do plasma para o crescimento de filmes finos de AlN com alta qualidade. Os parâmetros explorados foram pressão residual, concentração de nitrogênio e potência de RF aplicada, estes tiveram forte influência na estrutura e composição dos filmes de AlN depositados. A taxa de deposição e a morfologia de filmes finos de AlN foram caracterizadas por meio de perfilometria óptica e mecânica e microscopia eletrônica de varredura de alta resolução MEV-FEG, respectivamente. A taxa de deposição aumenta linearmente com a elevação da potência de RF até cerca de 240W. Para potências de RF maiores, a taxa de deposição apresentou um aumento menos acentuado devido ao re-sputtering do filme em crescimento causado pelas espécies altamente energéticas colidiram com a superfície do filme. O alto teor de nitrogênio (100%) na mistura de gases diminui a taxa de deposição em cerca de 50% devido ao envenenamento do alvo e a ausência de argônio. As estruturas cristalinas dos filmes finos de AlN depositados foram analisadas por difração de raio X, espectroscopia Raman e elipsometria espectroscópica de ângulo variável. A cristalinidade dos filmes foi afetada pela pressão residual devido à elevada concentração de impurezas, principalmente oxigênio. O aumento da potência de RF aplicada favorece o crescimento de estrutura do tipo wurtzita hexagonal bem orientada h-(002). Os valores do índice de refração obtidos estão alinhados com os valores descritos na literatura e estes aumentam com a cristalinidade do AlN, que ocorre com o aumento da potência de RF aplicada. Os valores de energia bandgap obtidos por elipsometria foram ligeiramente baixos em comparação com os valores de energia bandgap obtidos pelo método de Tauc-Lorentz, os quais estão mais próximos dos valores citados na literatura. Essa diferença está associada à falta de ajuste do modelo matemático e/ou geométrico utilizado. O filme de AlN com o melhor conjunto de propriedades para aplicação SAW foi desenvolvido com menor pressão residual, mistura de gás contendo 70% N<sub>2</sub> e uma potência de RF de 240W.

# List of Figures

FIGURE 1.1 – Basic sensor operation. (COVACEVICE, 2012) . . . . .	23
FIGURE 1.2 – Numbers of science publication with the topics "aluminum nitride", "surface acoustic waves sensor" and "AlN for SAW sensor applica- tion". (SCIENCEDIRECT, 2018) . . . . .	24
FIGURE 2.1 – XRD diffractograms of AlN films deposited at 200 W DC and gas flow rate $N_2 : Ar$ (a) 30:10 sccm and (b) 20:20 sccm. (ALRASHDAN <i>et al.</i> , 2014) . . . . .	27
FIGURE 2.2 – (a)Effect of the nitrogen contents on the AlN thin film structure. (b) Evolution of the FWHM Raman mode $E_2$ (open circles) and the IR mode of vibration $E_1$ (TO) of aluminum nitride (bold circle) versus $R = N_2/(Ar + N_2)$ . (DUQUENNE <i>et al.</i> , 2007) . . . . .	28
FIGURE 2.3 – XRD spectra of AlN films prepared at various nitrogen condition. (KHAN <i>et al.</i> , 2015) . . . . .	29
FIGURE 2.4 – Influence of substrate temperature on the refractive index. (KHAN <i>et al.</i> , 2015) . . . . .	30
FIGURE 2.5 – The XRD patterns of AlN (a) at different sputtering pressures ( $N_2$ 50%, power 50 W, distance D 40 mm); (b) at different target powers ( $N_2$ 50%, sputtering pressure 0.3 Pa (2.25 mTorr), distance D 40 mm). (XU <i>et al.</i> , 2001) . . . . .	31
FIGURE 2.6 – Orientation diagram of AlN films under various sputtering pressures and distances D. (XU <i>et al.</i> , 2001) . . . . .	31
FIGURE 2.7 – (a)Film thickness of AlN films versus applied DC power; (b) GIXRD diffractograms of the deposited film prepared at different DC power; (a) 100W, (b) 200W, (c) 300W and (d) 400W. (KUMARI <i>et al.</i> , 2014)	32
FIGURE 2.8 – (a)XRD patterns of the AlN thin films; (b) Room temperature Ra- man spectra of AlN thin films. (AISSA <i>et al.</i> , 2015) . . . . .	33

FIGURE 2.9 – (a) Scanning electron microscopy image of the cross-section of a typical AlN film used in this study; (b) Raman spectrum of a typical c-axis textured AlN film on silicon (100). The inset shows an enlarged view of the spectral region where the $E_2^{high}$ optical phonon of AlN is visible for three selected samples. The FWHM is also indicated. (LUGHI; CLARKE, 2006) . . . . .	34
FIGURE 2.10 – (a) XRD diffractograms of AlN films deposited (a) at 0.5 Pa (3.75 mTorr) and different RF power; (b) at 150 W for different deposition pressure. (ZHANG; CHEN, 2013) . . . . .	35
FIGURE 2.11 – (a) The XRD results of the AlN films deposited at different N <sub>2</sub> :r ratio; (b) The EDX spectra of the AlN film deposited at the optimized process. (ZHANG; CHEN, 2013) . . . . .	36
FIGURE 2.12 – The morphology of the AlN film deposited at the optimized process, (a) the surface, (b) the cross-view. (ZHANG; CHEN, 2013) . . . . .	36
FIGURE 2.13 – Spectroscopic ellipsometry angles measured (open circle) and calculated from the best-fit model (solid curves). (JOO <i>et al.</i> , 2000) . . . . .	37
FIGURE 2.14 – Typical refractive index curves for the AlN thin films obtained from the best-fit parameters in Table 2.1. (JOO <i>et al.</i> , 2000) . . . . .	38
FIGURE 2.15 – SEM micrographs of AlN films deposited on SiO <sub>2</sub> /Si at different Ar/N <sub>2</sub> partial pressures: (a) 0.8:0.3 Pa (6:2 mTorr) and (b) 1:0.3 Pa (8:2 mTorr). (JOO <i>et al.</i> , 2000) . . . . .	39
FIGURE 2.16 – XRD Diffractograms of AlN films in function of applied power, fixing the values P=0.27 Pa (2mTorr) and d=50mm. (BRITO, 2014) . . . . .	40
FIGURE 2.17 – Room-temperature Raman spectra of the AlN films grown on different substrate materials. All spectra were taken under the same geometry. (OLIVEIRA <i>et al.</i> , 2001) . . . . .	41
FIGURE 3.1 – Periodic classification of the elements and the formation of nitrides and semiconductors of wide gap. Adapted from (PIERSON, 1996) . . . . .	43
FIGURE 3.2 – Schematic representation of the crystal structure of aluminum nitride. a) Tetrahedron formed by one atom of Al and four of N; b) Unit cell forming the Wurtzite structure of AlN. (RODRÍGUEZ-CLEMENTE <i>et al.</i> , 1993) . . . . .	45
FIGURE 3.3 – Hexagonal wurtzite structure of aluminum nitride. (FU <i>et al.</i> , 2017) . . . . .	46
FIGURE 3.4 – Planes for the hexagonal wurtzite structure. (MOURA, 2010) . . . . .	46

FIGURE 3.5 – Bandgap energy versus network parameters. (MOURA, 2010) . . . . .	50
FIGURE 3.6 – Mechanism of piezoelectric effect in quartz. (GUPTA <i>et al.</i> , 2014) . . .	51
FIGURE 3.7 – Schematic of the dipole distribution along a piezoelectric net: (a) grains aligned in various directions and (b) grains aligned along the same direction. (LÓPEZ, 2016) . . . . .	51
FIGURE 3.8 – Surface acoustic waves sensor. (WHITE; VOLTMER, 1965) . . . . .	52
FIGURE 4.1 – Methodology diagram. . . . .	54
FIGURE 4.2 – (a) Magnetron sputtering system used to deposit AlN thin films. (b) Schematic drawing of the vacuum chamber with its main constituent parts. (BRITO, 2014) . . . . .	55
FIGURE 4.3 – Contributions of the materials' structure to the line broadening of diffraction profiles. (NOYAN; COHEN, 1987) Adapted from (RO-BATTO, 2017) . . . . .	59
FIGURE 4.4 – The convolution of a Gaussian function (dash-dot line) and Lorentzian (dashed line) provide a Voigt function (continuous function). (ICHIKAWA, 2013) . . . . .	60
FIGURE 4.5 – Raman spectra (a) mainly characteristics; (b) with peaks shifted and the correlation with the residual stress. (NANOPHOTON, 2018) . . . . .	62
FIGURE 4.6 – Identification of crystal polymorphs. (NANOPHOTON, 2018) . . . . .	62
FIGURE 4.7 – Spectroscopic ellipsometry methodology. Adapted from (HORIBA, 2008) . . . . .	63
FIGURE 5.1 – Sample heating rate during the deposition process. The heating was caused only by the plasma process. . . . .	66
FIGURE 5.2 – Images of the sample profiles obtained by CAM. . . . .	67
FIGURE 5.3 – Thickness samples as function of the nitrogen content in the gas mixture. . . . .	68
FIGURE 5.4 – Thickness of the samples deposited with 70% N <sub>2</sub> as function of the applied RF power. . . . .	69
FIGURE 5.5 – XRD diffractograms for all deposited AlN thin films. . . . .	71
FIGURE 5.6 – Diffractogram of the type-p Si (100) used as substrate to growth AlN thin films. . . . .	72

---

FIGURE 5.7 – Micrographies of sample S200-N70-P5 deposited AlN thin films in 200W with 70% N <sub>2</sub> and high residual pressure (10 <sup>-5</sup> Torr). . . . .	73
FIGURE 5.8 – Micrographies of samples deposited AlN thin films (a) S200-N70-P6 deposited with 200W and (b) S240-N70-P6 deposited with 240W in a zoom in 1 μm, 500 nm and 200 nm. . . . .	76
FIGURE 5.9 – Raman spectra of the aluminum nitride films varying deposition parameters, such as residual, initial temperature, nitrogen concentration and RF power. . . . .	78
FIGURE 5.10 –Structural model applied in the spectroscopy of ellipsometry for samples (a)S200-N100-P6 to S240-N70-P6; (b) S300-N70-P6. . . . .	80
FIGURE 5.11 –Spectroscopic ellipsometry experimental data measured I <sub>s</sub> (blue symbols) and I <sub>c</sub> (red symbols) with the curve fit (lines) versus the energy for the AlN films of samples S200-N100-P6 to S300-N70-P6. . . . .	82
FIGURE 5.12 –Thickness comparison between profilometry and ellipsometry technique. . . . .	84
FIGURE 5.13 –Bandgap energy analyzing through the ellipsometry and the Tauc-Lorentz method. . . . .	84
FIGURE 5.14 –Refractive index (n) versus the wavelength for the AlN films of samples S200-N100-P6 to S300-N70-P6. . . . .	85

# List of Tables

TABLE 2.1 – Best-fit model parameters of AlN thin films. (JOO <i>et al.</i> , 2000) . . .	37
TABLE 3.1 – Ionicity Phillips ( $f_i$ ), Pauling ( $f_i^P$ ) e Harrison ( $f_i^H$ )for the semiconductor nitrides. (ADACHI, 2005) . . . . .	46
TABLE 3.2 – Crystal structure, space group, lattice constants $a$ and $c$ (T = 300K) for semiconductor nitrides; d = diamond, zb = blende, h = hexagonal, w = wurtzitic and rs = cubic. (ADACHI, 2005) . . . . .	47
TABLE 3.3 – Cleavage planes for various crystal structures of group III-V. (ADACHI, 2005) . . . . .	47
TABLE 3.4 – Melting point, specific heat and Debye temperature for semiconductor nitrides. (ADACHI, 2005) . . . . .	48
TABLE 3.5 – Thermal conductivity for semiconductor nitrides and other materials of interest. (QUAY, 2007) . . . . .	49
TABLE 4.1 – Experimental parameters. . . . .	57
TABLE 5.1 – Thickness and roughness of AlN thin films by profilometry technique.	68
TABLE 5.2 – Peaks positions ( $\theta$ ), full width at half maximum ( $FWHM$ ), Gaussian convolution( $\beta_G^f$ ), Lorentz convolution ( $\beta_L^f$ ), crystallite size ( $C$ ), area under the peaks ( $A$ ), coating thickness ( $t$ ), $A/t$ ratio and intensity of microstrains ( $\varepsilon$ ) for all deposited samples, obtained from the XRD difratograms of Figure 5.5. . . . .	74
TABLE 5.3 – Raman reference values of the $E_2$ modes in $cm^{-1}$ . (MCNEIL <i>et al.</i> , 1993) The $E_2^{low}$ , $E_2^{high}$ and $FWHM(E_2^{high})$ from Raman spectra of the AlN film varying deposition parameters. . . . .	79
TABLE 5.4 – Ellipsometry data as thickness and roughness compared with profilometry techniques of the samples of AlN film varying deposition parameters. . . . .	81

---

TABLE 5.5 – Ellipsometry data from the spectra and mathematical model of the samples of AlN film varying deposition parameters. . . . .	83
---	----

# List of Abbreviations and Acronyms

CAM	Chromatic Aberration Microscopy
CCM	Centro de Competência em Manufatura
CVD	Chemical Vapor Deposition
DC	Direct Current
DCMS	DC Magnetron Sputtering
DIN	Deutsches Institut für Normung
EDX	Energy Dispersive X-Ray Spectroscopy
FEG	Field Emission Gun
FUV	Far Ultraviolet
FWHM	Full-Width Half Maximum
hcp	Hexagonal Close-Packed
HiPIMS	High-Power Impulse Magnetron Sputtering
IBD	Ion Beam Deposition
IDT	Inter-Digital Transducers
INPE	Instituto Nacional de Pesquisas Espaciais
IR	Infrared
ISO	International Organization for Standardization
ITA	Instituto Tecnológico de Aeronáutica
JCPDS	Joint Committee on Powder Diffraction Standards
LabMat	Laboratório de Materiais
LAS	Laboratório Associados de Sensores e Materiais
LPP	Laboratório de Plasmas e Processos
MBE	Molecular Beam Epitaxy
MEMS	Micro-Electro-Mechanical System
PEM	Photoelastic Modulator
PLD	Pulsed Laser Deposition
PME	Polarization Modulation Ellipsometer
PVD	Physical Vapour Deposition
RBS	Rutherford Backscattering Spectroscopy
RF	Radio-Frequency

---

RMS	Reactive Magnetron Sputtering
RS	Raman Spectroscopy
SAW	Surface Acoustic Waves
SE	Spectroscopic Ellipsometry
SEM	Scanning Electronic Microscopy
SIMS	Secondary Ion Mass Spectroscopy
UHF	Ultra High Frequency
UV	Ultra-Violet
WBG	Wide Bandgap Semiconductor
XPS	X-Ray Photoelectron Spectroscopy
XRD	X-Ray Diffraction
zb	Zinc-Blend

# List of Symbols

$C_3H_6O$	Acetone
Al	Aluminum
AlN	Aluminum Nitride
$Al_2O_3$	Aluminum Oxide
$Al_2OC$	Aluminum Oxycarbide
$\psi$	Amplitude Ratio
Å	Angstrom
Ar	Argon
C	Carbon
$^{\circ}C$	Celsius
$f_h^{\alpha}$	Covalent Fraction
$\theta_D$	Debye Temperature
$^{\circ}$	Degree
$\theta$	Diffraction angle
$k_t^2$	Electromechanical Coupling Coefficient
eV	Electronvolt
$E_g$	Energy Bandgap
$\chi$	Error
HF	Fluoride Acid
GaN	Gallium Nitride
$H_2O_2$	Hydrogen Peroxide
$f_i^{\alpha}$	Ionic Fraction
$f_i^H$	Ionicity Harrison
$f_i^P$	Ionicity Pauling
$f_i$	Ionicity Phillips
$C_3H_8O$	Isopropyl Alcohol
K	Kelvin
$LiNbO_3$	Lithium Niobate
$T_m$	Melting Temperature
$\varepsilon$	Microstrains

---

nm	Nanometer
N	Nitrogen
$\Omega$	Ohm
O	Oxygen
Pa	Pascal
%	Percentage
$\Delta$	Phase Difference
$d_{33}$	Piezoelectric Coefficient
R	Range
n	Refractive Index
$R_q$	RMS Roughness
Si	Silicon
SiC	Silicon Carbide
SiCN	Silicon Carbide Nitride
$C_p$	Specific Heat
sccm	Standard Cubic Centimeters per Minute
$H_2SO_4$	Sulfuric Acid
W	Watts
$\lambda$	Wavelength
ZnO	Zinc Oxide

# Contents

1	INTRODUCTION . . . . .	22
1.1	Background . . . . .	22
1.2	Motivation for the Study . . . . .	24
1.3	Objectives . . . . .	25
1.3.1	Specific Objectives . . . . .	25
1.4	Outline . . . . .	25
2	LITERATURE REVIEW . . . . .	26
3	THEORETICAL FOUNDATIONS . . . . .	42
3.1	Nitride . . . . .	42
3.1.1	Semiconductors Nitrides . . . . .	44
3.1.2	Aluminum Nitride . . . . .	44
3.1.3	Piezoelectric Effect . . . . .	49
4	EXPERIMENTAL PROCEDURE . . . . .	53
4.1	Thin Films Deposition System . . . . .	53
4.2	Parameters for Thin Films Deposition of AlN . . . . .	56
4.3	Film Characterization Techniques . . . . .	57
5	RESULTS AND DISCUSSION . . . . .	65
5.1	Film Deposition and Thickness . . . . .	65
5.2	X-Ray Diffractometry . . . . .	70
5.3	Raman Spectroscopy . . . . .	77
5.4	Variable Angle Spectroscopic Ellipsometry - VASE . . . . .	80

CONTENTS	xxi
<hr/>	
6 CONCLUSIONS . . . . .	86
6.1 Future Directions . . . . .	87
BIBLIOGRAPHY . . . . .	88

# Chapter 1

## Introduction

In this chapter is presented the background, motivation, objectives and outline of this dissertation.

### 1.1 Background

Ever since mankind improved the knowledge about quantum mechanics, this promoted the development of interesting materials such as semiconductors. The semiconductor materials are important to technology development because they present an intermediate electrical conductivity between the insulator and conductor materials. In consequence of it, the microelectronic sector has boomed in recent years, mainly in the development of devices such as transistors and sensors. (DUARTE, 2010)

The high demand of the market for even more efficient and low-cost sensors has boosted the studies for the development of technologies for the application of accessible and high performance sensors. Sensors are devices capable of instantaneously monitoring actions, usually acting in a system detecting variations of physical, chemical or biological parameters, transforming and emitting the information captured in an electrical signal. These input and output processes are known as the transduction process, but the sensors may also have signal amplifiers that are responsible for the sensor's sensitivity. (KIRSCHNER, 2010) (COVACEVICE, 2012) This process can be illustrated in Figure 1.1.

The Surface Acoustic Waves (SAW) sensor devices have a differential for constituting a transmitter and responder. This characteristic makes the SAW sensor a self-sustaining, dispensing any power source. The SAW sensors are devices that work according to the interaction between acoustic waves propagation on the surface of piezoelectric materials with a physical and/or chemical quantity. (COVACEVICE, 2012)

The development of micro-electro-mechanical system (MEMS) devices is only possible

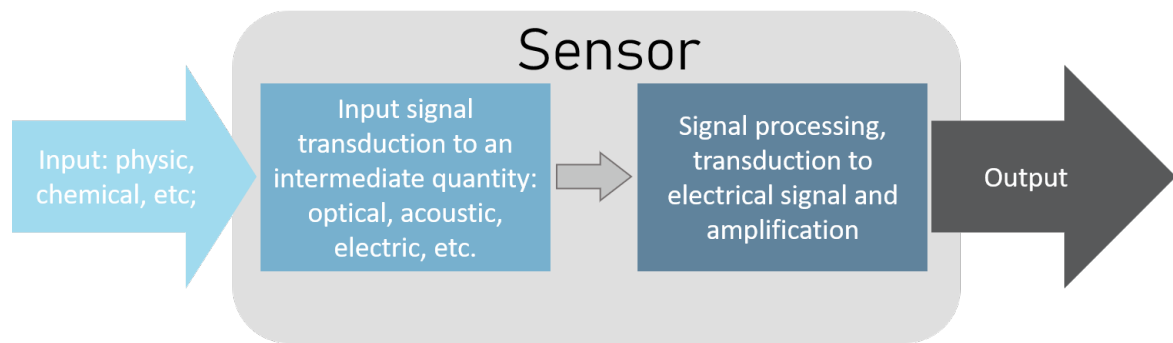


FIGURE 1.1 – Basic sensor operation. (COVACEVICE, 2012)

with the progress of sensors concept and the researches' advancement in semiconductors materials. Through these, the application of thin films contributed to the fabrication of SAW sensors in MEMS. Thin film piezoelectric materials for MEMS application contributed to improve the sensibility of sensors with wide dynamic ranges, the low power requirement, low hysteresis and also this technology is offered with a low-cost production innovation. Among the wide range of elements used for obtaining thin films, Si, C, N and Al have been highlighted in the sensor development, forming thin films of AlN, SiC and SiCN. (TROLIER-MCKINSTRY; MURALT, 2004)

The thin films of aluminum nitride play key roles in the microelectronic field and its production started in 50's, the initial researches showed that the physical-chemical proprieties of these thin films make them promising to be applied in electrical, optical and mechanical areas. Some of these proprieties which are worth mentioning are the high coefficient of piezoelectric coupling, the high acoustic speeds, the high bandwidth value and the high thermal conductivity. (INTERRANTE *et al.*, 1989)

Aluminum nitride (AlN), zinc oxide (ZnO) and lithium niobate (LiNbO<sub>3</sub>) have been mostly used as piezoelectric material because they have a central asymmetric hexagonal (Wurtzite) crystal lattice. This characteristic guarantees piezoelectric coefficients different of zero, i.e., the hexagonal structure is the principal characteristic, which defines the properties of a piezoelectric material. (EIRAS, 2004) (CHEN *et al.*, 2018)

Many film growth techniques are used to obtain AlN, such as plasma-assisted molecular beam epitaxy (PAMBE) (IWATA *et al.*, 2007), pulsed laser deposition (PLD) (SURESH; MUTH, 2008), chemical vapour deposition (CVD) (SATO *et al.*, 2007), ion beam deposition (IBD), ion implantation (MATSUMOTO; KIUCHI, 2006) and the last but not the least, the reactive magnetron sputtering (RMS). The latter one is interesting to the microelectronic market because it is able to produce thin films at low temperature, acquiring an excellent morphological quality and preferential crystallographic orientation. (PELEGRINI *et al.*, 2014) (ADACHI *et al.*, 2012)

## 1.2 Motivation for the Study

Silicon has been studied for a long time, but currently, its proprieties implemented with nitrides proprieties have been one of the mains reasons for the microelectronic advances. The semiconductor nitrides have benefits that make this kind of material interesting to the market. The advantages in this material are that the electrons travel four times more quickly, support higher temperature than silicon and they have high hardness. Consequently, many technologies could be developed, such as transistors with better performance, solar cells, LEDs and sensors. (CHEN *et al.*, 2018)

The SAW sensors have been found commercially for more than 60 years and today there are several unexplored parameters. The aluminum nitride (AlN) is mainly used in surface acoustic wave (SAW) sensors because this material allows a high propagation velocity of the acoustic wave. However, any change in its structural parameters during the thin film grown can modify the wave speed propagation on its surface. For that reason, the AlN deposition process becomes a very promising research target. Even a minimal modification in the deposited film changes the material's piezoelectricity, interfering in the sensitivity of the surface acoustic wave sensor.

So, the study of MEMS is increasing exponentially in the last years. According to the last ten year, the number of publications per year about SAW development is on the rise. On the other hand, the researches about aluminum nitride for SAW sensor application did not follow the same way, as shown in Figure 1.2.

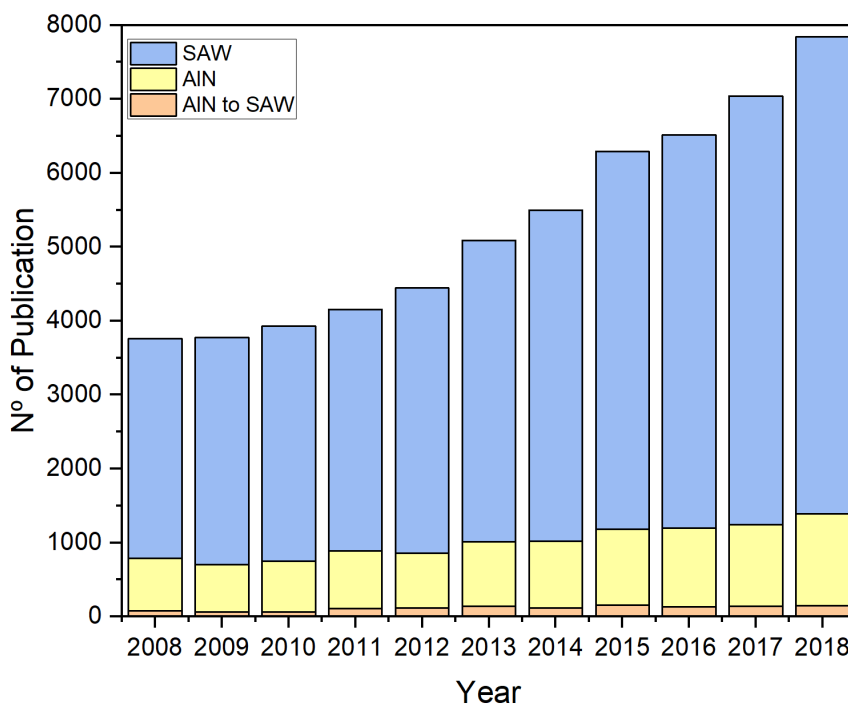


FIGURE 1.2 – Numbers of science publication with the topics "aluminum nitride", "surface acoustic waves sensor" and "AlN for SAW sensor application". (SCIENCEDIRECT, 2018)

## 1.3 Objectives

The main objective of this work is to find the radio-frequency (RF) reactive sputtering process deposition conditions to deposit high-quality crystalline aluminum nitride thin films for application as surface acoustic wave sensors.

### 1.3.1 Specific Objectives

- Deposition of AlN thin films varying the RF power, nitrogen concentration and residual pressure.
- To investigate the AlN thin films morphology.
- To study the film crystalline structure.
- To analyze the optical and electrical properties of the AlN thin films.

## 1.4 Outline

The present work is divided in six chapters, where the first one is about the introductory part of the work.

The second chapter describes the literature review, presenting a review about papers and works that involves aluminum nitride deposited by magnetron sputtering. Furthermore, this chapter presents state of the art about deposition procedures of aluminum nitride thin film to be applied in SAW devices.

The third chapter presents a basic theoretical foundation of nitrides, semiconductor nitrides, in especially the aluminum nitride, the piezoelectric effects and its importance in SAW applications.

The fourth chapter describes the experimental procedures used to the AlN thin film deposition process and the techniques used to characterize it.

The results and a discussion about the deposited thin films are presented in the fifth chapter.

The sixth chapter relates the main conclusions of this work obtained through the results and discussions. It also presents some suggestions for possible future works that can complement the research developed in this work.

# Chapter 2

## Literature Review

In this chapter is presented a state of art and literature review about aluminum nitride, showing its main deposition techniques, thin film characteristics and analyses for application in SAW.

The aluminum nitride thin film researches are increasing in the micro-electro-mechanical system (MEMS) field, especially in SAW devices application. (XU *et al.*, 2001) The deposition of AlN on a silicon substrate is a promising piezoelectric material to be applied in SAW devices because of its mechanical properties, high thermal conductivity and wide bandgap. (ALRASHDAN *et al.*, 2014) Also, the AlN with hexagonal wurtzite structure presents high electrical resistivity, high resistance to breakdown voltage, high acoustic propagation rate and low-temperature signal loss. (XU *et al.*, 2001)

The AlN has a large band gap (6.2 eV) in III-IV group of semiconductors. (KUMARI *et al.*, 2014) The AlN with a hexagonal wurtzite crystalline structure has high acoustic velocity, which turns it an attractive candidate of piezoelectric materials for high-frequency surface acoustic waves device applications, such as resonators, high-frequency filters and pressure sensors. (KHAN *et al.*, 2015)

The deposition process requires some care to ensure the best quality of the thin film deposited. The AlN thin film with desired properties demands a high purity source and oxygen-free environment due to the high aluminum reactivity with oxygen. (KUMARI *et al.*, 2014) However, all the physical properties of AlN film are significantly influenced by its crystallographic orientation. (KHAN *et al.*, 2015) In other words, to guarantee high-quality crystalline with preferred orientation, homogeneous composition, low surface roughness AlN films, is essential to have high control of the deposition parameters during the process. (XU *et al.*, 2001)

Well-oriented AlN thin films can be grown on silicon substrate at relatively low temperature (below 300 °C). (ALRASHDAN *et al.*, 2014) So, the most adequate method to

grow AlN thin film with such quality and deposition condition are the physical vapour deposition (PVD) method, such as radio frequency magnetron sputtering. (DUQUENNE *et al.*, 2007)

PELEGRINI analyzed the effect of pressure in the study of piezoelectric materials of family III-V obtained by reactive sputtering aiming its application in sensors and MEMS. The parameters used during the deposition process were residual pressure of  $5.33 \times 10^{-5}$  Pa ( $4 \times 10^{-7}$  Torr) with RF power set in  $1.23 \text{ W/cm}^2$ , the gas content with 1:2 (Ar :  $\text{N}_2$ ) and varying the process pressure of 0.27 to 0.67 Pa (2 to 5 mTorr). The results show that the lower pressure (0.27 Pa - 2 mTorr) increases the deposition rate six times due to the higher molecule average free path into plasma. So, the authors concluded that higher deposition rates with lower pressure are due to the AlN molecules trend to arrive perpendicularly on the substrate surface favoring the columnar growth of AlN crystals with high piezoelectric constant. The authors also describe that lower process pressure than the used in the study presented ( $< 0.27$  Pa - 2 mTorr) the plasma is not stable.

ALRASHDAN *et al.* used DC sputtering to deposit AlN thin films on silicon. The deposition was performed using 200 W with distance target-substrate of 100 mm for times of 30 and 60 minutes with 75 %  $\text{N}_2$ . (ALRASHDAN *et al.*, 2014) In this case, the deposited films were amorphous as shown the XRD diffractograms of Figure 2.1-(a). The authors considered that it occurs because of high nitrogen content, which decreases the momentum at the silicon substrate due to the difference of mass between nitrogen and argon atoms, consequently decreasing the AlN deposition rate. The same experiment was performed using 50 % of  $\text{N}_2$  and the deposited films showed a wurtzite crystal structure with crystallographic orientation (002), Figure 2.1-(b). It demonstrates the influence of nitrogen concentration and how it interferes in the deposition rate of AlN at silicon wafer. (ALRASHDAN *et al.*, 2014)

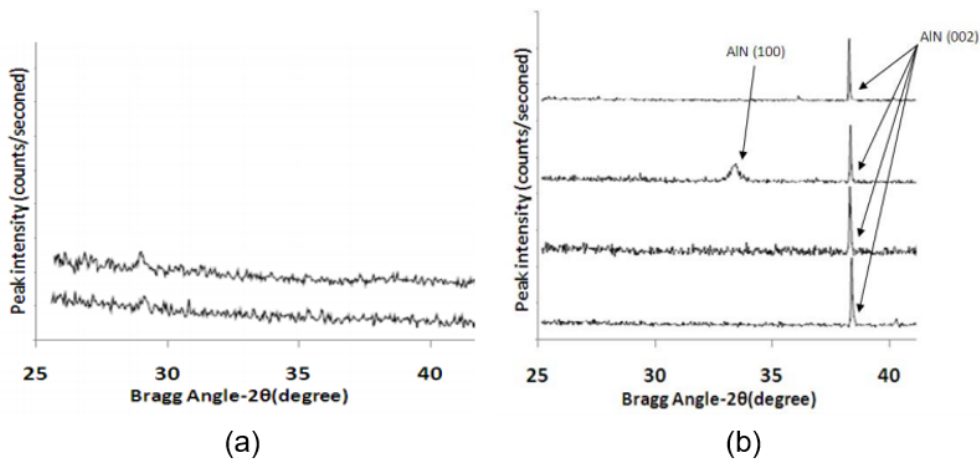


FIGURE 2.1 – XRD diffractograms of AlN films deposited at 200 W DC and gas flow rate  $\text{N}_2$  : Ar (a) 30:10 sccm and (b) 20:20 sccm. (ALRASHDAN *et al.*, 2014)

DUQUENNE *et al.* evaluated the influence of nitrogen concentration in AlN thin films deposited by magnetron sputtering using a gas mixture in the range of 10 to 60 % [ $R = N_2/(Ar + N_2)$ ]. (DUQUENNE *et al.*, 2007) The AlN thin films were deposited using a sample holder kept 50 mm distant of the aluminum target with rf power fixed in 100 W for 60 minutes and the working pressure varied from 1.0 to 2.5 Pa (7.5 to 18.75 mTorr). The deposition rate decreases as function of the increase of nitrogen content. The authors report that this effect is due to the strong nitriding of the target (the target poisoning). The XRD diagrams of AlN deposited with different nitrogen concentrations, Figure 2.2-(a), show that peaks with orientation (101) and (100) are related with low and high nitrogen concentration in the gas mixture, respectively. However, all spectra present a common peak in  $36^\circ$  assigned to the plane (002). Figure 2.2-(b) shows that the full width at half maximum (FWHM) obtained by the  $E_2$  Raman mode and IR mode of vibration  $E_1(T_o)$  analysis increases with the nitrogen concentration. The authors judge it as a degradation of the crystalline quality of deposited films. (DUQUENNE *et al.*, 2007)

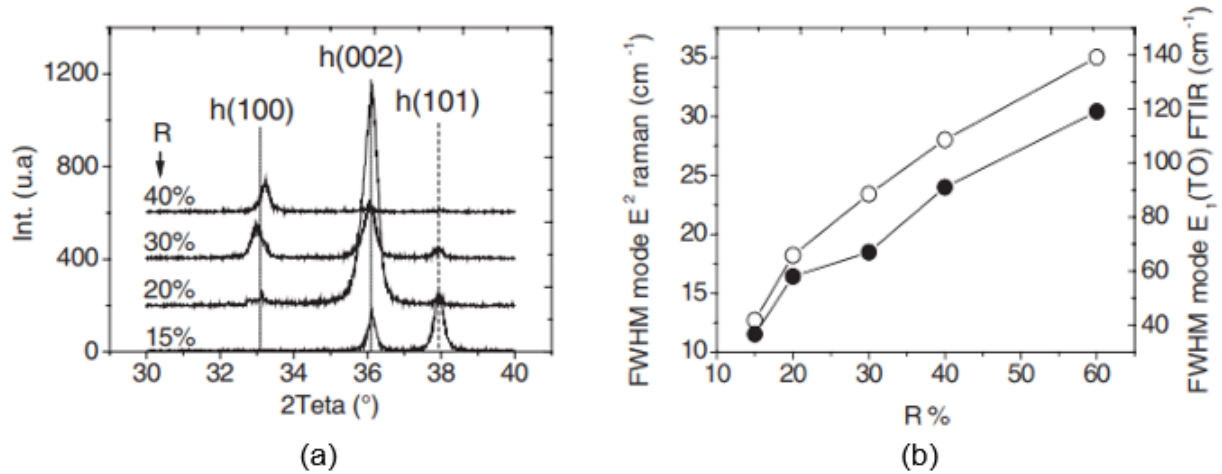


FIGURE 2.2 – (a) Effect of the nitrogen contents on the AlN thin film structure. (b) Evolution of the FWHM Raman mode  $E_2$  (open circles) and the IR mode of vibration  $E_1(TO)$  of aluminum nitride (bold circle) versus  $R = N_2/(Ar + N_2)$ . (DUQUENNE *et al.*, 2007)

In the article of (KHAN *et al.*, 2015), textured nano-crystalline AlN thin films were grown on silicon (111) substrate using DC magnetron sputtering with a residual pressure of about  $10^{-4}$  Pa ( $7.5 \times 10^{-7}$  Torr). The distance target-substrate was kept at 30 mm. Prior to the deposition process of 40 minutes, was performed a pre-sputtering for 10 minutes with the shutter closed. The deposition pressure was fixed in  $6.0 \times 10^{-1}$  Pa (4.5 mTorr) and the DC power maintained in 160 W. Samples were deposited at different nitrogen content and the XRD spectra are shown in Figure 2.3.

Samples deposited at the same temperature process ( $500^\circ\text{C}$ ) with low nitrogen concentration (30 %  $N_2$ ) presented peaks in the planes (102) and (103). And the film deposited

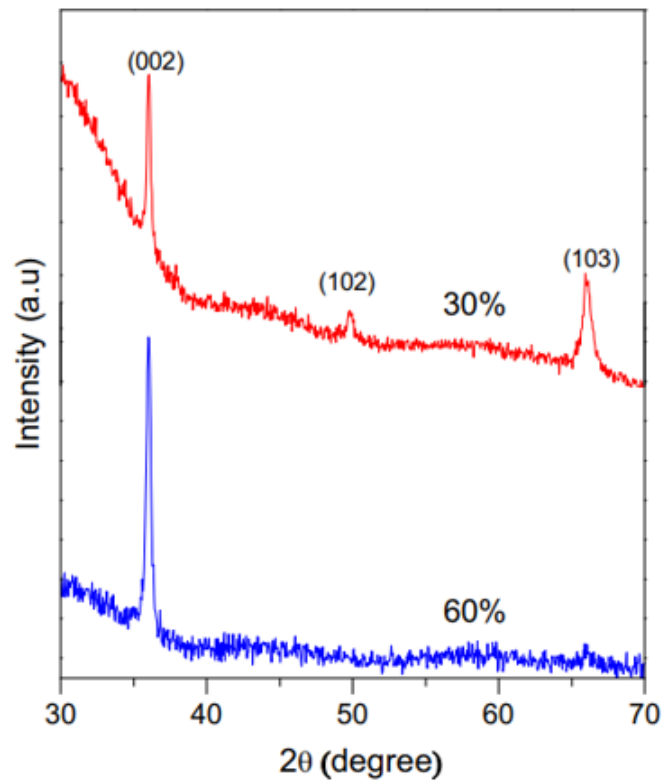


FIGURE 2.3 – XRD spectra of AlN films prepared at various nitrogen condition. (KHAN *et al.*, 2015)

with 60 % of nitrogen shows a single peak of (002) orientation plane. The FWHM decreases with the decrease of nitrogen concentration (60 %  $N_2$  -  $0.295^\circ$  and 30 %  $N_2$  -  $0.246^\circ$ ). However, the crystallite size increases in lower nitrogen content (60 %  $N_2$  - 284 and 30 %  $N_2$  - 341 Å). The low nitrogen concentration infers in low energy to the depositing species and the significant impacts of the heavier argon ion impart energy to depositing species enabling them to grow in other orientations as (102) and (103).

Furthermore, through spectroscopic ellipsometry (Figure 2.4) the samples were analyzed the refractive index with two samples varying the deposition temperature (500 °C and 400 °C). The refractive index ( $n$ ) acquired in these samples varied in a range of 1.84-1.9 at 2.3 eV, which is values reported by MAHMOOD *et al.* and VENKATARAJ *et al.*. (KHAN *et al.*, 2015)

The studies of morphological properties of AlN piezoelectric thin films deposited by DC reactive magnetron sputtering developed by (XU *et al.*, 2001) were realized in a system with  $5.0 \times 10^{-5}$  Pa ( $3.75 \times 10^{-7}$  Torr) of residual pressure. The aluminum target was cleaned by a pre-sputtering of 15 minutes and the time of deposition process was varied from 40 and 60 minutes. The nitrogen content was fixed in 50 %, the DC power used was 50 W and the target-substrate distance was 40 mm.

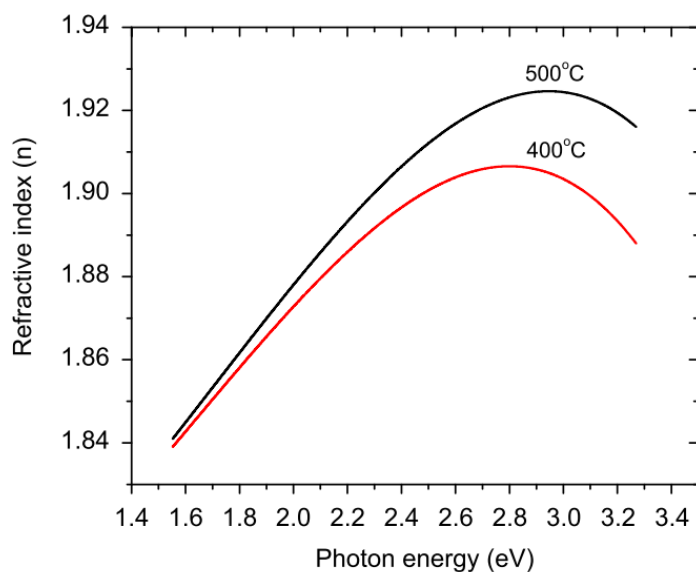


FIGURE 2.4 – Influence of substrate temperature on the refractive index. (KHAN *et al.*, 2015)

Figure 2.5-(a) presents the XRD diffractograms for samples deposited with pressures varying from 0.3 to 1.2 Pa (2.25 to 9 mTorr). Sample deposited at low pressure, 0.3 Pa (2.25 mTorr), only the (002) diffraction peak at  $36^\circ$  appeared. For pressures of 0.4 Pa (3 mTorr) and 0.5 Pa (3.75 mTorr) the AlN films present peak in the planes (002), (100) and (101) indicating no preferential orientation. For higher sputtering pressure, only appeared a preferential orientation of AlN (100) peak at  $33.2^\circ$ , but the peaks intensity decreases and broadens with the increase of the pressure. The authors describe that the amorphization effect occurs because of the decrease of energy of the sputtered species due to the decrease of the mean free path.

The author also shows the AlN thin films structure as function of deposition power (from 30 W to 100 W) for a fixed pressure of 0.3 Pa (2.25 mTorr), Figure 2.5-(b). The films deposited at 30 W presented a nonpreferential orientation with peaks of AlN in the (100), (101) and (002) planes. Films deposited with 40 to 65 W presented preferential orientation on the (002) plane. For higher power, 80 W, the AlN structure present again a nonpreferred orientation with the presence of peaks in the planes (100), (002), (101) and (110). Authors concluded that this may occur because of an increase in the nucleation rate along with the increase in sputtering rate. In 100 W power deposition, the Al phase is present in XRD patterns because of the high sputtering rate of aluminum and consequently the presence of metallic aluminum in the deposited film. But the authors also conclude that the impact of  $N_2$  concentration on the preferential orientation, which is necessary to identify the best power to the nitrogen content for the desired film proprieties. (XU *et al.*, 2001)

In addition, XU *et al.* showed that the target-substrate distance is also an important

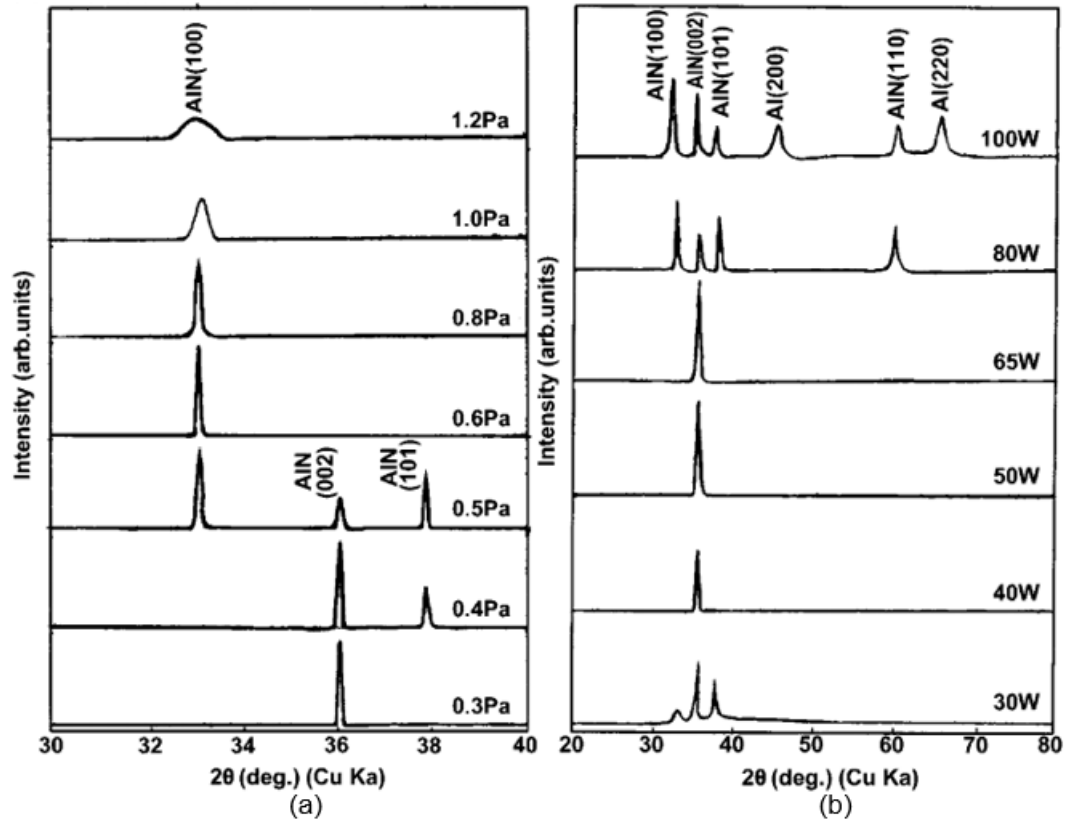


FIGURE 2.5 – The XRD patterns of AlN (a) at different sputtering pressures ( $N_2$  50%, power 50 W, distance D 40 mm); (b) at different target powers ( $N_2$  50%, sputtering pressure 0.3 Pa (2.25 mTorr), distance D 40 mm). (XU *et al.*, 2001)

parameter to define the sputtering pressure and its settings depend upon the desired orientation structures of the AlN thin films. So, to grow AlN oriented in (002) plane the curve that defines it is curved I in Figure 2.6. The authors choose pressure of deposition process of about 0.3 Pa (2.25 mTorr) consequently, the target-substrate distance was 50 mm.

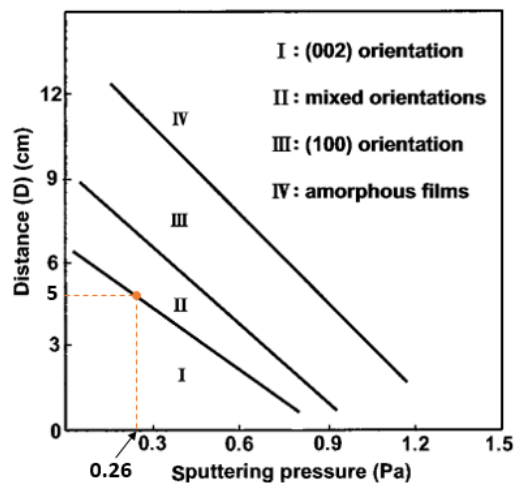


FIGURE 2.6 – Orientation diagram of AlN films under various sputtering pressures and distances D. (XU *et al.*, 2001)

The study of the properties of AlN thin films deposited by reactive magnetron sputtering demonstrates the influence of the DC power applied during the process. The deposition was realized with residual pressure of about 1.0 mPa ( $7.5 \times 10^{-6}$  Torr), the pre-sputtering was made with Ar at 100 W for 20 minutes. The deposition process was performed using 60 % of  $N_2$ , pressure of 2.0 Pa (15 mTorr), target-substrate distance of 65 mm and process time of 60 minutes. The DC power was varied from 100 to 400 W. The films thickness increases with the increase of the applied DC power on the cathode as presented in Figure 2.7-(a). The XRD diffractograms, Figure 2.7-(b), obtained by grazing incidence identify the same peak at  $33.310^\circ$  in all samples corresponding to AlN (100). The intensity of the peak increases with the increase of the applied DC power. (KUMARI *et al.*, 2014)

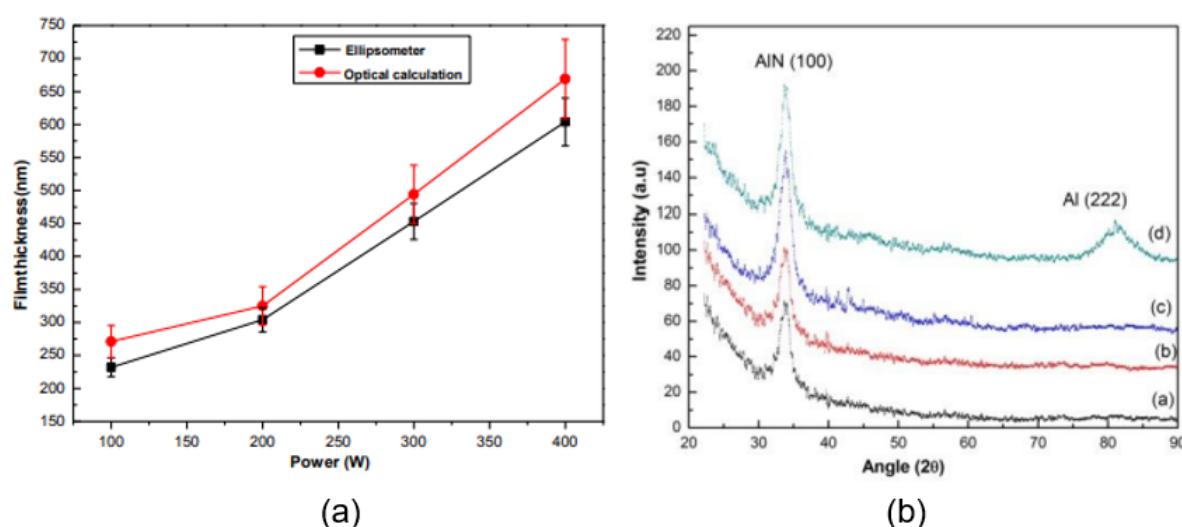


FIGURE 2.7 – (a) Film thickness of AlN films versus applied DC power; (b) GIXRD diffractograms of the deposited film prepared at different DC power; (a) 100W, (b) 200W, (c) 300W and (d) 400W. (KUMARI *et al.*, 2014)

AISSA *et al.* performed the characterization of AlN films deposited by DC magnetron sputtering (DCMS) and high-power impulse magnetron sputtering (HiPIMS) for SAW applications. (AISSA *et al.*, 2015) The experiment was developed with target distance from substrate holder of 30 mm, cathode power of 150 W and the residual pressure of the system was 6.0 mPa ( $4.5 \times 10^{-5}$  Torr). The pre-sputtering was made using argon gas for 15 minutes. The AlN deposition was made in commercial templates of 200 nm thick AlN epitaxially grown on (111) Si substrate. The deposition process was performed by 12 minutes using 35%  $N_2$  and pressure of 0.4 Pa (3 mTorr).

Figure 2.8-(a) shows the XRD spectra with the presence of AlN (002) peak indicating the preferential orientation on the c-axis that is interesting to SAW application because of the high-velocity acoustic propagation of this piezoelectric material. The sample A (Epitaxial AlN/Si (111)) and the sample B (AlN deposited by DCMS on Epitaxial AlN/Si (111)) have the preferential orientation (002) and they have the same type of tensile

stress, even when the film thickness of sample B is twice thicker than sample A. On the other hand, sample C (AlN deposited by HiPIMS on Epitaxial AlN/Si (111)) presents a broadened (002) peak explained by the authors due to the tensile residual stress from the epitaxial AlN buffer layer and the compressive residual stress from the AlN layer deposited by HiPIMS. Furthermore, the Figure 2.8-(b) presents the Raman spectra of the three samples, where the sample B and C presents a little shift to high energy that the authors explain by the residual stress of the films. (AISSA *et al.*, 2015)

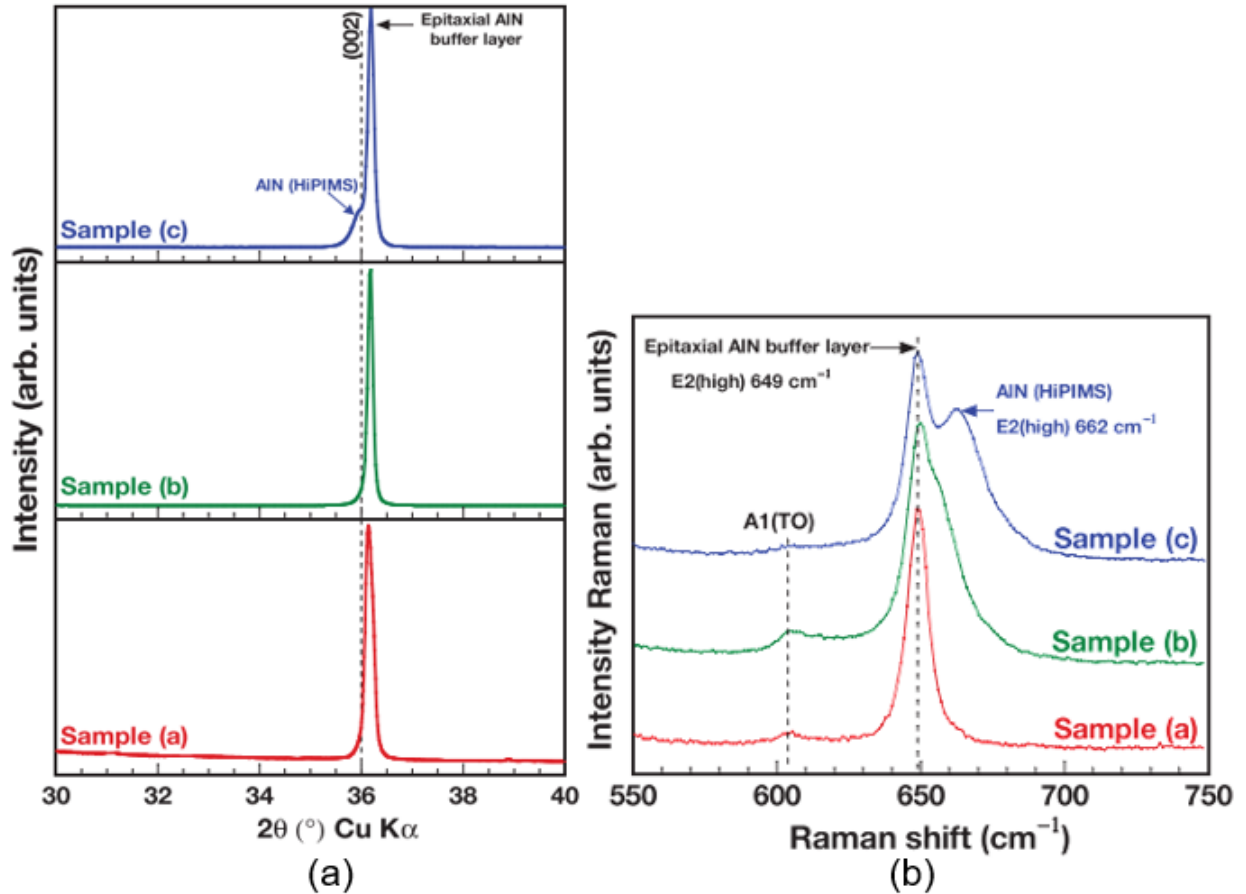


FIGURE 2.8 – (a) XRD patterns of the AlN thin films; (b) Room temperature Raman spectra of AlN thin films. (AISSA *et al.*, 2015)

According to LUGHI; CLARKE, in the search of defect and stress characterization of AlN by Raman spectroscopy, defended that the Raman spectroscopy did not qualify just the deposited films through measuring the crystallographic texture, but this technique can also investigate properties that can interfere the MEMS device performance, such as the acoustic losses. Other important AlN properties that affect MEMS resonator performance cited by the author are the residual stress, by observing the frequency shift of the  $E_2^{high}$  phonon Raman line, and the defect density, by monitoring the width of the peak. Also, the author correlated these effects with the oxygen content present in the material.

To experimental analyses, the authors deposited AlN thin film in Si (100) by ac re-

active sputtering of a pure aluminum target and in the gas mixture of Ar : N<sub>2</sub> - 40:20 sccm. The residual pressure before deposition process was  $< 1.33 \times 10^{-5}$  Pa ( $10^{-7}$  Torr), the sputtering process was maintained in 1.5 Pa (11.25 mTorr) and the substrate was preheated until 500°C. The thickness films obtained varied between 1000-2300 nm and the grain diameter also varied in 50-200 nm, it can be observed in Figure 2.9. In addition, the authors analyzed the thin films with XRD and Raman techniques. In the XRD, diffractometry the peak present in the spectra shows that the films were crystalline and had a preferential orientation with the wurtzite. Investigating the FWHM (full width of half maximum) of this evident peak (002) was between 1.2° and 2.4°. The Raman presents a peak at about 520 cm<sup>-1</sup> originated from the silicon substrate and the peak at  $\sim 658$  cm<sup>-1</sup> corresponds to the  $E_2^{high}$  mode of AlN. The FWHM of this peak was measured on the spectra and varied between 10.0 and 17.7 cm<sup>-1</sup>. Through this technique and the secondary ion mass spectroscopy (SIMS) was possible to analyze the amount of oxygen and the defect concentration, measuring the residual film stress and the defect density, and correlating with the acoustic losses in the UHF regime. For MEMS applications is very important to minimize the stress and acoustic losses of the material.

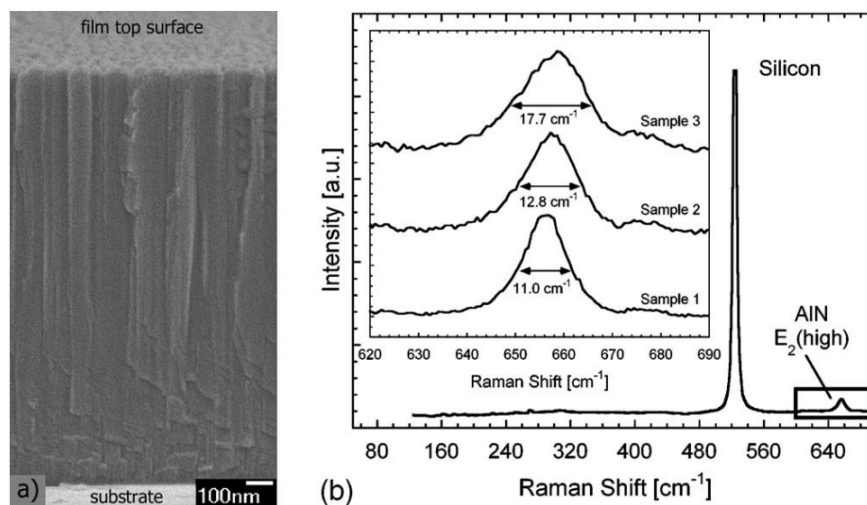


FIGURE 2.9 – (a) Scanning electron microscopy image of the cross-section of a typical AlN film used in this study; (b) Raman spectrum of a typical c-axis textured AlN film on silicon (100). The inset shows an enlarged view of the spectral region where the  $E_2^{high}$  optical phonon of AlN is visible for three selected samples. The FWHM is also indicated. (LUGHI; CLARKE, 2006)

ZHANG; CHEN deposited AlN film by RF magnetron sputtering on silicon (100) substrate for application in integrated acoustic resonators. The deposition parameters used were: residual pressure lower than 4.0 mPa ( $3 \times 10^{-5}$  Torr), pre-sputtering with Ar for 15 minutes, substrate temperature of 300 °C, RF power varied from 50 to 200 W, work pressure of 0.53 Pa (4 mTorr) and a gas mixture containing 60% N<sub>2</sub>. (ZHANG; CHEN, 2013)

Figure 2.10-(a) presents the XRD diffractograms of the films deposited at 0.5 Pa (3.75 mTorr) and different RF power. The film deposited at low RF power (50W) shows a wide band near  $34^\circ$  that corresponds to an amorphous phase. In film deposited at 100 W power, two orientation peaks are evidenced by AlN (002) and (100) corresponding the angles  $33^\circ$  and  $36^\circ$ , respectively. However, samples grown with high RF power (150 and 200 W) the preferential orientation (002) of wurtzite is evidenced. But authors declare that further increase of RF power fails to improve the (002) texture of the deposited film. They believe that need to find another correspondent parameter to obtain the optimum conditions to obtain hexagonal wurtzite crystalline films.

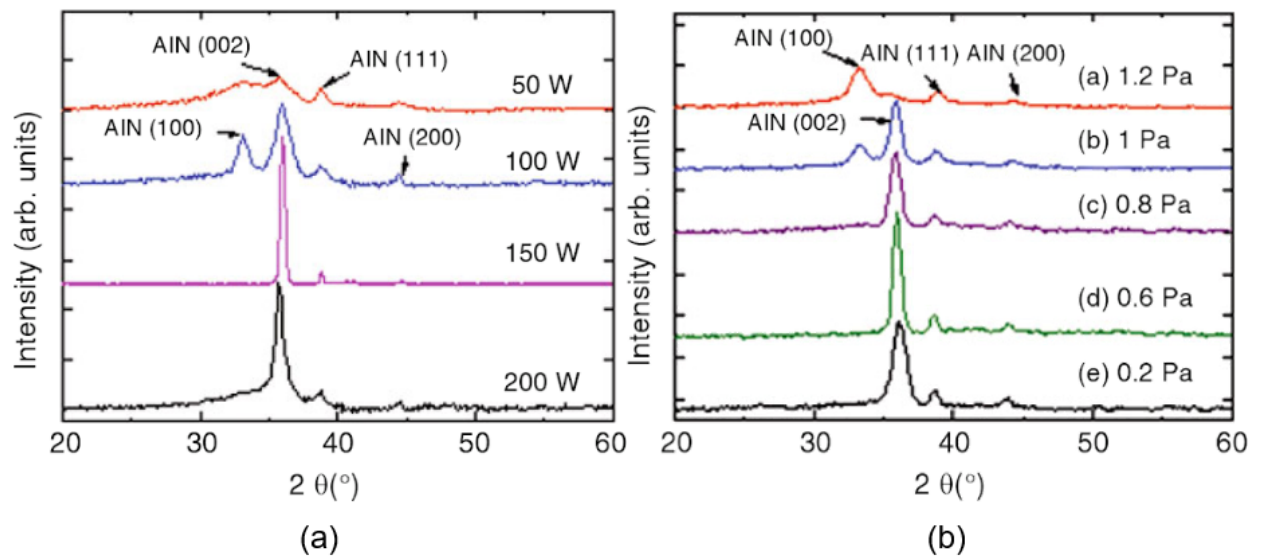


FIGURE 2.10 – (a) XRD diffractograms of AlN films deposited (a) at 0.5 Pa (3.75 mTorr) and different RF power; (b) at 150 W for different deposition pressure. (ZHANG; CHEN, 2013)

In the same experiment was investigated the effect of the deposition pressure in the range of 0.2 to 0.8 Pa (1.5 to 6 mTorr) while keeping the RF power at 150 W and 50% of  $N_2$ . Figure 2.10-(b) presents the XRD diffractograms where can be observed that for pressures  $< 1.0$  Pa (7.5 mTorr) the deposited films show one preferential orientation of AlN (002).

They also investigated the nitrogen concentration in the gas mixture for pressure of 0.5 Pa (3.75 mTorr) and 150 W of RF power. The XRD diffractograms presented in Figure 2.11-(a) show that only the films deposited with 70% and 100%  $N_2$  presented the oriented peaks of AlN (002). For the other samples with low argon content (80%  $N_2$  and 90%  $N_2$ ) in the gas mixture, the deposited film was amorphous and (200) and (100) oriented AlN films.

The chemical composition for the AlN film deposited at RF power (150W), work pressure of 0.5 Pa (3.75 mTorr) and 60%  $N_2$  obtained by EDX is shown in Figure 2.11-

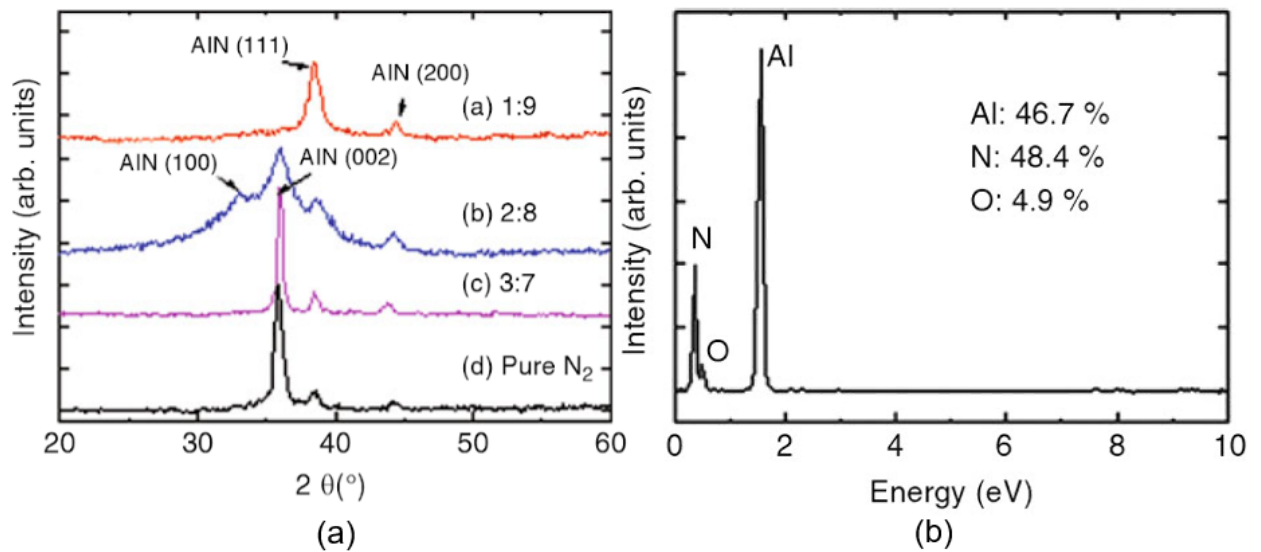


FIGURE 2.11 – (a) The XRD results of the AlN films deposited at different  $N_2:r$  ratio; (b) The EDX spectra of the AlN film deposited at the optimized process. (ZHANG; CHEN, 2013)

(b) and contain Al (46.7 %), N (48.4 %) and O (4.9 %), which indicates the presence of oxides on the film. (ZHANG; CHEN, 2013) The film morphology of this sample is shown in the micrographs of Figure 2.12. The film surface, Figure 2.12-(a), shows the presence of crystalline grains, which has haricot shape with nearly uniform size. Figure 2.12-(b) presents the film cross-section where can be observed the columnar crystal shape with c axis vertical to the substrate.

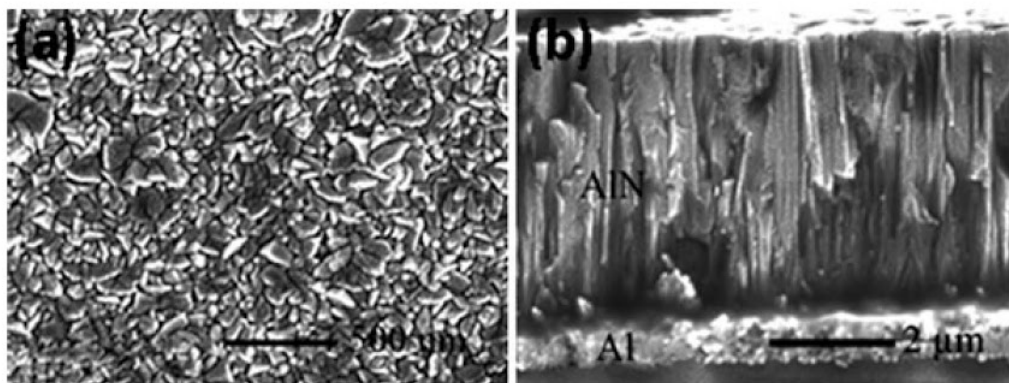


FIGURE 2.12 – The morphology of the AlN film deposited at the optimized process, (a) the surface, (b) the cross-view. (ZHANG; CHEN, 2013)

JOO *et al.* investigated the optical and structural properties of AlN thin films characterized by spectroscopic ellipsometry. The AlN thin film was deposited on  $SiO_2/Si$  or Si substrates by RF magnetron sputtering. The target-substrate distance was kept at 70 mm and the Al target with a purity of 99.999%. All films except SW series were deposited at  $Ar : N_2 = 0.8 : 0.3$  Pa (6 : 2 mTorr), and the SW series was utilized at  $Ar : N_2 = 0.5$

: 0.3 (4 : 2 mTorr). The best-fit model parameters of AlN thin films are summarized in Table 2.1 and the spectra in Figure 2.13.

TABLE 2.1 – Best-fit model parameters of AlN thin films. (JOO *et al.*, 2000)

Label	RF Power (W)	Time (min)	$A$	$B$	$\lambda_0$ (nm)	$n_f$	$n_s$	$\sigma$
S <sub>1</sub>	150	120	1.08	2.99	138.2	2.05	1.39	0.028
S <sub>2</sub>	150	250	1.00	3.12	138.6	2.07	1.42	0.050
S <sub>O1</sub>	120	240	0.97	2.98	139.2	2.03	1.27	0.106
S <sub>O2</sub>	180	240	1.08	3.19	144.7	2.11	1.35	0.259
S <sub>O3</sub>	210	240	1.22	3.22	147.1	2.15	1.50	0.318
S <sub>Wa</sub>	180	180	1.10	2.96	142.2	2.05	1.36	0.112
S <sub>Wb</sub>			0.98	3.10	139.6	2.06	1.35	0.105
S <sub>Wc</sub>			1.05	3.02	140.6	2.05	1.29	0.100
S <sub>Wd</sub>			1.00	3.05	139.6	2.05	1.29	0.080

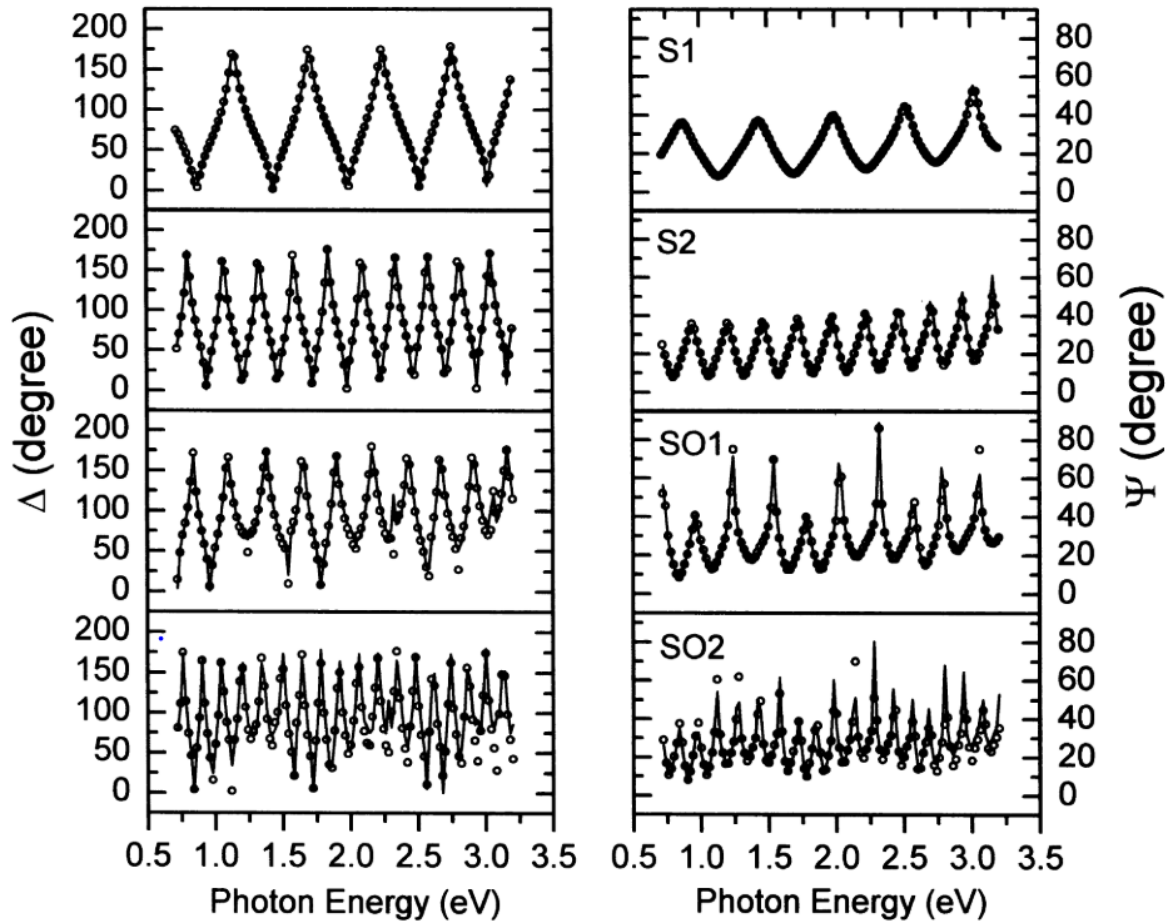


FIGURE 2.13 – Spectroscopic ellipsometry angles measured (open circle) and calculated from the best-fit model (solid curves). (JOO *et al.*, 2000)

The thicker films present high oscillation in the  $\Delta$  and  $\psi$  spectra due to the interference and present higher fitting errors, as illustrated in Figure 2.13. The films exhibited normal dispersion and the refractive index at a long wavelength (Figure 2.14). The curves were acquired with ellipsometry data between 0.7 and 3.2 eV range.

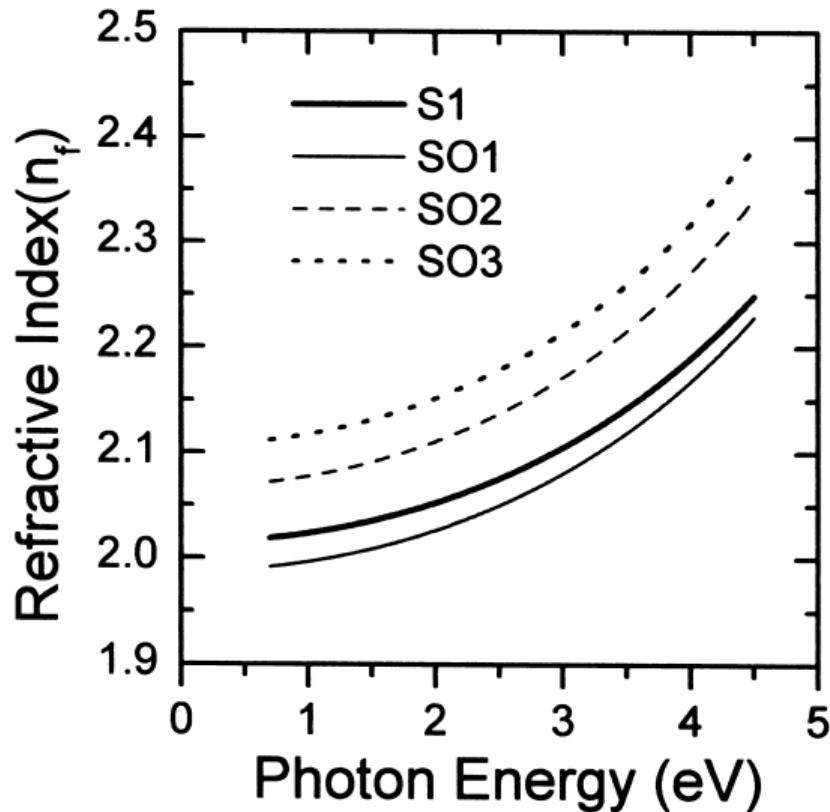


FIGURE 2.14 – Typical refractive index curves for the AlN thin films obtained from the best-fit parameters in Table 2.1. (JOO *et al.*, 2000)

The authors affirmed that the optical parameters, refraction index ( $n$ ) and extinction coefficient ( $k$ ) are determined by the chemical composition and structural disorder (e.g. oxygen, impurities, void and lattice defect). So, the correlation between XRD and SE techniques needs to be an increase discussion, but JOO *et al.* discussed this apparent correlation with the results of a film with high refractive index and low extinction coefficient had the best crystalline alignment, which is suitable to SAW devices applications. Also, in analyses from scanning electronic microscopy (SEM) the films deposited in high pressure (Ar : N<sub>2</sub> = 1 : 0.3 Pa ~ 8 : 2 mTorr) exhibited low refraction index, poor crystallinity and high thickness to thickness ratio, in consequence these films presented a columnar structure with less closely packed boundaries (Figure 2.15-(b)) which are susceptible to oxidation, as compared with a good textured film (Figure 2.15-(a)).

BRITO studied the fabrication and characterization of SAW sensors based in AlN thin film. In this study was explored the deposition rate as function of the applied RF power, pressure and distance target-sample. Figure 2.16 presents an X-Ray diffractogram of AlN

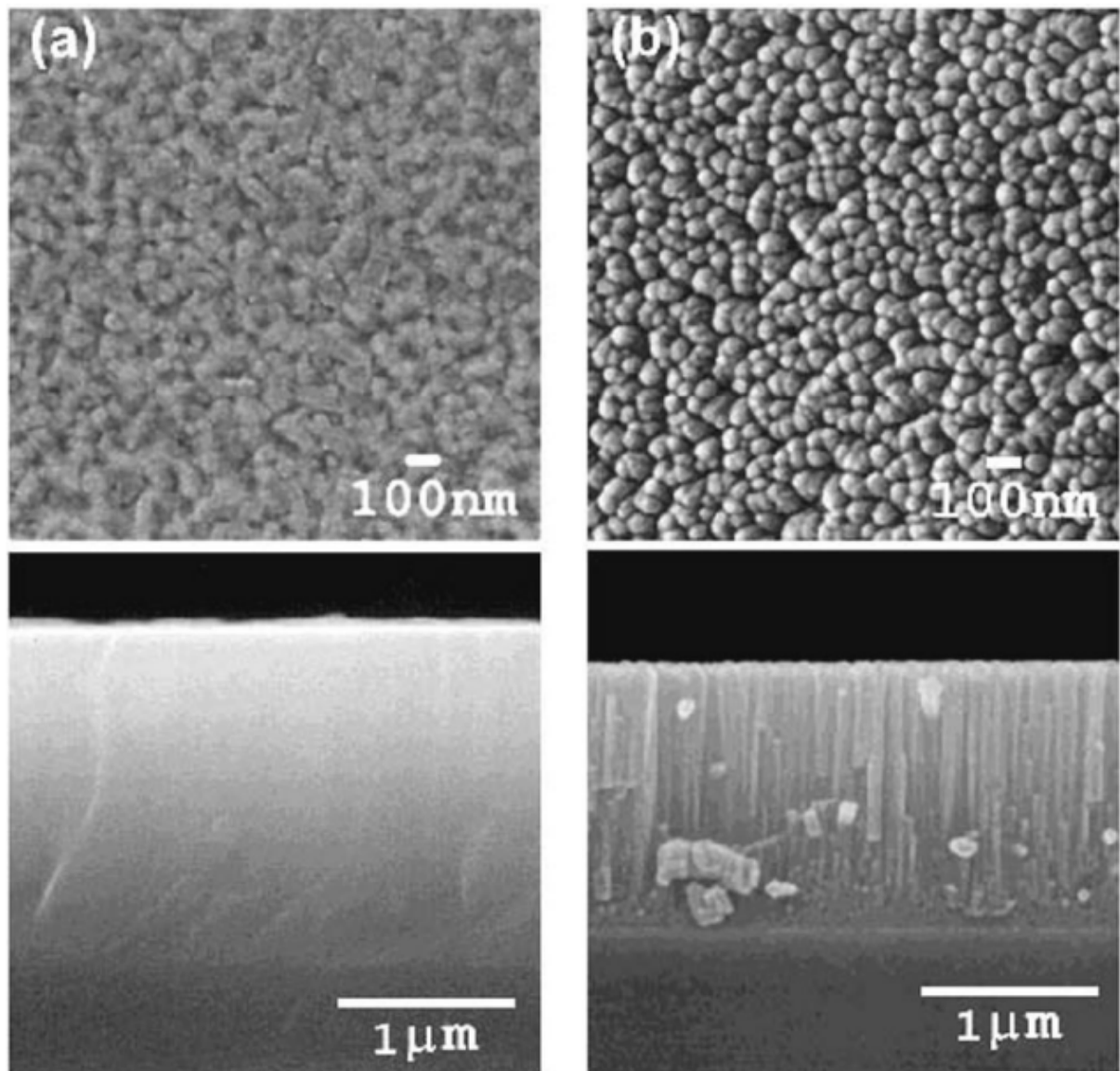


FIGURE 2.15 – SEM micrographs of AlN films deposited on SiO<sub>2</sub>/Si at different Ar/N<sub>2</sub> partial pressures: (a) 0.8:0.3 Pa (6:2 mTorr) and (b) 1:0.3 Pa (8:2 mTorr). (JOO *et al.*, 2000)

thin films deposited at 100, 200 and 300 W using a pressure of 0.27 Pa (2 mTorr) and target-sample distance of 50 mm. Only the AlN thin film deposited using 300 W presented a hexagonal structure oriented at the plane h-(002). The author explains the formation of amorphous AlN thin films for the others condition due to the lack of enough energy of the particles impinging the sample surface to promote the atomic rearrangement or by the presence of impurities (mainly oxygen) in the gas phase. In addition, the author concludes that the AlN-(002) orientation was obtained in almost all conditions applied, except when elevated target-sample distance (70 mm and 100 mm) or high applied pressure, that the films growth in the planes (100) and (002). (BRITO, 2014)

MEDEIROS studies the growth of SiC, SiC and AlN thin films by dual magnetron sput-

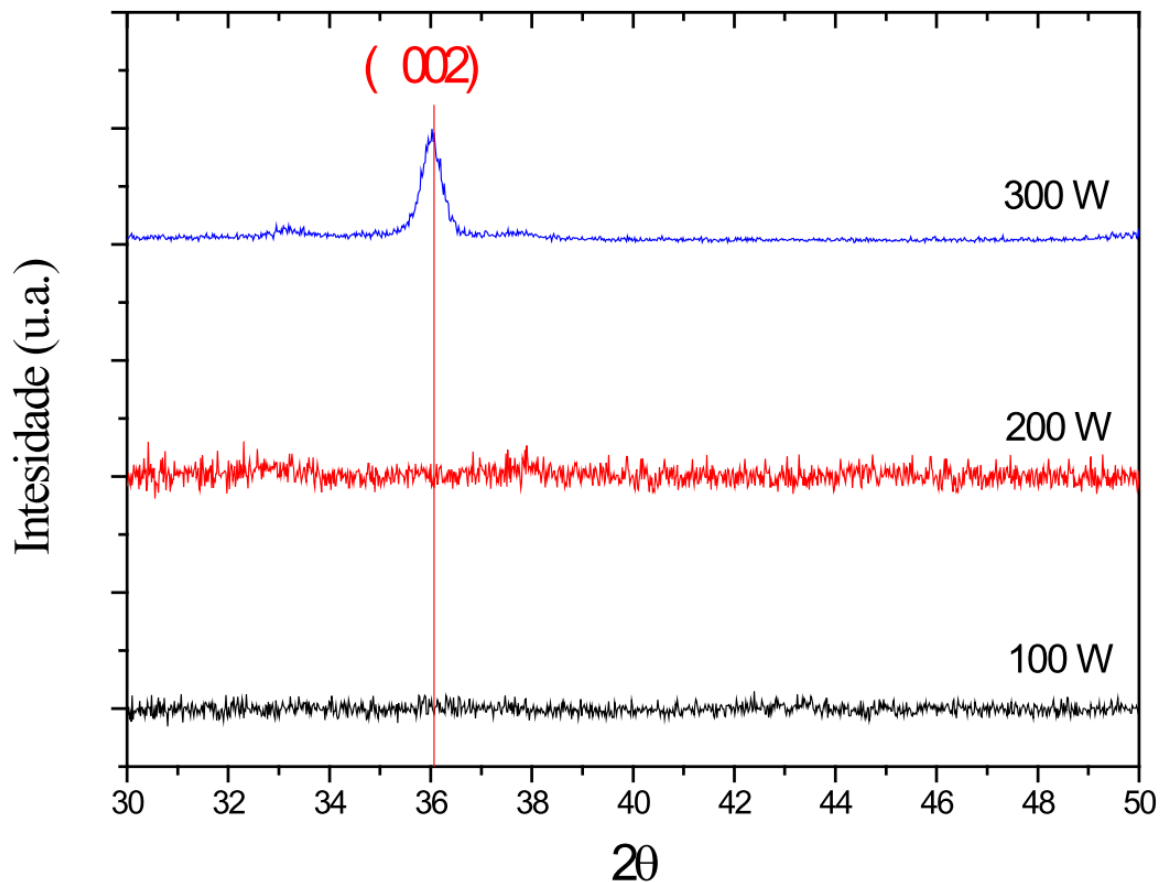


FIGURE 2.16 – XRD Diffractograms of AlN films in function of applied power, fixing the values  $P=0.27$  Pa (2mTorr) and  $d=50$ mm. (BRITO, 2014)

tering varying the target-sample distance and gas flow aiming application in microsensors. The study showed that the target-sample distance affects directly the deposition rate and the crystallinity of the films:  $d_{a-s} > 120$  mm presented amorphous films and  $d_{a-s}=80$  mm highly crystalline. With lower target-sample distance, the film presented low oxygen concentration. The XRD results showed that the nitrogen content (80%  $N_2$ ) favors the formation of cubic (100) oriented AlN films. (MEDEIROS, 2012)

OLIVEIRA deposited AlN thin film at different argon and nitrogen flow rate (0 to 280 sccm and 0 to 100 sccm, respectively), substrate temperature (80 to 600°C) and deposition time (1 to 10 hours). The results obtained showed that the AlN refractive index is relatively insensitive to the variation  $N_2$  from 10 to 100%. For high nitrogen content, the complete nitriding occurs on the target, poisoning it and reducing the deposition rate changing the sputtering process characteristics, but the films presented highly-oriented structures. The films were analyzed by ellipsometry technique and, it presented refraction indices between 2.0 to 2.2 showing that these films presented low impurities. Films deposited in low reactive gas concentrations presented multi-oriented metallic structure and/or amorphous AlN films. (OLIVEIRA, 2004) The films were analyzed by Raman spec-

troscopy and presented typical AlN  $E_2^1$  modes in region of  $228 - 252 \text{ cm}^{-1}$  and  $E_2^2$  modes in region of  $631 - 655 \text{ cm}^{-1}$  (Figure 2.17). (OLIVEIRA *et al.*, 2001)

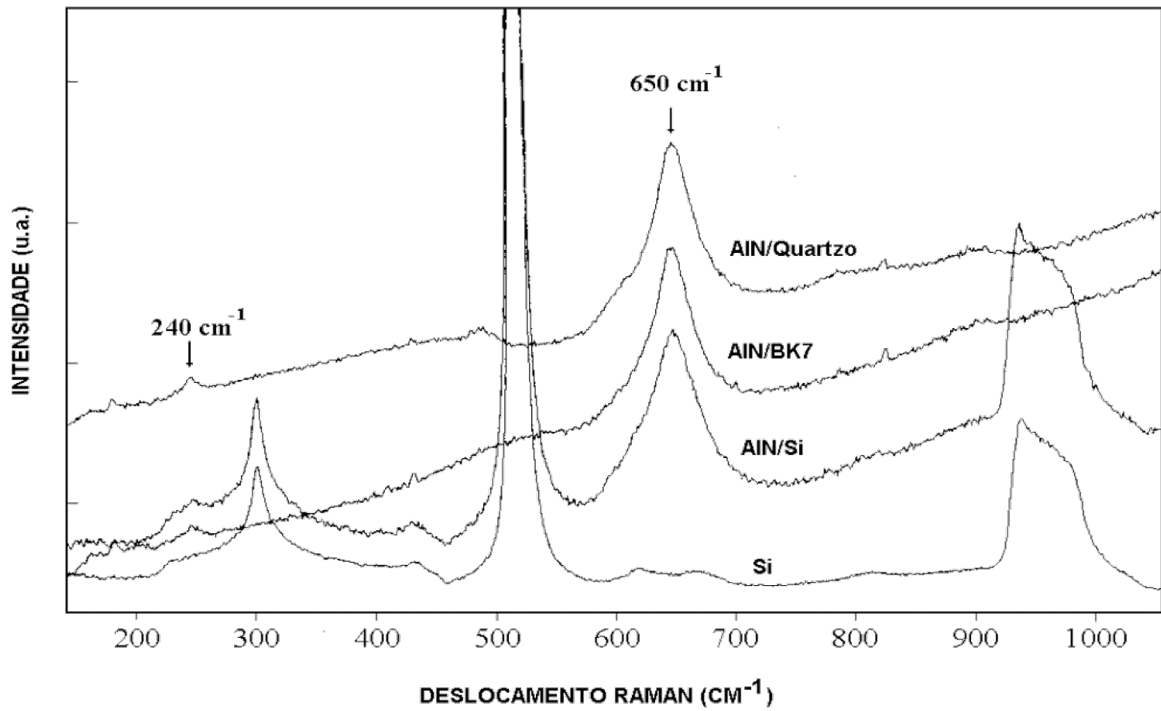


FIGURE 2.17 – Room-temperature Raman spectra of the AlN films grown on different substrate materials. All spectra were taken under the same geometry. (OLIVEIRA *et al.*, 2001)

# Chapter 3

## Theoretical Foundations

This chapter contemplates a basic theoretical foundation of nitrides, semiconductors and piezoelectric effects.

### 3.1 Nitride

The nitrides are chemical compounds formed by nitrogen and it has a wide range of properties and application, such as:

- Heat-resistance - Refractory;
- Insulating - BN,  $\text{Si}_3\text{N}_4$ ;
- Semiconductors - GaN, AlN;
- Solid lubricants - BN;
- Manufacture cut tools -  $\text{Si}_3\text{N}_4$ ;
- Surface coatings - TiN,  $\text{Fe}_2\text{N}$  and
- Fuel cell -  $\text{Li}_3\text{N}$ . (PIERSON, 1996)

Nitride is defined by compounds formed by nitrogen and elements of lower or about equal electronegativity. The nitrides can be classified in five general categories that depend on the binding element and their electronic structure and binding type. The nitride categories are illustrated in the periodic table shown in Figure 3.1. (COTTON; WILKINSON, 1972)

The interstitial nitrides are formed by the accommodation of nitrogen in the metal interstice, the difference of electronegativity and atomic size between the atoms being large.

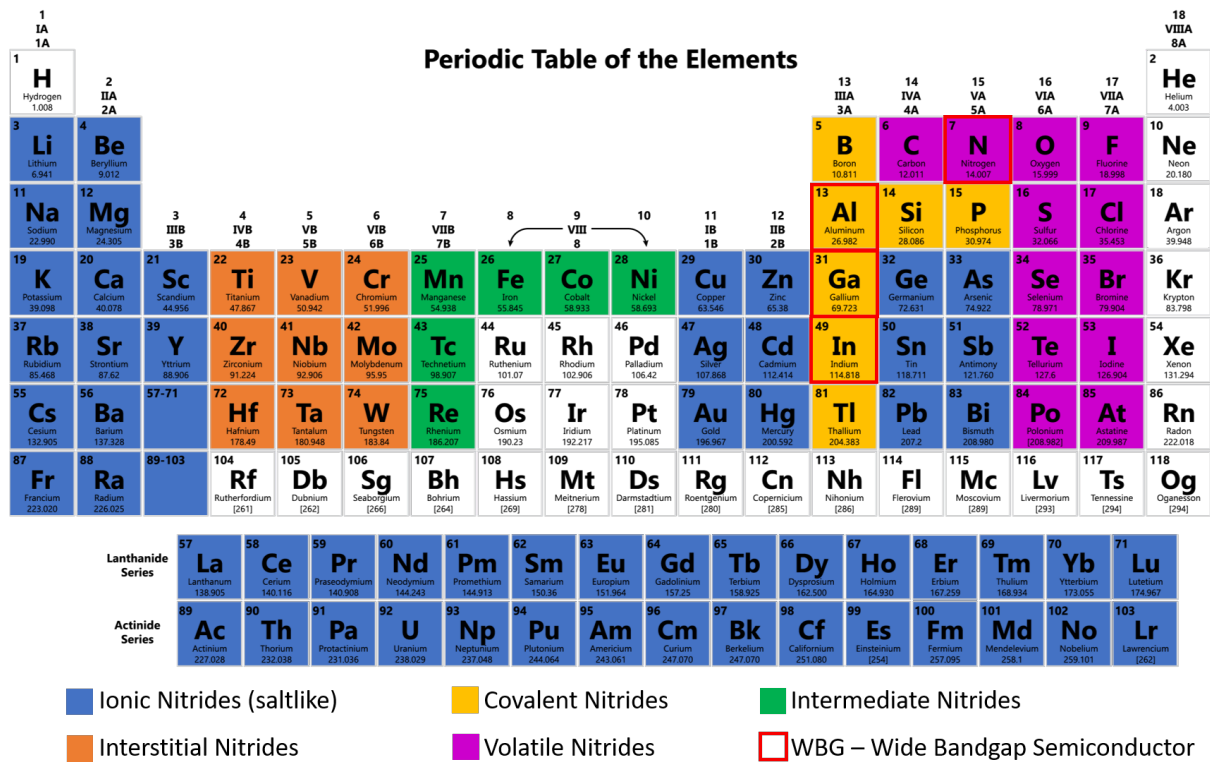


FIGURE 3.1 – Periodic classification of the elements and the formation of nitrides and semiconductors of wide gap. Adapted from (PIERSON, 1996)

However, the covalent category occurs when this difference is small and the electronic bonding being essentially covalent. This category consists of the non-metallic elements of Group IIIA (B, Al, Ga, In and Tl), besides Si and P, showed in the periodic table of Figure 3.1. The Groups VIIB and VIIIB form the category of intermediate nitrides, where the transition metals (Co, Mn, Fe and Ni) are chemically unstable, which the chemical bond breaks down quickly. (PIERSON, 1996)

The salt-like nitrides are composed of nitrogen and most electropositive elements, such as the alkali metals and the Group III of the periodic table of Figure 3.1. The difference of electronegativity between these compounds is large, but the atomic bonding is essential ionic.

The semiconductors nitrides have wide bandgap semiconductor (WBG), present high ionicity, very short chemical bonds, low compressibility, good thermal stability and are inert to chemical and radiation attacks. For that reason, they present a large interest in the industry besides not presenting risks to the environment. The WBG material allows the fabrication of devices with the capability to operate at higher temperatures and high-power switching applications. (YODER, 1996)

### 3.1.1 Semiconductors Nitrides

Semiconductors of Group III-V, such as AlN, GaN, InN and their ternary and quaternary alloys emit and absorb the wavelength in the visible spectral and short wavelength as violet and ultraviolet spectra. This Group also has benefits as high spectral selectivity that allows fine cut-off frequency control by only regulating the molar composition of their ternary alloys and are ease to manufacturing heterojunction devices. (MONROY *et al.*, 2003)

These characteristics promote the development of optoelectronic and electronic devices for high potentials and temperatures. Examples of semiconductor applications are laser diodes, photodiodes and photoconductivity sensors. Besides emitting and absorb light applications, these semiconductors groups possess piezoelectric proprieties that allows the manufacturing of electroacoustic devices to applications in high frequencies as radiofrequency filters, sensors and MEMS (Microelectromechanical Systems) devices. (AKASAKI; AMANO, 1997)

### 3.1.2 Aluminum Nitride

The aluminum nitride, AlN, is a material with many excellent mechanical, thermal, optical and electronic proprieties that present an enormous potential to be applied in various technological applications. An example of it is the high surface propagation wave speed, the excellent piezoelectric proprieties, the excellent coefficient of electromechanical coupling, high hardness, high melting point and associated with the chemical stability to high temperatures (above to 2000 °C). These exceptional combinations make the AlN an attractive candidate to be applied in temperature and pressure sensors based on surface acoustic waves, for instance. (CLEMENT *et al.*, 2004) (ELMAZRIA *et al.*, 2006)

AlN can be used as a ceramic substrate to elaborate micro-circuits, mainly in the aerospace area because it has excellent thermal proprieties such as thermal dissipation. The AlN also is applied in the light transmitting windows and in emitter devices in UV region because of its high bandwidth value ( $\sim 6.2$  eV). (STRITE, 1992)

The aluminum nitride (AlN) is formed by the reaction of nitrogen and aluminum elements. The AlN structure showed in Figure 3.2 is normally hexagonal close-packed (hcp) of the wurtzite (2H) type (hP4). The AlN with such structure present the higher piezoelectric coefficient ( $5 \times 10^{-2} C^{-1}$ ) among the nitrides of the IIIA group making it appropriate to applications such in microelectronics. The AlN has isomorphous crystallographic structure and high resistivity ( $\sim 1013 \Omega.cm$ ). (FIREK *et al.*, 2015)

Figure 3.2 shows the AlN atomic bonding where the aluminum atom is bonded to four nitrogen atoms in a fourfold coordinated tetrahedral ( $sp^3$ ) arrangement. The aluminum

has lower electronegativity than nitrogen. However, the nitrogen element has the smallest atomic radius. The aluminum nitride is excellent electrical insulators because of its electrons are strongly bonded to the nucleus and are not available for metallic bonding. (PIERSON, 1996)

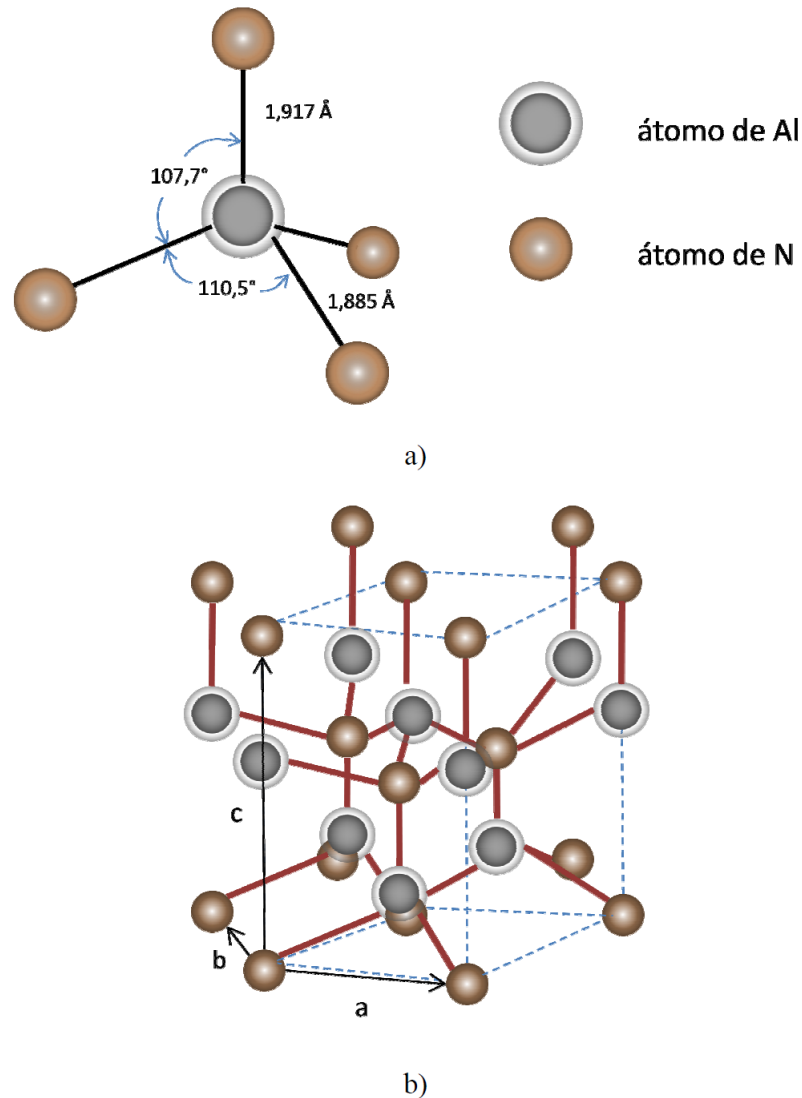


FIGURE 3.2 – Schematic representation of the crystal structure of aluminum nitride. a) Tetrahedron formed by one atom of Al and four of N; b) Unit cell forming the Wurtzite structure of AlN. (RODRÍGUEZ-CLEMENTE *et al.*, 1993)

Aluminum nitride can be found in three forms: Wurtzite represented in Figure 3.3 is the most common form because it can be found in room temperature. Both other forms are the metastable phases: the Zincblende form is more frequently obtained when growth on Si (001) and GaAs (100) bulk, and a cubic form, known as Rocksalt, that have been found only in experiments with high pressure. The preferential growth orientation of the Wurtzite is on the axis  $c$  as shown in Figure 3.4. (RODRÍGUEZ-CLEMENTE *et al.*, 1993)

The ionicity of the atomic bond is a powerful parameter to the obtain information

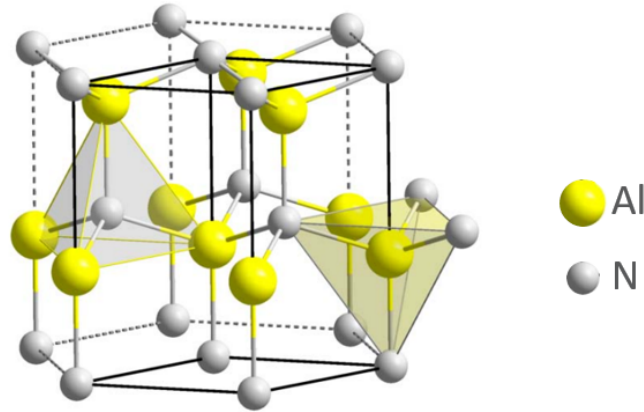
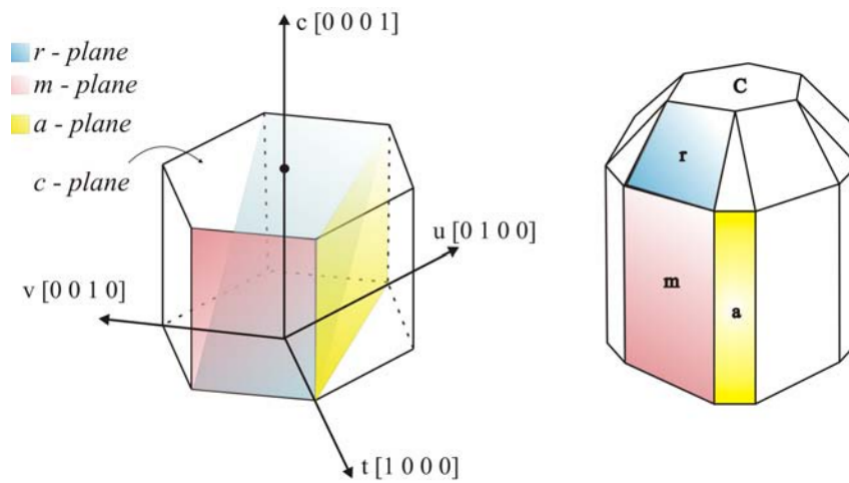
FIGURE 3.3 – Hexagonal wurtzite structure of aluminum nitride. (FU *et al.*, 2017)

FIGURE 3.4 – Planes for the hexagonal wurtzite structure. (MOURA, 2010)

about the crystalline structure of the AlN. The ionicity can be defined according to the relation of Equation 3.1, which is a fraction of ionic ( $f_i^\alpha$ ) compared with covalent ( $f_h^\alpha$ ). The ionicity of the main semiconductors' nitride is cited in Table 3.1. (ADACHI, 2005)

$$f_i^\alpha + f_h^\alpha = 1 \quad (3.1)$$

TABLE 3.1 – Ionicity Phillips ( $f_i$ ), Pauling ( $f_i^P$ ) e Harrison ( $f_i^H$ ) for the semiconductor nitrides. (ADACHI, 2005)

Material	$f_i$	$f_i^P$	$f_i^H$
BN	0,221	0,42	0,43
AlN	0,49	0,56	0,57
GaN	0,500	0,55	0,61
InN	0,578	-	-

The Phillips ionicity is based on the connection between the chemical bonding properties of the  $A^N B^{8-N}$  family of crystals and their electronic energy-band structure. Analyzing the covalent and ionic energy, Phillips found a correlation between chemical bond ionicity and crystalline structure adopted by the compound that for reduced values of  $f_i$ , consequently has high  $f_c$  and then present tetrahedral structure coordinate zinc-blend (zb). Wurtzite structure is obtained when the values of  $f_i$  are high. According to Phillips the observed chemical bond present in semiconductors and the stabilization of material structure between zinc-blend and wurtzite is a result of the balance between ionicity and chemical covalent bond. (PHILLIPS, 1970)

The material symmetry group is defined by the distance between atoms in the crystal lattice and the arrangement in the structure and it explains the physical and chemical proprieties of a material. To define the symmetry of a hexagonal structure is necessary to set the AlN lattice parameters,  $a = 0.3112$  nm and  $c = 0.4982$  nm. The lattice constant and symmetry are exposed in Table 3.2.

TABLE 3.2 – Crystal structure, space group, lattice constants  $a$  and  $c$  ( $T = 300\text{K}$ ) for semiconductor nitrides; d = diamond, zb = blende, h = hexagonal, w = wurtzitic and rs = cubic. (ADACHI, 2005)

Material	Structure	Symmetry	$a$ (Å)	$c$ (Å)
c-BN	zb	$F\bar{4}3m(T_d)$	3,6155	-
h-BN	h	$P6_3/mmc(D_{6h})$	2,5040	6,6612
w-AlN	w	$P6_3mc(C_{6v})$	3,112	4,982
c-AlN	zb	$F\bar{4}3m(T_d)$	4,38	-
$\alpha - GaN$	w	$P6_3mc(C_{6v})$	3,1896	5,1855
$\beta - GaN$	zb	$F\bar{4}3m(T_d)$	4,52	-
InN	w	$P6_3mc(C_{6v})$	3,5848	5,760

Another parameter that depends on atoms arranged in the structure is the cleavage plane, this propriety is showed in Table 3.3.

TABLE 3.3 – Cleavage planes for various crystal structures of group III-V. (ADACHI, 2005)

Structure	Cleavage Plane
diamond	(111)
blende	(110)
wurtzite	$(11\bar{2}0), (11\bar{1}0)$
cubic	(100)

Though the AlN has significant mechanical proprieties above mentioned its hardness (Vickers Hardness) is 12 GPa, the young modulus of elasticity is 315 GPa and the flexural strength is between 590 – 970 MPa. Furthermore, the aluminum nitride is able to deform plastically to some degrees above the ductile-to-brittle. Besides these mechanical proprieties, the AlN has high temperature and corrosion resistance. (FITZ, 2002)

Thermal proprieties of monocrystals nitrides are based on the high melting point ( $>2000^\circ\text{C}$ ), but the aluminum nitride is a material difficult to reproduce the monocrystals growth. Thus, the AlN melting point can be obtained based on the lattice parameters using the Equation 3.2. The basic thermal proprieties, such as melting temperature, specific heat and Debye temperature of some semiconductor nitrides are shown in Table 3.4. (PELEGRINI, 2010)

$$T_m = 7159 - 957a, \quad (3.2)$$

$$\text{being } \begin{cases} a = \text{lattice parameter for blender and cubic structures} \\ a = a_{eff}, a_{eff} = (\sqrt{3}a^2c)^{\frac{1}{3}} \text{ to hexagonal} \end{cases}$$

The AlN has thermal stability up to  $2200^\circ\text{C}$ , thermal conductivity of about 320 W/mK and has good metallization capacity. (FIREK *et al.*, 2015) Just for comparison, the thermal conductivity of  $\text{SiO}_2$  is 1,38 W/mK. This characteristic allows better heat dissipation in the device where it is applied, increasing the efficiency and consequently, the lifetime of the device. (PELEGRINI, 2010)

TABLE 3.4 – Melting point, specific heat and Debye temperature for semiconductor nitrides. (ADACHI, 2005)

Material	$T_m(K)$	$C_P(J/gK)$	$\theta_D(K)$
c-BN	$>3,246$	0.643	1,613
h-BN	-	0.805	323
w-AlN	3,487	0.28	988
$\alpha$ -GaN	2,791	0.42	821
InN	2,146	2.274	674

Due to these thermal properties' aluminum nitride is the most appropriate material to apply in electronic devices that requires high-power demand. The thermal conductivity of some nitrides is presented in Table 3.5.

TABLE 3.5 – Thermal conductivity for semiconductor nitrides and other materials of interest. (QUAY, 2007)

Material	K (W/cm K)
Si	148
GaAS	54
InP	68
c-BN	749
GaN	130
w - AlN	285
w - InN	38.5; 45; 80; 176
6H-SiC	390; 490
4H-SiC	330
Safira	42
Diamond	2000; 2500

The methodology to prepare samples needs attention because it can interfere in the material proprieties, such as optical and electrical proprieties, normally the impurities found are O, Al<sub>2</sub>O<sub>3</sub>, Al<sub>2</sub>OC. (STRITE, 1992) Impurities make electrical proprieties as resistivity varies in a very large range of 10<sup>11</sup> to 10<sup>13</sup> Ω.cm. The AlN also has one of the highest surface acoustic waves (SAW) speed (approximately 5500 m/s), making it a material attractive to Si integrated circuit application and in the fabrication of SAW devices. (PELEGRINI; PEREYRA, 2010)

The impurities effect in the material also produces a strong changing in the dielectric strength that varies from 1 to 6 MV/cm. (GEROVA *et al.*, 1981) (TSUBOUCHI; MIKOSHIBA, 1985) Normally, the typical value of the bandgap corresponding to the Al-N bonds is around 670 cm<sup>-1</sup> and can be decreased with post-processing annealing, due to the narrowing of the width of the vibrational band which contributes to an improvement in the crystallinity of the film. (INTERRANTE *et al.*, 1989)

The typical bandgap values (~ 6.2 eV) is also affected by the presence of the impurities in the deposited film. (PASTRÁK; ROSKOVCOVÁ, 1968) Figure 3.5 shows the bandgap energy values as function of the lattice constant for the nitrides with wurtzite structure as AlN, GaN and InN that have direct bandgap structure. When the aluminum or gallium nitrides are in the cubic form, they have indirect bandgap structure.

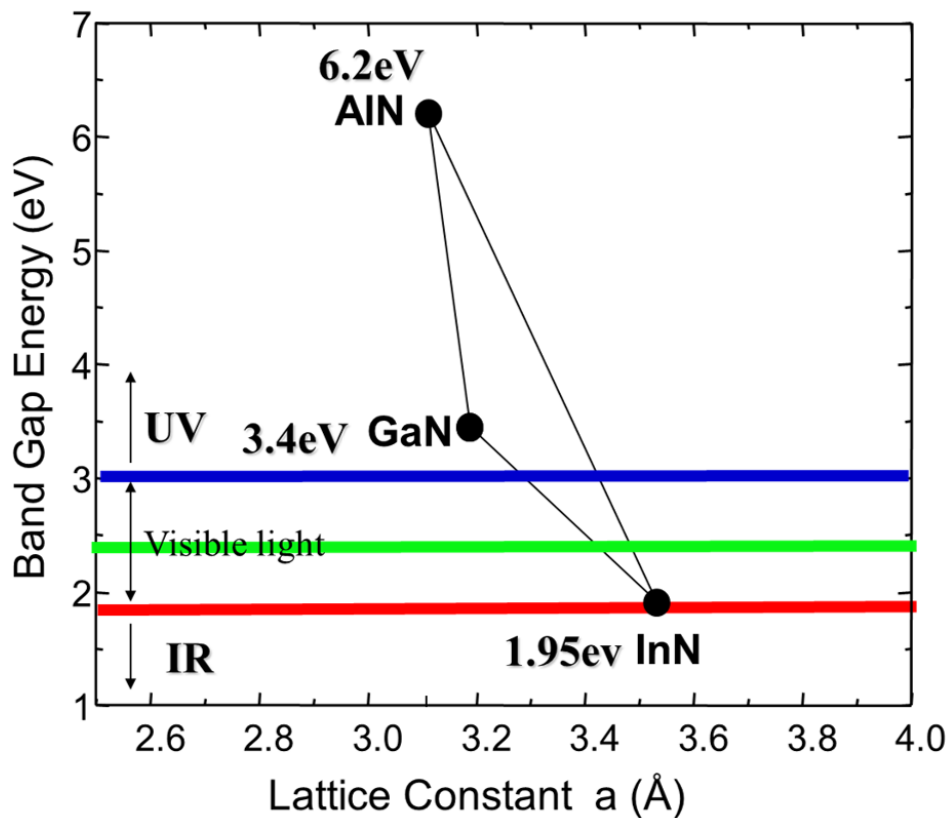


FIGURE 3.5 – Bandgap energy versus network parameters. (MOURA, 2010)

### 3.1.3 Piezoelectric Effect

Piezoelectric materials are characterized by their capability to transform electric stimulus in mechanical waves and mechanical stimulus in the electric signal. This occurs as consequence of the piezoelectric effect that was discovered in 1880 by the brothers Curie, Jaques and Pierre. It is presented in a natural form in many material classes such as semiconductors, ceramics and composites. Other materials can acquire this effect when they are submitted to high electric fields close to Curie temperature and in these cases, they are called ferroelectric materials. (HRIBŠEK *et al.*, 2010)

This effect can be classified in direct or converse effect. The direct effect consists of the electric field generation in a material through of a mechanical tension application that causes a deformation in its structure (Figure 3.6). But the converse effect is when mechanical deformation of material occurs from an external electric field application. (EIRAS, 2004) The piezoelectricity depends directly on the crystal structure of the material, so amorphous materials are not piezoelectric material. Then, the piezoelectric properties define the performance of the electroacoustic device. (NOYAN, 2013)

The piezoelectric effect occurs due to the lack center symmetry present in the material structure. When a mechanical deformation occurs, the charge within the material reorganizes, in consequence of it a dipole moment obtain value other than zero and thus the

## Piezoelectric Effect in Quartz

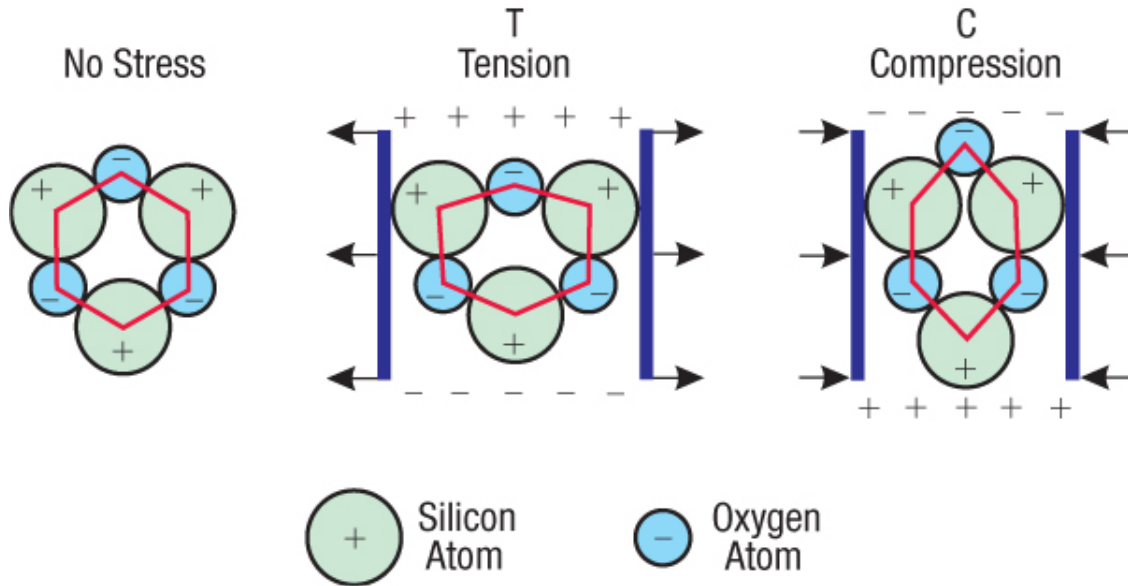


FIGURE 3.6 – Mechanism of piezoelectric effect in quartz. (GUPTA *et al.*, 2014)

electric field arises. However, when the material is exposed to an external electric field, the lattice atoms tend to reorganize to acquire a dipole inverse of this field implying in mechanical deformation. (WEIGEL *et al.*, 2002)

AlN has also piezoelectric coefficient  $d_{33}$  of  $5.1 \pm 0.1 \text{ pmV}^{-1}$ . (WRIGHT, 1998) The piezoelectric response of AlN with structure wurtzite comes from each dipole of all grains comprising the film. Hence, a film structure with high  $c$ -axis oriented yields a higher electromechanical coupling coefficient ( $k_t^2$ ), collaborating to the same sign to piezoelectric response as shown in Figure 3.7. In this context, is important to have  $c$ -axis oriented film with low oxygen content (below 1%) to guarantee a good piezoelectric response. Others factor that also interferes the piezoelectric response are the surface roughness, crystal morphology (grain size) and substrate type, which shows that the deposition parameters control is essential in order to reach these piezoelectric requirements. (IBORRA *et al.*, 2004) (PELEGRINI; PEREYRA, 2010)

Piezoelectricity is utilized in various application such as radio transmission, filter technology, nano-positioning, measurement of pressure, velocity and acceleration, gas sensor, biological sensor and others. (NOYAN, 2013) In 1965 the SAW sensor was developed and first used by White and Voltmer. Figure 3.8 shows the first sensors developed that are fabricated by the deposition of a piezoelectric material on a substrate with a metal structure deposited in bar forms on the top of the piezoelectric material. These metallic bars structures are called inter-digital transducers (IDT) and normally SAW sensor is composed of one or more IDTs set pairs. (WHITE; VOLTMER, 1965) The piezoelectricity of materials is essential for propagating surface waves between a transmitting and receiving transducer.

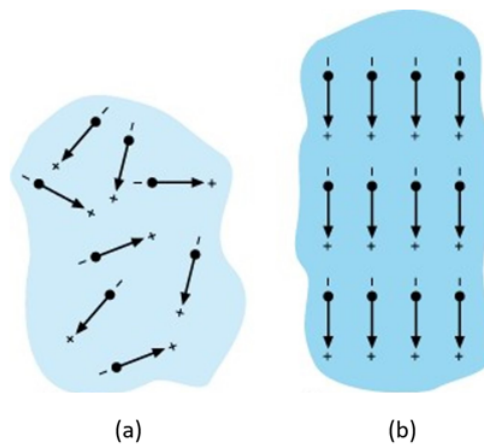


FIGURE 3.7 – Schematic of the dipole distribution along a piezoelectric net: (a) grains aligned in various directions and (b) grains aligned along the same direction. (LÓPEZ, 2016)

In other words, it consists mainly in the production of mechanical vibrations on a substrate through the application of an alternate electrical potential or vice versa. (BRAY *et al.*, 1987) Then, the transducers are resonators utilized to produce acoustic waves in piezoelectric substrates through the direct and converse piezoelectric effect, respectively. According to WHITE; VOLTMER, the IDT geometry, the chosen piezoelectric material and the electromechanical coupling plays fundamental role in the SAW sensor response and its operational sensibility. (COVACEVICE, 2012)

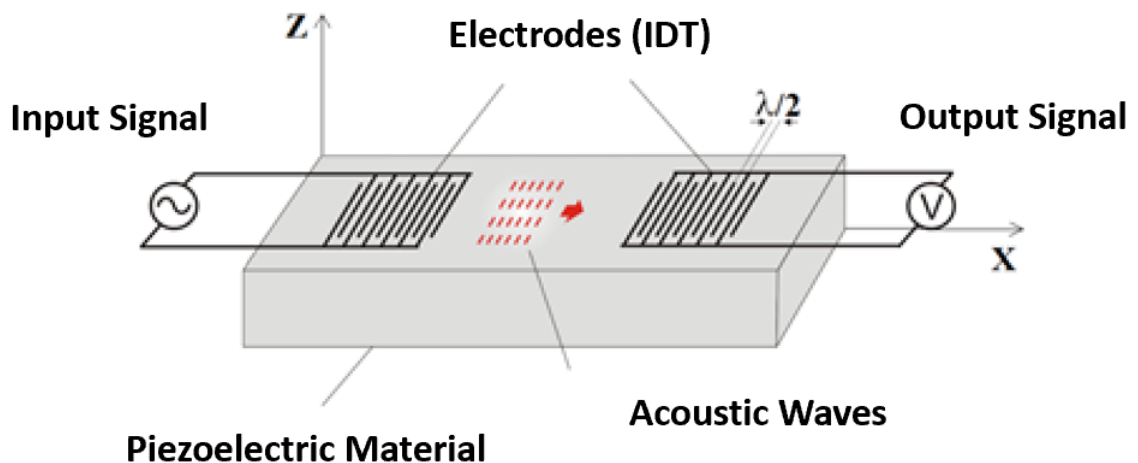


FIGURE 3.8 – Surface acoustic waves sensor. (WHITE; VOLTMER, 1965)

# Chapter 4

## Experimental Procedure

The present chapter describes the methodology used in this work and the characterization techniques to analyze the thin film properties.

This work consists in define a methodology to obtain the best parameters of thin film deposition of aluminum nitride by reactive magnetron sputtering aiming applications in SAW devices. The methodology of the work illustrated in the diagram of Figure 4.1 was divided into two sections: deposition parameters and thin films characterization.

The deposition parameters considered to be analyzed in this process were the applied RF power, the nitrogen concentration and the reactor residual pressure. The material characterization was carried out by mechanical and optical profilometry, X-ray diffraction, Raman spectroscopy, spectroscopic ellipsometry and field emission gun scanning electron microscopy.

### 4.1 Thin Films Deposition System

The aluminum nitride (AlN) thin films deposition were performed using an experimental apparatus composed by:

- Process chamber;
- Gas injection system;
- Vacuum system;
- Pressure monitoring;
- Power supply system.

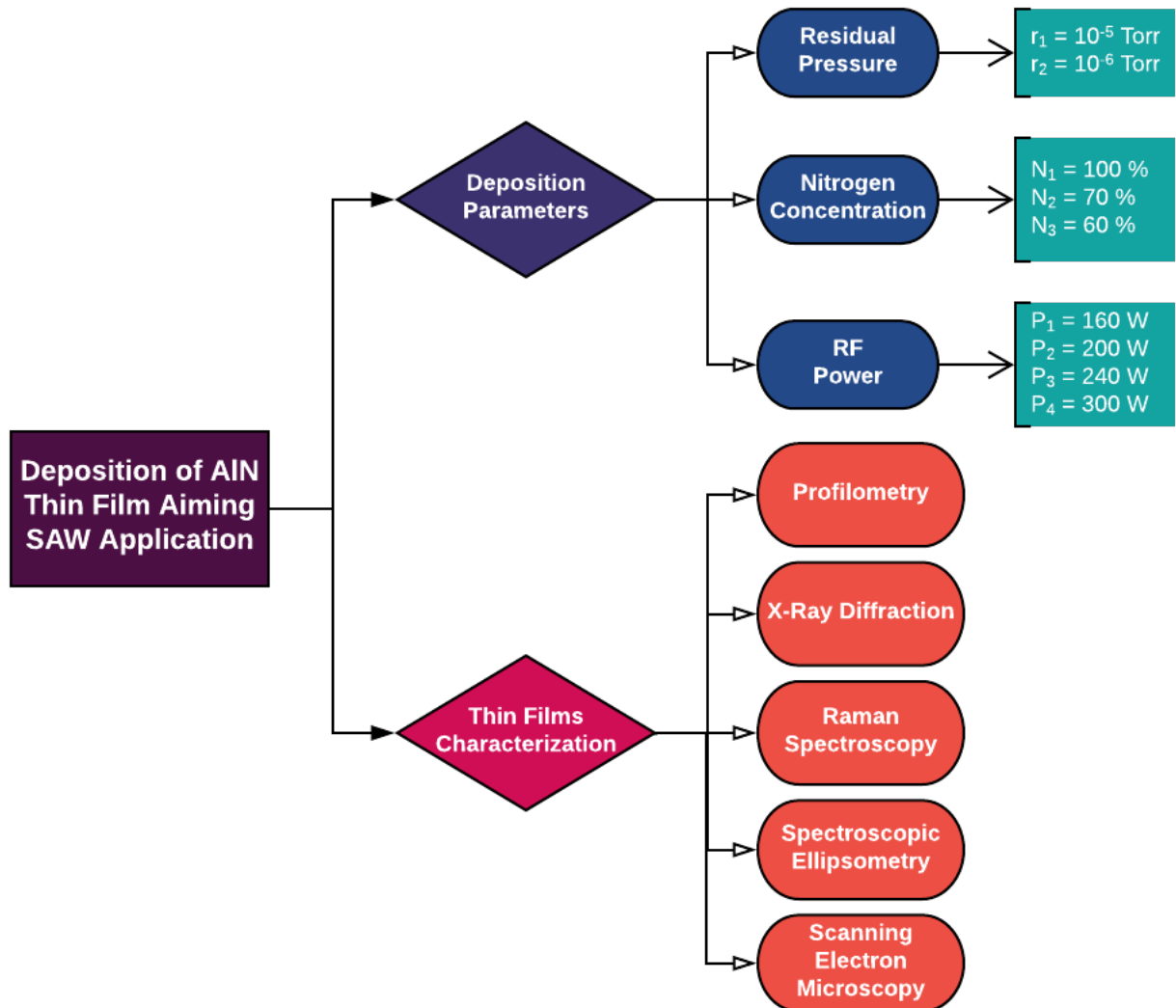


FIGURE 4.1 – Methodology diagram.

Figure 4.2 presents photography and schematic diagram of the deposition apparatus used in this work.

The depositions processes were performed in a stainless-steel cylindrical chamber with 650 mm diameter, 500 mm depth with two observation windows. The AlN thin films were deposited using a 203.2 mm in diameter magnetron cathode with a 6.35 mm thick aluminum target of 99.99% purity. The magnetron cathode is cooled by water and contain permanent magnet set inner housed generating a magnetic field with approximately 500 Gauss.

The sample holder is a flat circular support with 110 mm diameter allowing the use of silicon wafers up to 101.6 mm in diameter. The substrate holder also has a vertical degree of freedom which allows varying the distance between the substrate holder and the target. Between the sample holder and the target, there is a shutter so that when the target is being cleaned the substrate is protected and not contaminated by the ejected oxides and impurities of the target. A type K thermocouple is fixed in the sample holder surface to

monitor the temperature during the deposition process.

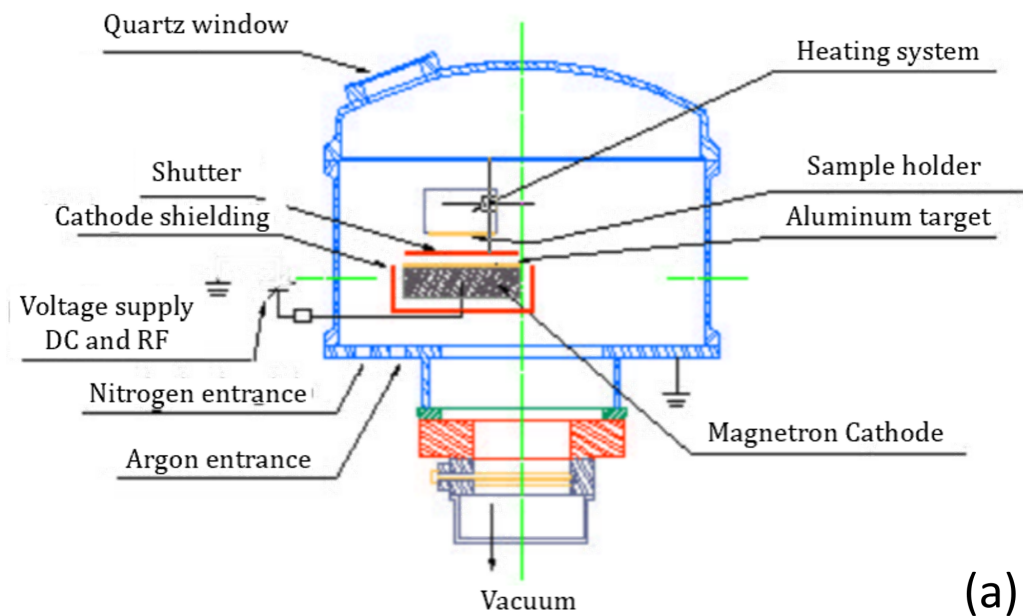


FIGURE 4.2 – (a) Magnetron sputtering system used to deposit AlN thin films. (b) Schematic drawing of the vacuum chamber with its main constituent parts. (BRITO, 2014)

The gas injection system is composed of gas flow controller system (MKS 247C model) coupled to four mass flow controllers (1159B-MKS model) with maximum flow rate of 100,

200, 20, 50 sccm used for argon, nitrogen, oxygen and hydrogen injection, respectively. However, only these controllers do not guarantee complete closure of their needle valves and leakage may occur. Therefore, the plasma system has pneumatic on/off valves between the mass flow controllers and the chamber to ensure complete closure of the gas injection circuit.

The vacuum system is composed of a mechanical pump (E2M-18 model, Edwards) and a diffusion pump (Diffstak model, Edwards). The latter one is cooled by a thermostat water bath equipment (TE-184 model, Tecnal) and it has a trap of liquid nitrogen to prevent the plasma chamber contamination by oil vapors back-stream.

The residual and working pressure are measured by Ion Gauge and Baratron type pressure meters, respectively.

The power supply system consists of an analogical radio-frequency source connected by BNC cable to the magnetron cathode. This system is composed of an RF power supply (RF Generator - ENI: Model ACG - 10B) and an RF impedance matching antenna (Plasma-Therm: Model 1000E) that can be set manually or automatically. This equipment allows applying power between 0 - 1000 W with a resolution of 20 W.

## 4.2 Parameters for Thin Films Deposition of AlN

The AlN thin films were deposited on crystalline (100) p-type silicon substrate with 1-10  $\Omega - cm$  resistivity and on microscope glass slides. Both of them were positioned in the center of the sample holder and maintained 50 mm distant from the target. This distance was determined by the literature as acceptable because it is within the range of 30 to 70 mm to get oriented AlN in the crystalline plane h-(002). (IRIARTE *et al.*, 2010) (XU *et al.*, 2001)

The silicon wafer was cleaned by a standard process called RCA-1. This procedure removes organic residues and elimination of native oxides on the silicon wafer surface. It is based on  $H_2SO_4$  (sulfuric acid) and  $H_2O_2$  (hydrogen peroxide) for the decontamination of organic materials and on HF (fluoride acid) for native oxides elimination. This ensures an effective cleaning by reducing or eliminating impurities in the substrates. The microscope glass slides were previously cleaned by a chemical procedure with  $C_3H_6O$  (acetone) and  $C_3H_8O$  (isopropyl alcohol) in ultrasound (15 min each) and rinsed in deionized water.

Before each deposition process, the deposition chamber was pumped out for approximately two hours to reach a residual pressure of  $1 \times 10^{-4}$  Pa ( $1 \times 10^{-6}$  Torr). During this period the substrate holder was heated up to 150 °C for 20 minutes to help the system vacuum cleaning. Then, the heating was turned off and waited the temperature came back

to room temperature prior to the deposition process. Prior to the deposition process, the target was cleaned (pre-sputtering) for 40 minutes. During the deposition process, the heating device was turned off. The deposition parameters investigated were: RF power (160, 200, 240 and 300 W); nitrogen flow rate (6, 7 and 10 sccm) and residual pressure (1 mPa and 0.1 mPa -  $10^{-5}$  and  $10^{-6}$  Torr) that are detailed for each sample on Table 4.1.

TABLE 4.1 – Experimental parameters.

<b>Sample</b>	<b>Power Supply (W)</b>	<b>Nitrogen Concentration (%)</b>	<b>Residual Pressure (Torr)</b>
S200-N100-P5	200	100	$5 \times 10^{-5}$
S200-N70-P5	200	70	$5 \times 10^{-5}$
S200-N100-P6	200	100	$2 \times 10^{-6}$
S200-N70-P6	200	70	$2 \times 10^{-6}$
S200-N60-P6	200	60	$2 \times 10^{-6}$
S160-N70-P6	160	70	$2 \times 10^{-6}$
S240-N70-P6	240	70	$2 \times 10^{-6}$
S300-N70-P6	300	70	$2 \times 10^{-6}$

The deposition time was fixed in 240 minutes (4 hours) and the work pressure was kept at 0.27 Pa (2 mTorr) for all deposited samples.

### 4.3 Film Characterization Techniques

The characterization techniques were chosen to determine the film thickness, the chemical composition, chemical bond structures and the crystallographic orientation of the deposited material.

- **Profilometry**

To measure the thickness of the deposited films was necessary to use a mechanical mask covering the sample during the deposition process with a silicon piece. The step formed on the surface sample presents a region with aluminum nitride deposited and other uncoated, just the silicon substrate.

The high of the formed steps on each sample, that gives us the coating thickness, were measured by mechanical profilometry using a profilometer (KLA Tencor - P-7) available at Laboratório de Caracterização de Materiais (LabMat) from Laboratório de Plasmas e

Processos (LPP) of Instituto Tecnológico de Aeronáutica (ITA) and an optical non-contact profilometer (Cyber - CT 100) situated in the Centro de Competência em Manufatura (CCM), a laboratory associated of ITA.

The stylus profilometer has as principle the displacement measurement of a contact sensor (diamond-tipped needle) that slowly scans from the step created between film to substrate, acquiring the substrate profiles of its surface. With this profile is localized the film step and is measured the vertical distance between the substrate surface and the film surface resulting in a thickness measure. In all samples were realized five thickness measurements in distinct regions of step in order to verify possible non-uniformities in the film thickness. All these evaluations are made by the software Profiler 8.0.

The method measures the film thickness was determined using a non-contact profilometer through a chromatic white light sensor. The confocal microscope of chromatic aberration can define the thickness gap between the substrate and the deposited films. The software used to analyze the sample measurement is the ASCAN Software that allows obtaining a comprehensive profile, 3D and roughness analyses conforming to DIN ISO. The method was set to analyze an area of  $12\text{ mm} \times 2\text{ mm}$  with lowest superficial defects. The scan was realized with  $10\text{ nm/s}$  and the light was set to 70%. In all samples were collected three measurements in different regions of the step-in order to verify possible non-uniformity in the film thickness. With this technique was possible to acquire data as the height average, the RMS roughness ( $R_q$ ) and a 3D projection of the surface and demonstrate the thickness step, estimating the thickness of deposited film.

The thickness values presented is this work for each sample are the mean values of the measures performed by the mechanical (5 measurements) and optical profilometers (3 measurements). The error bar was obtained by the standard deviation of the eight measurements.

### • X-Ray Diffraction

The XRD (X-Ray Diffraction) is a technique used to material analysis, providing information as crystallinity, grain size, stress and crystal orientation. It uses a monochromatic beam of X-Ray to determinate interplanar spaces of the analyzed material. (ZACHARIASEN, 2004) This technique stands out from the other of microstructural material characterization techniques because it does not need complex methods for the sample preparation, is a non-destructive technique and allows the analysis of heterogeneous materials with phase mixing. (CULLITY, 1978)

The plane orientation of material can be defined by this scattered process, once each crystallographic orientation has a distinct diffraction angle. This distinction is obtained through Bragg laws, which correlates the incident beam wavelength ( $\lambda$ ) with a distance

of adjacent planes ( $d$ ) and diffraction angles ( $\theta$ ). The Bragg law is described in Equation 4.1. (CULLITY, 1978)

$$n\lambda = 2d \sin \theta \quad (4.1)$$

The peak shapes and width of the X-ray diffraction are determined by the microstrains, crystallite size and the instrumental operation setup. For example, the diffraction peak is broadened with the presence of small crystallite and/or heterogeneous microstrains (Figure 4.3). (ICHIKAWA, 2013)

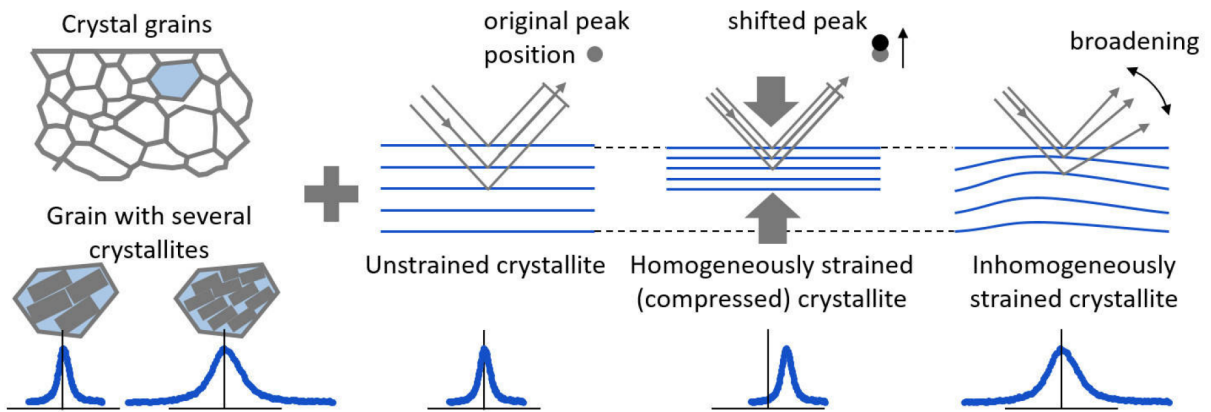


FIGURE 4.3 – Contributions of the materials' structure to the line broadening of diffraction profiles. (NOYAN; COHEN, 1987) Adapted from (ROBATTO, 2017)

The profile diffractions of the samples are treated following a *Voigt* function, which is the results of the convolution of *Gaussian* ( $\beta_G^f$ ) that describes the enlargement of the profile related to the microdeformations and *Lorentzian* ( $\beta_L^f$ ) that describes the enlargement related to the mean crystallite size (Figure 4.4). (LANGFORD *et al.*, 1991) (ICHIKAWA, 2013) The  $K\alpha_2$  separation also was treated, once the spectra are symmetrical for this function assumptions. With these functions is possible to analyze the full width of half maximum (FWHM), peak area and the intensity of microstrains. (WARREN, 1959)

The crystallite size is reported in nm for each individual crystallographic phase. The crystallite size is the average size of a coherent scattering domain (perfect arrangement of unit cells or perfect crystal). The crystallite size may affect some properties of the material as dissolution, material strength, catalytic activity, product aging to state few. It is important to take into account that crystallite size and grain size is not necessarily the same thing, since a grain may be composed of multiple crystallites.

The traditional measurement of crystallite size is by the Scherrer equation, which shows that the crystallite size is inversely proportional to the peak width ( $\beta_L^f$ ), which is the FWHM fitted in the peak, using Equation 4.2. Where  $\lambda$  is the wavelength of the X-Ray,  $\theta$  is the angle of Bragg diffraction and  $k$  is a constant in a range of 0.62 to 2.08

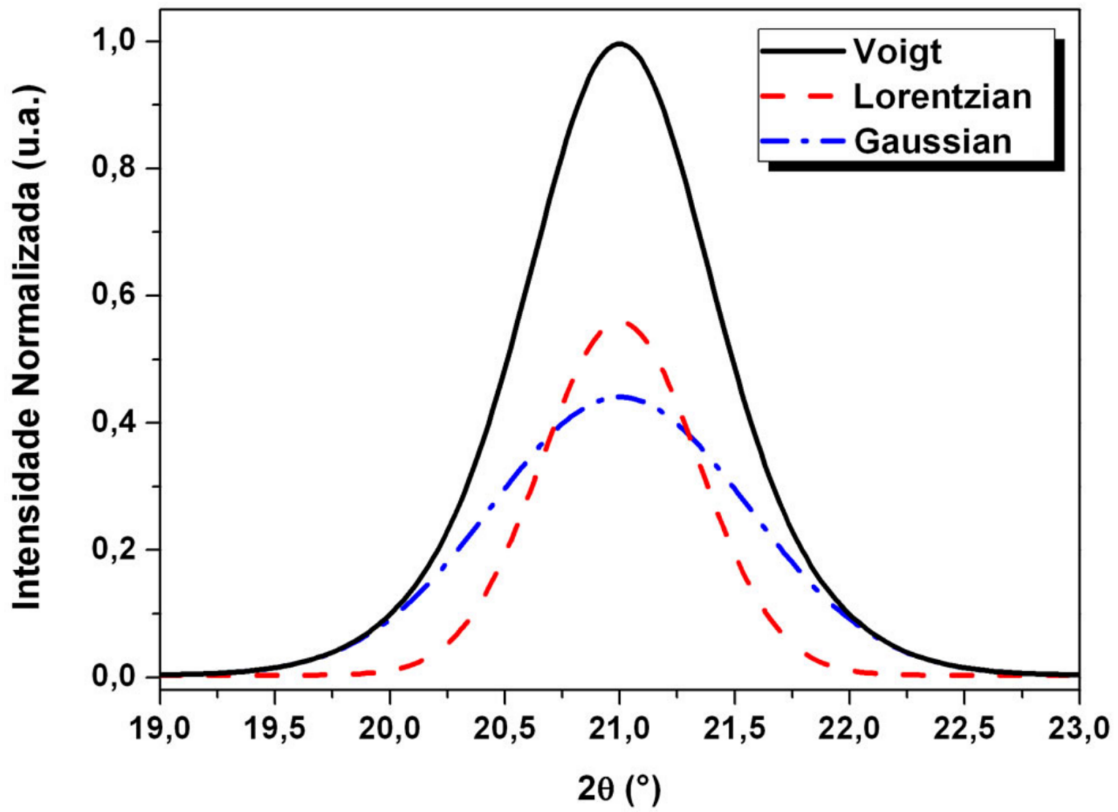


FIGURE 4.4 – The convolution of a Gaussian function (dash-dot line) and Lorentzian (dashed line) provide a Voigt function (continuous function). (ICHIKAWA, 2013)

which depends on the crystallite shapes in this work was considered spherical particles, so the  $k$  used was 0.9. (CULLITY, 1978)

$$C = \frac{k\lambda}{\beta_L^f \cos\theta} \quad (4.2)$$

Note that one average crystallite size is reported for the entire sample and the crystallite size distribution can be estimated.

Therefore, Stokes and Wilson (1944) defined Equation 4.3 to determine the microstrains. (LANGFORD; WILSON, 1978)

$$\varepsilon = \frac{\beta_G^f}{4 \tan \theta} \quad (4.3)$$

The  $\varepsilon$  is the range of microstrains that is the results from the extreme values of lattice spacing. (LANGFORD; WILSON, 1978)

The X-Ray diffractometer used in the present work was a PANalytical Empyrean and the obtained data were treated using the HighScore software. The measurements were performed using  $Cu K\alpha$  radiation with wavelength of 1.5418 Å. The equipment is located

in LabMat of LPP-ITA.

- **Field Emission Gun Scanning Electron Microscopy**

The Field Emission Gun Scanning Electron Microscopy (FEG-SEM) was used to evaluate the surface morphology of the deposited AlN thin film such as the presence of imperfections and the formation of structures. The energy-dispersive X-ray spectroscopy (EDX) technique was used to investigate chemical characterization and elemental composition measurements. The equipment used to realize both techniques was Vega3 by TESCAN operated at 30 kV at Laboratório Associado de Sensores e Materiais (LAS) from Instituto Nacional de Pesquisas Espaciais (INPE).

- **Raman spectroscopy**

Raman spectroscopy is widely used to detect the phonon vibration properties in materials and is also a practical method for studying stress of III-IV semiconductor including AlN. (WANG *et al.*, 2013) In addition, it has the advantage of being a non-destructive, non-contact character and do not need special sample preparation. (BUMBRAH; SHARMA, 2015)

The Raman spectroscopy consists to analyze the vibration state of material molecules correlating the energy of the scattered photons with the Raman displacement around a wavelength of incident laser radiation. This direct analysis is called Stokes and anti-Stokes wavenumbers. (SMITH; DENT, 2005)

According to the group theory, hexagonal wurtzite AlN structure belongs to the space group ( $C_{6v}^4 - P6_3mc$ ) with four atoms in the unit cell. (MCNEIL *et al.*, 1993) Theory analysis predicts six optical vibration modes. (DAVYDOV *et al.*, 1998) The optical modes are represented as  $A_1 + 2B_1 + E_1 + 2E_2$ , being the modes  $A_1$ ,  $E_1$  and  $E_2$  Raman actives and the  $B_1$  modes are silent (FILIPPIDIS *et al.*, 1996). The  $A_1$  and  $E_1$  modes are polar modes, which mean that the energies of these modes depend on the direction of propagation of the phonon relative to the optical axis (MCNEIL *et al.*, 1993). In addition, they are divided into longitudinal optical (LO) and transversal optical (TO). (FILIPPIDIS *et al.*, 1996)

The Raman was analyzed by glass and the spectra are analyzed observing the peaks characteristics as shown in Figure 4.5. The peak positions are responsible to identify the molecular structure of material analyzed. The height of the peak is correlated with the substance concentration and the width of the peak indicates the crystallinity of the material, Figure 4.5-(a). The Raman Shift (the shift of the peak position) can indicate the presence of residual tensile or compressive stress inside the crystal.

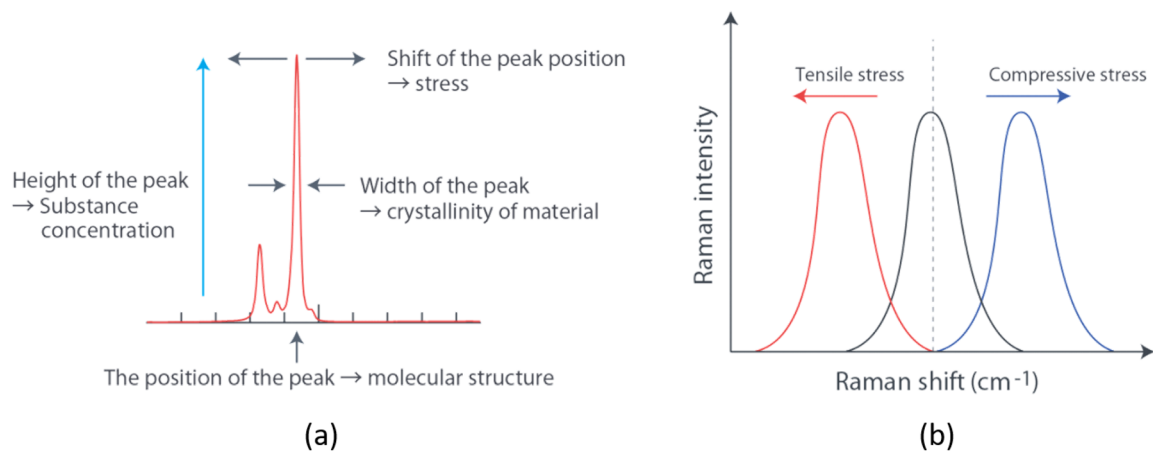


FIGURE 4.5 – Raman spectra (a) mainly characteristics; (b) with peaks shifted and the correlation with the residual stress. (NANOPHOTON, 2018)

To analyze it, is used the method FWHM of the  $E_2^{high}$  band measured in the samples. According to KUBALL *et al.* FWHM around of  $3\text{ cm}^{-1}$  is reported for the highest quality of aluminum nitride bulk single crystals and PERLIN *et al.* reported that  $50\text{ cm}^{-1}$  for highly defective crystals. So, any intermediate value of FWHM of a Raman peak indicates that the AlN films present high quality, however, it is not free of any concentration of defects, as shown in the Figure 4.5-(b). (KANG *et al.*, 2005) (LUGHI; CLARKE, 2006)

In addition, the difference between peak positions, the difference of intensity ratio and the presence or absence of a specific peak are characteristic that defines that the material is formed by polymorphs crystal (Figure 4.6). This kind of material occurs when the chemical composition is the same, but the crystal structure is different. (WARREN, 1959)

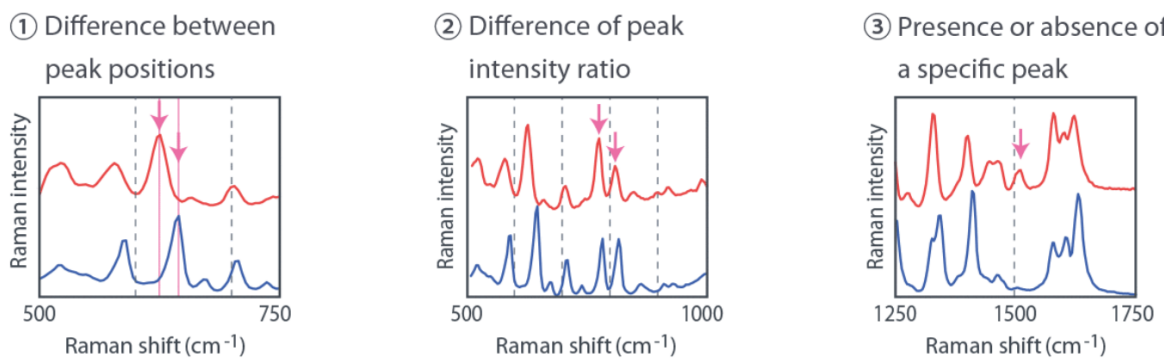


FIGURE 4.6 – Identification of crystal polymorphs. (NANOPHOTON, 2018)

The Raman spectra are also used to identify the energy characteristics of chemical bonds or distinguish different phases within the same material. (SMITH; DENT, 2005) The Raman spectroscopy was used to study the AlN films deposited on glass, using a LabRAM Horiba Evolution equipment with a Neodymium (Nd) solid state laser - YAG at 532 nm. The LabRAM HR Evolution uses the Lab Spec 6 software to data acquisition

and analyses of the spectra. The system is installed at Laboratório de Caracterização de Materiais (LabMat) of Laboratório de Plasmas e Processos (LPP) of ITA.

### • Variable Angle Spectroscopic Ellipsometry

Variable angle spectroscopic ellipsometry (VASE) is an optical technique for investigating the dielectric properties (complex refractive index or dielectric function) of thin films. Ellipsometry is based on the measurement of the change of polarization upon reflection or transmission and compares it to a theoretical model. The ellipsometry technique consists of a measurement of polarization variation of light after it is reflected or transmitted from the sample. The obtained data is analyzed using a model that considers the substrate, the film and its roughness. The experimental curves are fitted with the data obtained from the model curves. By varying the parameters values of the AlN film in the model the theoretical data approach the model curve with the experimental data curve, then the desired data values are obtained as shown in Figure 4.7. (HORIBA, 2008) The polarization change is affected by the optical properties and the film thickness and is described by amplitude ratio ( $\psi$ ) and phase difference ( $\Delta$ ). (TOMPKINS *et al.*, 2005) The ellipsometry technique can evaluate the multi-layered film providing parameters of each layer. (KIM; VEDAM, 1988)

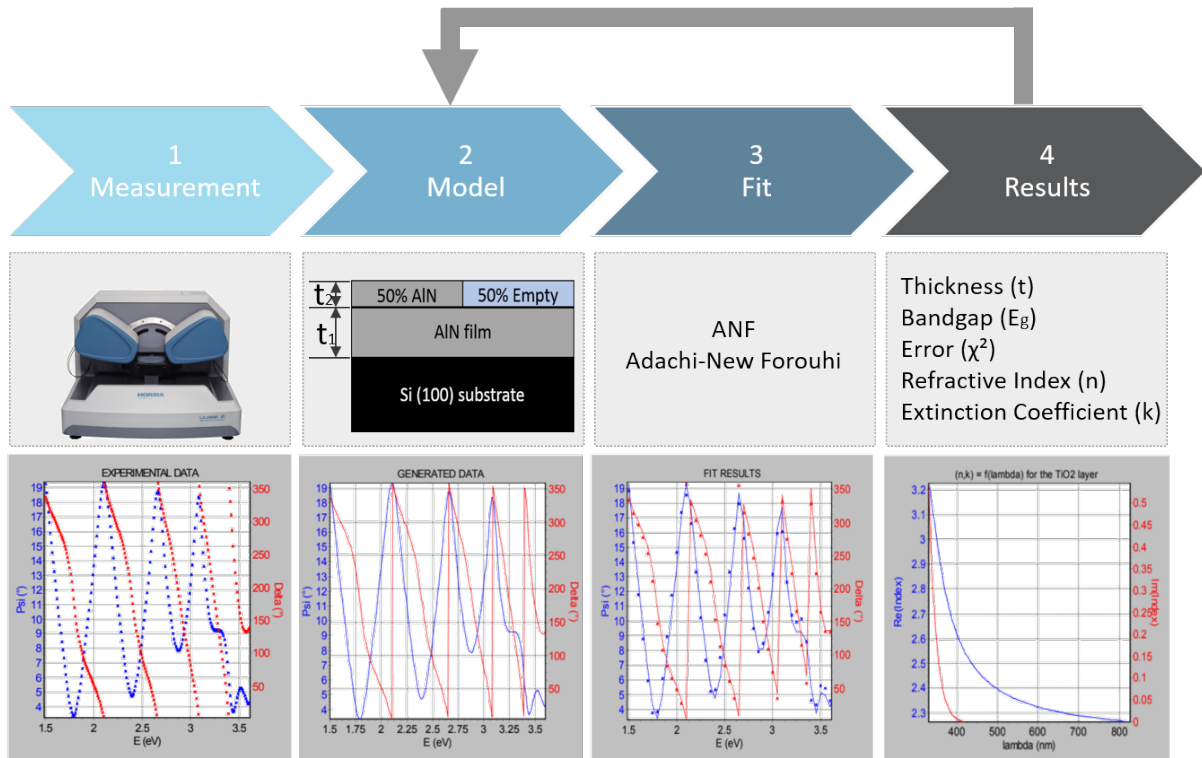


FIGURE 4.7 – Spectroscopic ellipsometry methodology. Adapted from (HORIBA, 2008)

It can be used to characterize the material composition, roughness, thickness (depth), crystalline nature, doping concentration, refractive index, extinction coefficient, electrical

conductivity, bandgap and other material properties. It is a nondestructive and very sensitive technique to the change in the optical response of incident radiation that interacts with the material being investigated. (LOSURDO; HINGERL, 2013)

The ellipsometry also can be utilized in-situ monitoring of thickness and refractive index of the growing film which are interesting to understand the thin film growth mechanism. (MENG *et al.*, 1993) (NAKAMURA, 1991) The refractive index ( $n$ ) of AlN at 632.8 nm varies depending on its structural order: 1.8 - 1.9 for amorphous films, 1.9 - 2.1 for polycrystalline films, and 2.1 - 2.2 for epitaxial films. (EDGAR, 1994)

The operating principle of ellipsometry applied in this work is denominated polarization modulation ellipsometer (PME), it shows optimized acquisition speed and a larger spectral range from the IR to the UV. The high acquisition speed is due to the presence of photoelastic modulator (PEM) whose acquisition frequency is around 50kHz. The drawbacks of this ellipsometer are the chromatic behavior of the modulator and the sophisticated optical calibrations. This type of ellipsometer allows extremely accurate results, thanks to the high performing electronic system.

The measurement of this technique yields experimental data that needs to be fitted to a model to determinate the unknown sample parameters. So, for this is considered an error denominated as goodness of fit (GOF) that is defined through  $\chi^2$  that present low values to a good fit, as shown in Equation 4.4. The spectra of  $\Psi$  and  $\Delta$  then the  $\chi^2$  value is compared to each theoretically calculated pair ( $\Psi_{th}$ ,  $\Delta_{th}$ ) and the experimental determined pairs ( $\Psi_{exp}$ ,  $\Delta_{exp}$ ).

$$\chi^2 = \min \sum_{i=1}^n \left[ \frac{(\Psi_{th} - \Psi_{exp})_i^2}{\Gamma_{\Psi,i}} + \frac{(\Delta_{th} - \Delta_{exp})_i^2}{\Gamma_{\Delta,i}} \right] \quad (4.4)$$

with  $\Gamma_i$  the standard deviation of each data point.

The measurements were performed from 0.6 to 6.5 eV with 0.02 eV steps at an angle of 70°. Each sample measured generate four curves ( $I_s$  and  $I_c$ ) for each incident angle. After the measurement of samples, the modeling process is realized, it is the experimental curves of each sample are fitted for curves generated by the software of DeltaPsi available with the equipment used.

The optical constants for the elliptic constants were determined through fitting the elliptic constants with the Adachi-New Forouhi (ANF) dispersion model. The mathematical model uses relations called dispersion formula that help to evaluate the optical properties of the material by adjusting specific fit parameters. For this work, was used the Tauc-Lorentz dispersion formula that works particularly well for amorphous material exhibiting an absorption in the visible and/or far ultraviolet (FUV) range (absorbing dielectrics, semiconductors and polymers). (HORIBA, 2008)

The equipment used was an UVISSEL 2 Spectroscopic Ellipsometry from HORIBA driven by the DeltaPsi2 software. It is also installed at LabMat of Laboratório de Plasmas e Processos (LPP) of ITA.

# Chapter 5

## Results and Discussion

In this section is presented the results and discussions obtained for each parameter set chosen to the deposition process of AlN thin films and their characterization according to the morphology and structure crystallinity of the deposited thin films.

The influence of parameter set on each sample, such as residual pressure, nitrogen concentration and applied RF power is discussed below.

### 5.1 Film Deposition and Thickness

As mentioned on the experimental procedures, Chapter 4, this work is based on deposition and characterization of eight samples grown at the conditions described in Table 4.1.

The variation of the substrate temperature as function of the time during the deposition process for all deposited samples is presented in Figure 5.1. The temperature increases linearly at a rate of about 1.2 degrees/min during the pre-sputtering process (first 40 minutes) and continues to increase at the same rate during the first 30 minutes of deposition process (total time 70 minutes). After that, the heating rate decrease and the sample temperatures reach the maximum values that are in the range of 110 to 130 °C that were maintained constant up to the end of the deposition process, except for sample S300-N70-P6. The maximum temperature value for each sample depends upon the variation of the deposition power and/or the nitrogen content on the gas mixture, once the pressure was kept at 0.27 Pa (2 mTorr) for all samples.

In the case of sample S300-N70-P6, grown at 300W, the temperature takes a longer time (120 minutes) to reach the maximum value (about 175°C). The temperature also presented a higher variation (about  $\pm 5^\circ\text{C}$ ) value compared with the other sample ( $\pm 2^\circ\text{C}$ ), which indicates that the plasma presents some instability at this condition of high

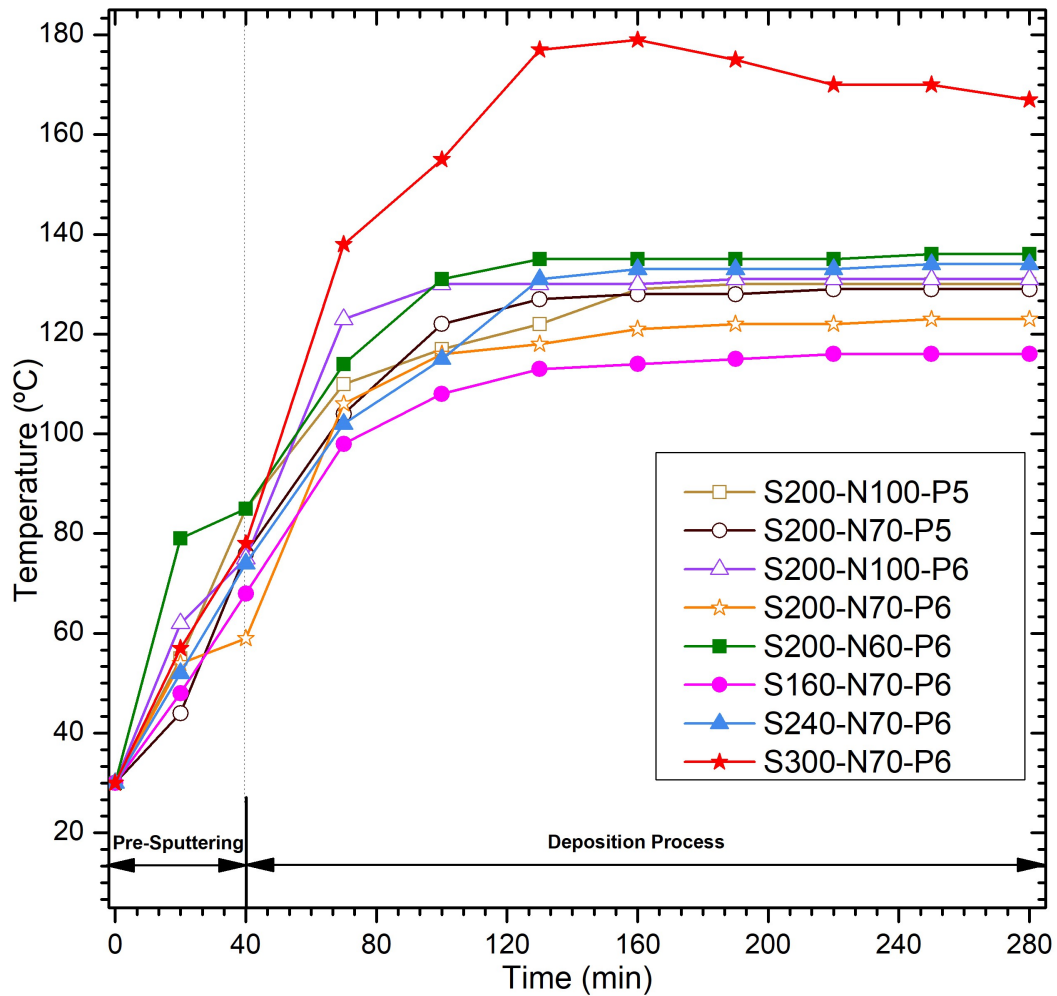


FIGURE 5.1 – Sample heating rate during the deposition process. The heating was caused only by the plasma process.

RF power (300 W) and low deposition pressure (0.27 Pa - 2 mTorr). For RF power higher than 300 W and at this pressure, the plasma starts to present some small sparks.

Figure 5.2 shows the images, obtained by chromatic aberration microscopy (CAM), of part of the surface of all samples. The images were obtained in samples areas partially covered during the deposition process in order to leave a step to measure the coating thickness. The film thickness values obtained, as well as, the surface roughness are presented in Table 5.1. The surface roughness increases with the increase of the applied RF power most probably due to the increase of the deposition rate and high energy bombardment of the impinging species on the coating surface.

Figure 5.3 presents the AlN film thickness as function of the nitrogen content in the gas phase for all deposited samples and these values are summarized in Table 5.1. The thickness evolution can be better observed in Figure 5.4, where is presented the thickness versus RF power only for samples deposited with 70% of nitrogen in the gas mixture, but the case of sample S200-N70-P5 will be discussed later. As expected, the thickness

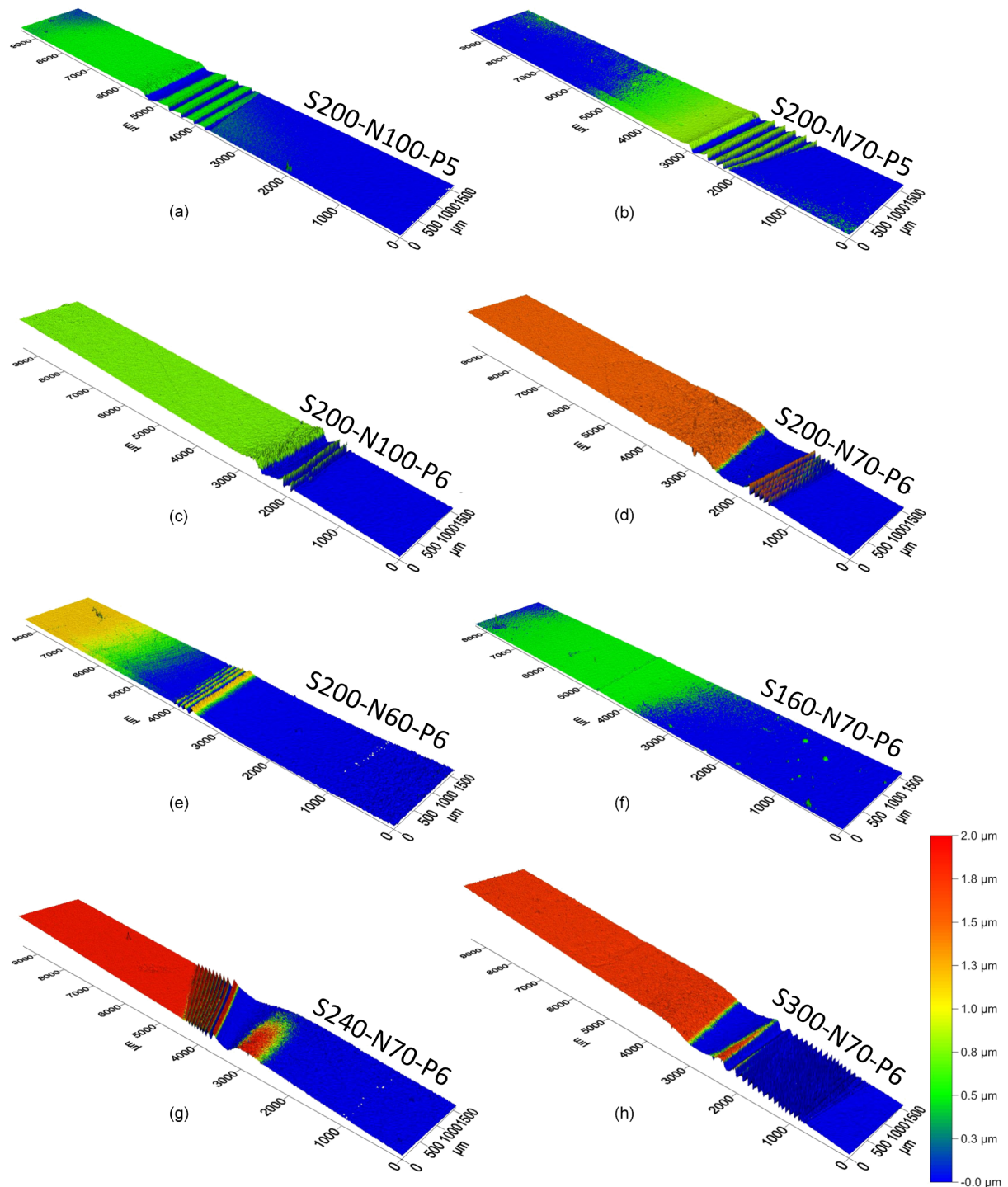


FIGURE 5.2 – Images of the sample profiles obtained by CAM.

increases linearly with the RF applied power up to about 200W. This is associated with the increase of the RF energy supplied, which gives an increase of density of ionized species in plasma and the increase of energy of particles hitting the target enhancing the ejection rate of the material. Then, the deposition rate starts to decrease for higher values of RF power and in these cases reaches a plateau at thickness of about 1800 nm. The decrease in the deposition rate when high RF power is applied can be associated with the increase

of the plasma volume that will cover all the substrate surface producing a re-sputtering process of the deposited AlN thin film, once the sample is only 50 mm from the magnetron cathode surface.

TABLE 5.1 – Thickness and roughness of AlN thin films by profilometry technique.

Sample	Power Supply (W)	Nitrogen Concentration (%)	Thickness (nm)	Roughness (nm)
S200-N100-P5	200	100	595±20	71±13
S200-N70-P5	200	70	785±10	83±35
S200-N100-P6	200	100	712±42	111±8
S200-N70-P6	200	70	1410±89	142±17
S200-N60-P6	200	60	1277±67	173±28
S160-N70-P6	160	70	555±20	302±6
S240-N70-P6	240	70	1823±28	84±11
S300-N70-P6	300	70	1833±56	244±18

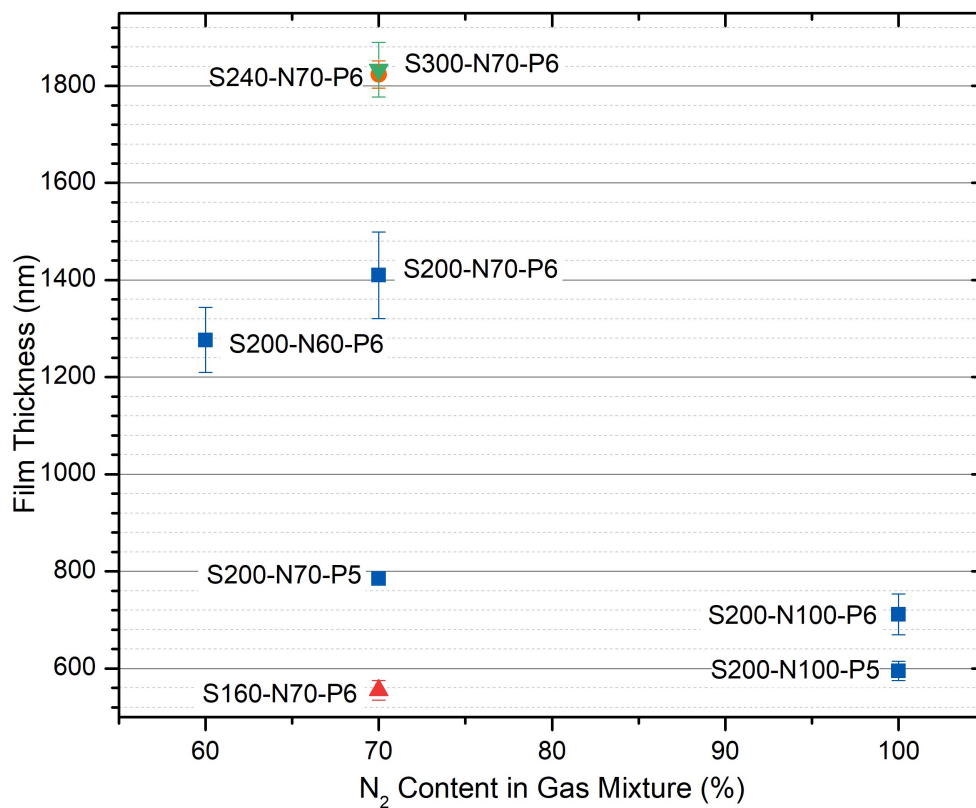


FIGURE 5.3 – Thickness samples as function of the nitrogen content in the gas mixture.

The deposition rate of the two samples deposited at the same RF power and nitrogen content (S200-N100-P5 and S200-N100-P6) presented a quite different deposition rate.

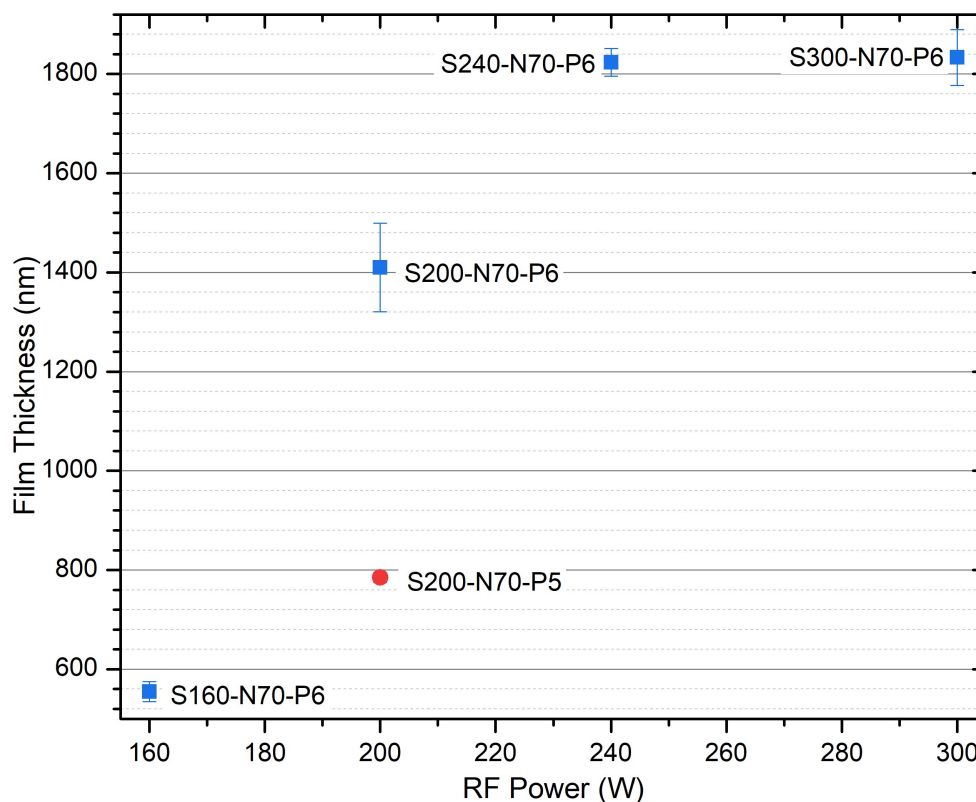


FIGURE 5.4 – Thickness of the samples deposited with 70%  $N_2$  as function of the applied RF power.

This difference may be associated mainly with different residual pressure. In the case of higher residual pressure, the plasma atmosphere has the presence of high amount of oxygen that is highly reactive compared with nitrogen. The oxygen reacts with the target surface forming an oxide rich ceramic thin film (oxynitride), target poisoning effect, that has lower sputtering yield compared with aluminum nitride formed in the target surface in the case of deposition at lower base pressure. Despite that, the electronegativity of oxygen and the formation of negative ions in the plasma turn it less efficient than nitrogen to eject atoms from the target surface. The high base pressure during the deposition process of the sample (S200-N100-P5), occurred by the presence of some leak in the plasma reactor and the residual pressure reached only 7 mPa ( $5 \times 10^{-5}$  Torr), leaving to deposition of an amorphous AlN as will be shown by the X-ray and Raman characterization. The chemical composition obtained by EDX for the samples S200-N100-P5 and S200-N70-P5 (both deposited with higher residual pressure) presented high oxygen concentration in the film compositions indicating that was deposited an aluminum oxynitride film. The measured chemical composition for sample S200-N70-P5 was 32.1 % O, 26.8% N and 41.1% Al.

## 5.2 X-Ray Diffractometry

The diffractograms of all deposited samples are presented in Figure 5.5.

As the AlN thin films were deposited to silicon wafer, it can be observed the presence of the silicon peaks assigned to the orientations (200) at  $33^\circ$  and (400) at  $61.7^\circ$ , as shown in the diffractogram of Figure 5.6. The sample S200-N100-P5 did not present evident diffraction peak indicating that the deposited film is amorphous. Sample S200-N70-P5 presented a small diffraction peak at about  $36^\circ$  which can be assigned to the plane h-(002) of AlN. The assignment of the XRD peaks to Wurtzite AlN structure was based on International Centre for Diffraction Data JCPDS card # 01-070-2545 and the peak position for the plane h-(002) is  $2\theta = 36.023^\circ$ .

As mentioned earlier, these two samples, S200-N100-P5 and S200-N70-P5, were grown when the reactor presented a small leak and the residual pressure obtained was only 7 mPa ( $5 \times 10^{-5}$  Torr). This effect decreased the deposition rate, once they presented only about 600 and 800 nm thick, respectively, and high level of contaminants, mainly oxygen, shown by the EDX analysis, illustrated in Figure 5.7. This fact shows that to grow well oriented aluminum nitride thin film, the gas mixture must be well controlled and free of oxygen.

For the other samples S200-N100-P6 to S300-N70-P6, the diffractogram presented a hexagonal structure of wurtzite that is indicated by a well-defined peak h-(002) at  $2\theta = 36.023^\circ$ . (CHENG *et al.*, 1996) Sample S<sub>8</sub> also presented the diffraction peak at  $2\theta = 33.2^\circ$  that is not an AlN peak because no AlN peak is located at  $2\theta$  position smaller than that of AlN h-(002) according to the powder pattern of JCPDS card #25-1133.

For (100) oriented silicon wafer examined with Cu  $K\alpha$  radiation, the only diffraction peak expected is (400) reflection because other (100) reflections are forbidden due to their vanishing structure factors (CULLITY, 1978). This peak is easily differentiated from the thin film peaks due to its high intensity and low FWHM. Although the corresponding interplanar spacing coincides exactly with the (200) reflection of silicon, Si that forbidden as mentioned above, see Figure 5.6. (CULLITY, 1978) In fact, this peak originates from the multiple diffractions that are the result of consecutive diffractions by different planes. (CHANG, 1984) It means that the diffracted beam from the first set of reflecting planes serves as the incident beam of the second set of reflecting planes, and the diffracted beam may be diffracted further by other planes. This results that the final diffracted beam, with respect to the original incident beam, may appear to correspond to a forbidden reflection.

However, multiple diffractions occur only when the sample is rotated (along with the sample normal) to one of the specific azimuthal angles. In the present work did not take care about of the silicon wafer orientation during the XRD measurement, and in

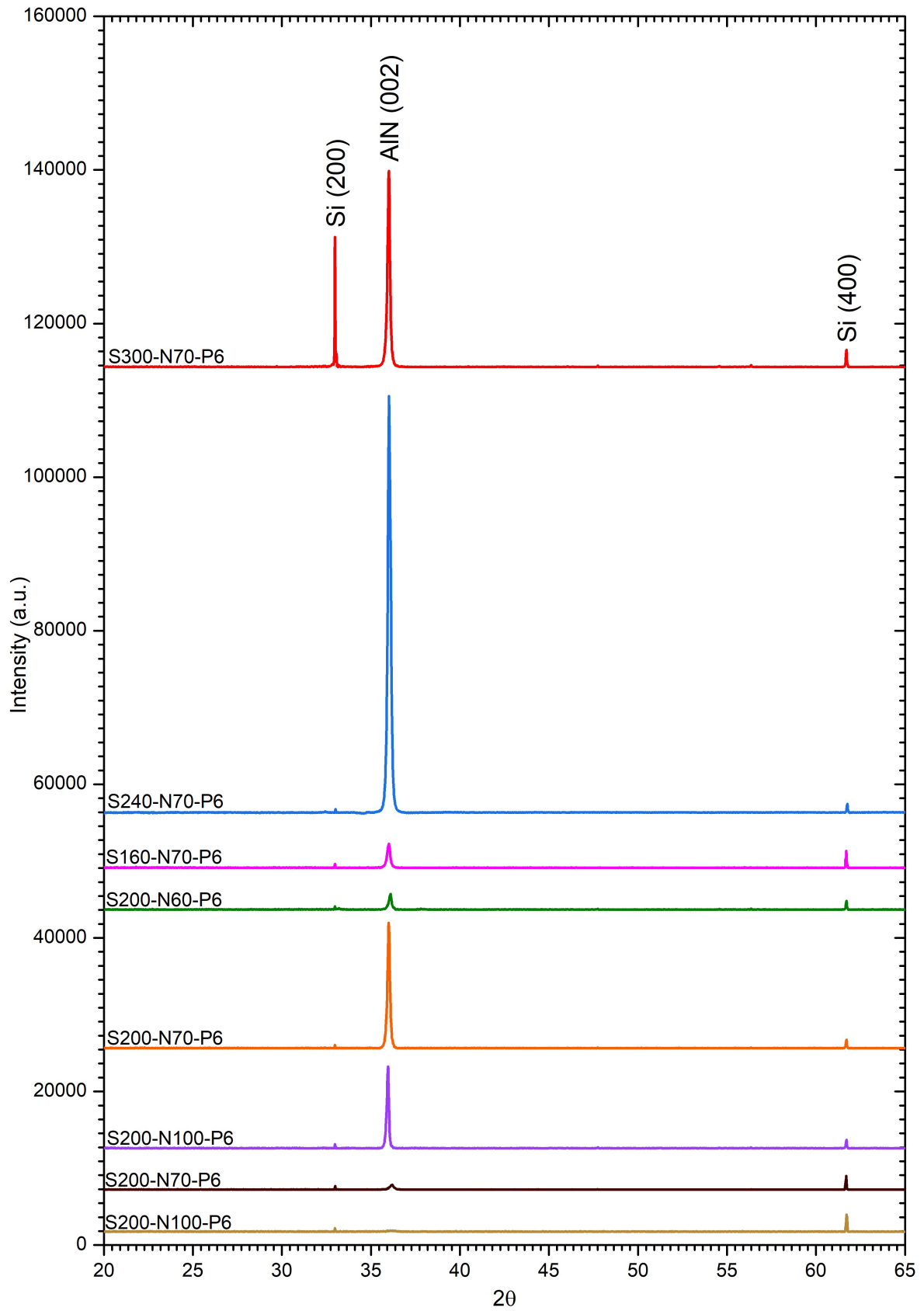


FIGURE 5.5 – XRD diffractograms for all deposited AlN thin films.

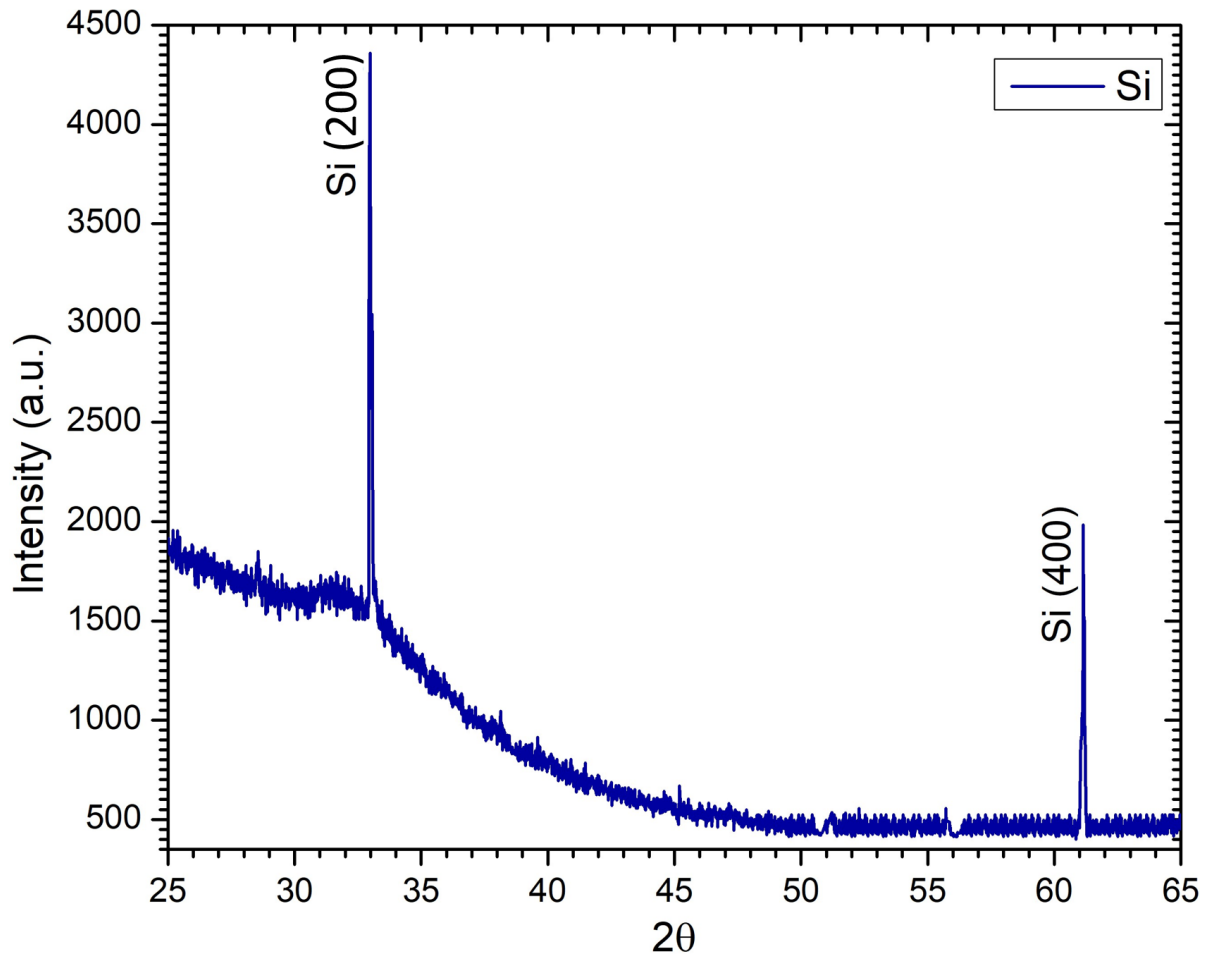


FIGURE 5.6 – Diffractogram of the type-p Si (100) used as substrate to growth AlN thin films.

particular, this sample was analyzed with a rotation that favored the multiple reflections. The effect of the Si wafer rotation in the XRD measurements of the other samples was minimized and the multiple reflections effect were not pronounced.

Table 5.2 summarizes all the information obtained from the diffractograms of Figure 5.5, as peaks positions ( $2\theta$ ), full width at half maximum (FWHM), constant from Gaussian convolution ( $\beta_G^f$ ), constant from Lorentzian convolution ( $\beta_L^f$ ), both constant result in a Voigt function described in Section 4.3, crystallite size ( $C$ ), area under the peaks ( $A$ ), coating thickness ( $t$ ),  $A/t$  ratio and intensity of microstrains ( $\varepsilon$ ).

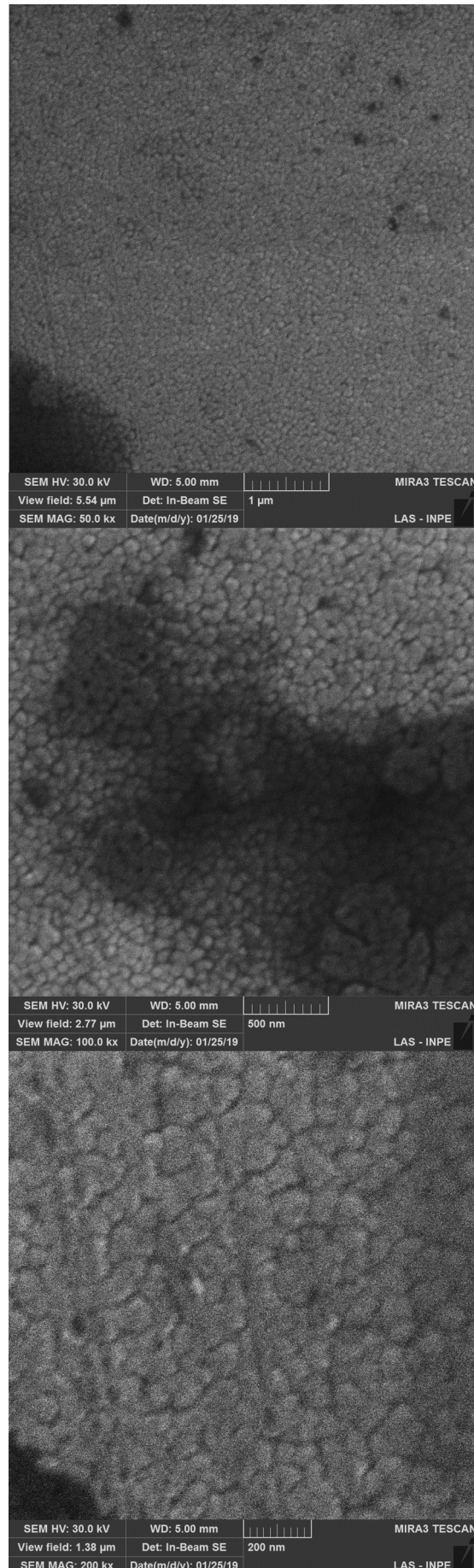


FIGURE 5.7 – Micrographies of sample S200-N70-P5 deposited AlN thin films in 200W with 70%  $\text{N}_2$  and high residual pressure ( $10^{-5}$  Torr).

TABLE 5.2 – Peaks positions ( $\theta$ ), full width at half maximum ( $FWHM$ ), Gaussian convolution ( $\beta_G^f$ ), Lorentz convolution ( $\beta_L^f$ ), crystallite size ( $C$ ), area under the peaks ( $A$ ), coating thickness ( $t$ ),  $A/t$  ratio and intensity of microstrains ( $\epsilon$ ) for all deposited samples, obtained from the XRD diffractograms of Figure 5.5.

Samples	$2\theta(^{\circ})$	$FWHM(^{\circ})$	$\beta_G^f(^{\circ})$	$\beta_L^f(^{\circ})$	$C$ (nm)	$A$ (u.arb)	$t$ ( $\mu\text{m}$ )	$A/t$ (u.arb)	$\epsilon$ (GPa)
S200-N70-P5	36.170	0.25881	0.33540	0.25200	36.8	0.37457	0.785	0.47	$4.48 \times 10^{-3}$
S200-N100-P6	35.918	0.16289	$1.29 \times 10^{-5}$	0.16289	57.0	0.20456	0.712	0.29	$1.74 \times 10^{-7}$
S200-N70-P6	36.001	0.12074	0.12381	0.10198	91.1	0.21405	1.410	0.15	$1.66 \times 10^{-3}$
S200-N60-P6	36.074	0.19085	0.08565	0.13482	68.9	0.24525	1.277	0.19	$1.15 \times 10^{-3}$
S160-N70-P6	35.990	0.20649	$4.96 \times 10^{-11}$	0.2049	45.0	0.31582	0.555	0.57	$6.66 \times 10^{-13}$
S240-N70-P6	36.029	0.22692	0.15342	0.07956	117	0.23985	1.823	0.13	$2.06 \times 10^{-3}$
S300-N70-P6	35.996	0.17484	$9.06 \times 10^3$	0.10695	86.8	0.21734	1.833	0.12	$1.22 \times 10^{-2}$

The sample S200-N100-P5 did not present an evident peak, demonstrating an amorphous structure, so for this sample is not present in Table 5.2. The h-(002) peak position of sample S240-N70-P6 at  $36.029^\circ$  are in excellent agreement with the reference value of JCPDS card ( $36.023^\circ$ ), indicating that the AlN thin film deposited in this sample is crystalline with hexagonal wurtzite structure.

Samples S200-N70-P6, S200-N60-P6, S160-N70-P6 and S300-N70-P6 also presented h-(002) peak position close to the reference value, meaning that the gas mixture containing 70% of nitrogen and 30% of argon (60%  $N_2$  + 40% Ar for sample S200-N60-P6) is an excellent condition to growth crystalline AlN film using RF power in the 160 to 300W range.

Regarding the sample S200-N70-P5, the h-(002) peak position presented a small shift to high angle ( $36.194^\circ$ ), which can be associated to a decrease of the distance of the adjacent planes of the crystalline structures as explained in Section 4.3, Figure 4.3. This effect can be produced by the presence of defects on the crystalline network, such as vacancies, which results in compressive residual stress on the film and are indicative of its amorphization.

Otherwise, the sample S200-N70-P6 presented the AlN h-(002) peak shifted to the left side ( $36.001^\circ$ ). Based on Section 4.3, this small shift can be related with the increase of the interplanar distance. Consequently, the crystalline structure presents a tractive residual stress between its adjacent planes that may indicate a non-crystalline film, allowing the presence of defects as interstitial atoms. This sample also presented high oxygen content (16.3% O, 40.5 % N and 43.2 % Al obtained by EDX) which can also contribute to the increase in the tractive residual stress. Figure 5.8 shows a micrographies of the surface of samples S200-N70-P6 (Figure 5.8-(a)) and S240-N70-P6 (Figure 5.8-(b)) obtained by FEG-SEM. In the case of sample S240-N70-P6 (crystalline with h-(002) peak at the reference position), presents an AlN film surface with large grain indicating that they had a planar growth relatively free or with low stress. Also, this sample presented low oxygen content (2.7% O, 47.1% N and 50.2% Al). On the other hand, the surface of sample S200-N70-P6 shows small grains with flapped ends indicating that the AlN film was growth at higher stress level.

The FWHM is a crystalline indicative which says that the more lattice planes with identical orientation are contributing to a diffraction peak, the sharper the diffraction pattern will be and small the FWHM will be indicating an improving in the short-range atoms ordering. The opposite (high FWHM) means that the film is losing the identical lattice plane orientation and turning an amorphous material. The highest FWHM value obtained was for sample S200-N70-P5 ( $0.28024^\circ$ ) which indicates that the AlN film is poorly crystalline for reasons already discussed above. The other samples presented small FWHM values showing that the deposited film presents a good lattice plane h-(002)

orientation as also confirmed by the very low peak shift from the reference peak position.

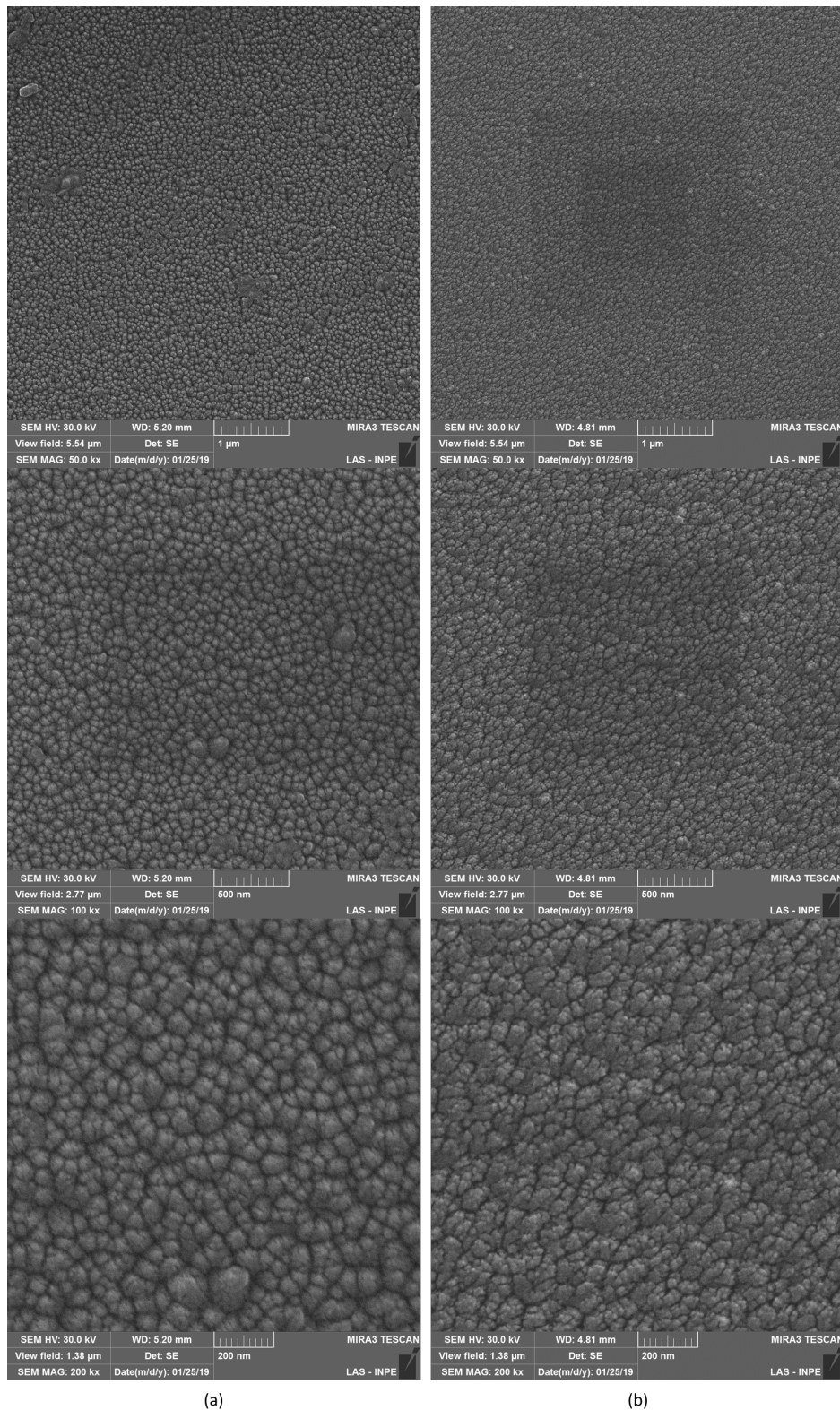


FIGURE 5.8 – Micrographies of samples deposited AlN thin films (a) S200-N70-P6 deposited with 200W and (b) S240-N70-P6 deposited with 240W in a zoom in 1  $\mu\text{m}$ , 500 nm and 200 nm.

In special the sample S200-N100-P5 presented lower FWHM (0.16289  $^\circ$ ). However, this

sample presented a small left shift in the AlN h-(002) peak indicating that the columnar deposition occurred with a tractive residual stress. This was associated with the deposition atmosphere containing 100% of nitrogen as discussed above.

As described in Section 4.3, the crystallite size ( $C$ ) is the average size of the coherent scattering domain that is the perfect arrangement of the unit cells or a perfect crystal. Sample S200-N70-P5 presented the lower value for the crystallite size (37 nm) indicating that the AlN film deposited in this sample present a small coherent scattering domain that is typical of poorly ordered structures. This result is in agreement with the ratio area below of peak curve h-(002) and the film thickness ( $A/t$ ) that gives an estimate of the quantity of crystallites responsible for the diffracted beam in the angle position. Large ratio value (0.47 for sample S200-N70-P5) indicates that there are a large number of very small crystallites and the material with crystallinity. The main reason for the small crystallite size is the elevated content of impurities (mainly oxygen) in the film due to the condition of the deposition process already discussed.

On the other hand, sample S240-N70-P6 presented the highest value of crystallite size (117 nm), showing that the AlN film deposited has a well ordered structure with large and coherent scattering domains that are in agreement with the low  $A/t$  ratio (0.13) and as can be observed by the good quality of the h-(002) peak in the diffractogram of Figure 5.5.

The other samples presented intermediate crystallite size and  $A/t$  ratio confirming that the crystalline quality of the AlN films is improved for depositions with gas mixture containing 60 to 70% of nitrogen and RF power from 160 to 240 W.

### 5.3 Raman Spectroscopy

The Raman spectra of all investigated sample deposited onto glass are illustrated in Figure 5.9 and the Raman parameters are summarized in Table 5.3. The AlN films deposited on glass substrates were analyzed by XRD diffractometry and did not show significant difference from the AlN thin film deposited on silicon substrate. For that reason, the Raman measurements were performed on the samples deposited on glass to avoid the strong Raman signal from silicon.

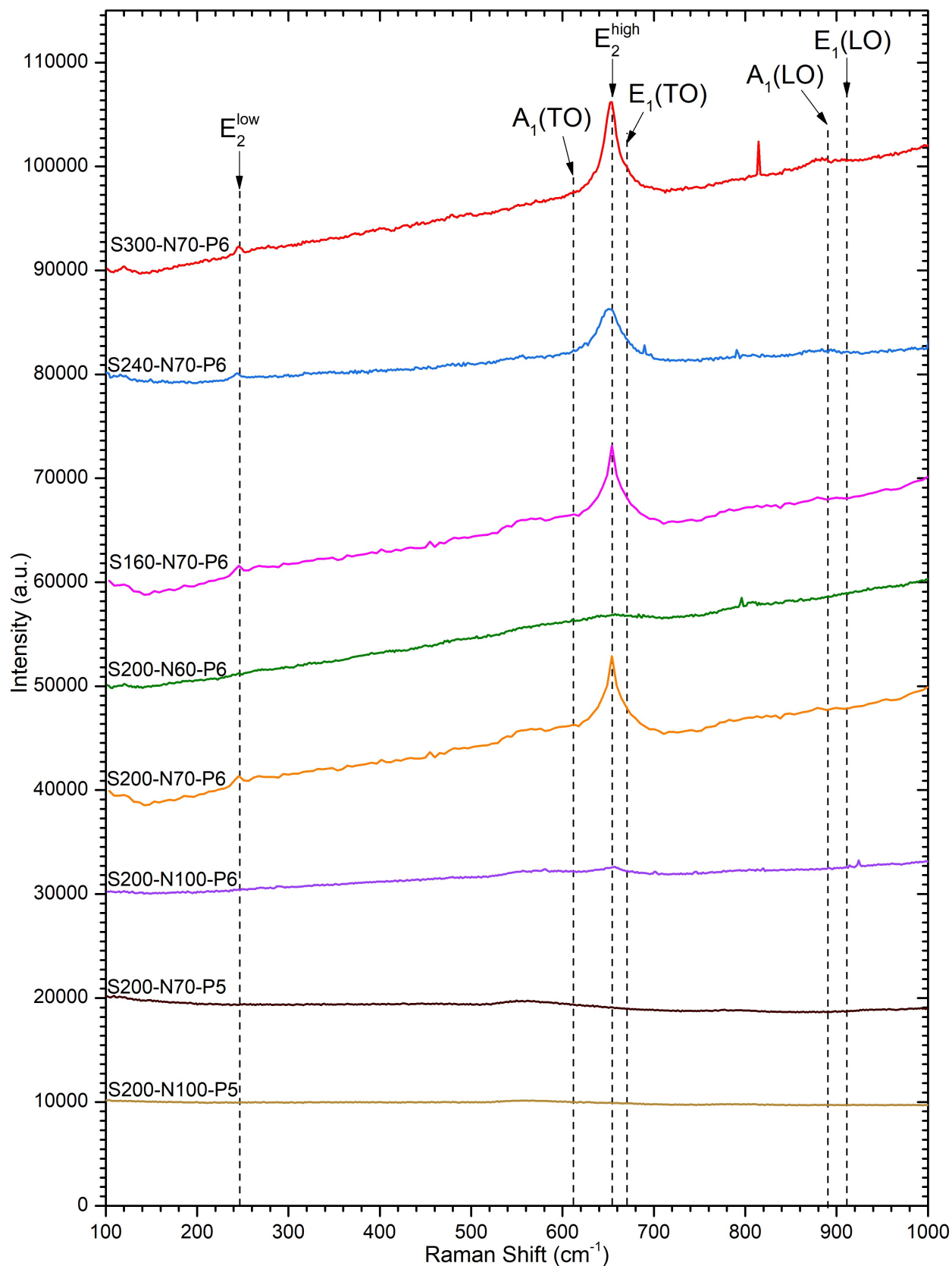


FIGURE 5.9 – Raman spectra of the aluminum nitride films varying deposition parameters, such as residual, initial temperature, nitrogen concentration and RF power.

TABLE 5.3 – Raman reference values of the  $E_2$  modes in  $cm^{-1}$ . (MCNEIL *et al.*, 1993) The  $E_2^{low}$ ,  $E_2^{high}$  and  $FWHM(E_2^{high})$  from Raman spectra of the AlN film varying deposition parameters.

Mode	$E_2^{low}$	$E_2^{high}$	$FWHM(E_2^{high})$
Reference Values	248	657	-
Samples			
S200-N100-P6	-	656	67
S200-N70-P6	245	654	16
S200-N60-P6	-	657	38
S160-N70-P6	245	653	17
S240-N70-P6	244	653	29
S300-N70-P6	244	652	20

The sample S200-N100-P5 and S200-N70-P5 did not present any peak in the Raman analyses indicating that the film growth in the sample S200-N100-P5 is amorphous and in the sample S200-N70-P5 are weakly ordered, as discussed in the previous section.

AlN films deposited at samples S200-N70-P6, S160-N70-P6, S240-N70-P6 and S300-N70-P6 presented apparent AlN characteristic peaks  $E_2^{high}$  at  $657\text{ cm}^{-1}$  and  $E_2^{low}$  at  $248\text{ cm}^{-1}$ . The intensity of  $E_2$  peaks define that the deposited film is preferably h-(002) oriented AlN film. So, the broadening of while  $E_2$  peak is attributed to the crystalline deterioration or intrinsic stress. The intensities of the  $E_2^{low}$  are very weak but are enough to determine the peak positions. The peak positions, for both  $E_2^{high}$  and  $E_2^{low}$ , presented very small left Raman shift ( $4\text{ cm}^{-1}$ ) from the reference value indicating that the deposited AlN films are crystalline and with low content of impurities, as observed by the XRD analysis. However, the peak intensities, mainly for  $E_2^{high}$ , presented a more pronounced difference, which can be associated with the film thickness that is different for each film. On the other hand, this small variation in the intensities of the peaks and peak position shift can also be related with the presence of residual tensile stress on the film due to ion bombardment of the film surface caused by the RF power applied during the deposition process, once the other parameters were the same for the four samples. The increase of applied RF improves the growth of well oriented AlN films as shown by the quality of the  $E_2^{high}$  peaks, except for the case of sample S240-N70-P6.

XRD analysis showed that the AlN film deposited on sample S240-N70-P6 has large crystallites that are related to the presence of large coherent scattering domain. The FEG-SEM micrograph of the surface of this film, Figure 5.8, also shows the presence of large grain indicating that the film was grown with certain degree of freedom in the planar

directions, which corroborates with the large crystallites size calculated. Then, the reason why the  $E_2^{high}$  peak for this film presented large FWHM ( $29\text{cm}^{-1}$ ) compared with 16, 17 and  $20\text{cm}^{-1}$  for the films of samples S200-N70-P6, S160-N70-P6 and S300-N70-P6, respectively, need to be better investigated.

The AlN films deposited on the samples S200-N100-P6 and S200-N60-P6 only presented a small a protuberance in the region of  $E_2^{high}$ . However, as illustrated in Figure 4.6, the absence of a peak for materials that already show to be crystalline by the XRD diffractogram may be associated with crystal polymorphism. These films were grown at gas mixture containing 60 and 100% of nitrogen, respective, and need more investigation to determine the presence of AlN polymorph crystal at deposition in low (60%) and very high (100%) nitrogen concentration.

## 5.4 Variable Angle Spectroscopic Ellipsometry - VASE

The analysis of the data obtained by VASE was performed using a structural model that describes the type of substrate. To study the deposited AlN thin films in this work were used two structural models depicted in Figure 5.10. The structural model 1, Figure 5.10-(a), is based in a Si (001) substrate with a dense AlN coating with thickness  $t_1$  and a very thin layer of thickness  $t_2$  of porous AlN (50% of AlN and 50% of void) to simulate the surface roughness, on top of it. The structural model 2, Figure 5.10-(b), consists of a Si (001) substrate with a dense AlN coating with thickness  $t_1$ , a layer of thickness  $t_2$  of a less dense AlN (80% of AlN and 20% of void) and a very thin layer of thickness  $t_3$  of porous AlN (50% of AlN and 50% of void) to simulate the surface roughness, on top of it.

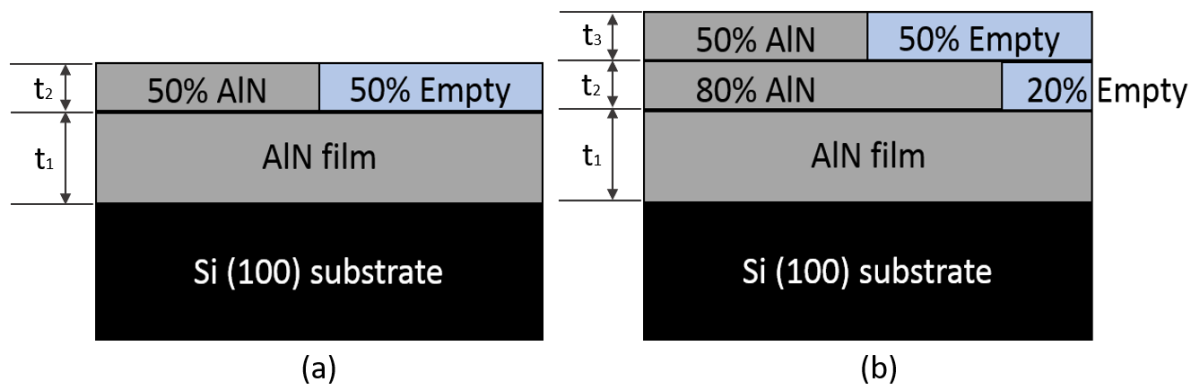


FIGURE 5.10 – Structural model applied in the spectroscopy of ellipsometry for samples (a)S200-N100-P6 to S240-N70-P6; (b) S300-N70-P6.

The structural model 1 was used to study the samples S200-N100-P6 to S240-N70-P6 and the structural model 2 to study the sample S300-N70-P6. As described in the previous section, the elevated amount of oxygen present on the composition of the AlN deposited on

samples S200-N100-P5 and S200-N70-P5, indicates that, in fact, it was grown amorphous oxynitride films as shown by the XRD and Raman analysis. For that reason, the two models presented here for the ellipsometry analysis do not fit well this material and these results will not be presented here.

All analyses of the ellipsometry spectra were obtained at the same conditions using photon energy range from 0.5 to 6.5 eV (UV to near IR - 2480 nm - 190 nm). Some samples presented a very high absorption at photon energy of about 5.5 eV.

Figure 5.11 presents the ellipsometric measured curves for  $I_s$  and  $I_c$ , as well as the curve fit for the structural model 1 for the AlN coatings deposited on samples S200-N100-P6 to S240-N70-P6 and structural model 2 for AlN deposited on sample S300-N70-P6 as function of the photon energy. This adaptation of structural model only to the sample S300-N70-P6 indicated that this sample presented a high roughness or non-uniform deposited film, which can explain the reason of the high peak of silicon in XRD analyses, once the diffraction analyzed more silicon in valleys between deposited AlN films than the other samples. The surface roughness and film thicknesses ( $t_1$ ,  $t_2$  and  $t_3$ ) measured by profilometry and ellipsometry technique are exposed in Table 5.4.

TABLE 5.4 – Ellipsometry data as thickness and roughness compared with profilometry techniques of the samples of AlN film varying deposition parameters.

Samples	Thickness		Roughness		
	Profilometry	Ellipsometry	Profilometry	Ellipsometry	
	$t_p$ (nm)	$t_T$ (nm)	$R_q$ (nm)	$t_2$ (nm)	$t_3$ (nm)
S200-N100-P5	595±20	797±10	71±13	9±1	-
S200-N70-P5	785±10	1305±29	83±35	13±1	-
S200-N100-P6	712±42	775±19	111±8	23±1	-
S200-N70-P6	1410±89	1228±23	142±17	19±1	-
S200-N60-P6	1277±67	1143±17	173±28	25±1	-
S160-N70-P6	555±20	638±12	302±6	19±1	-
S240-N70-P6	1823±28	1616±29	84±11	21±1	-
S300-N70-P6	1833±56	2021±53	244±18	11±2	23±2

The bandgap energy ( $E_g$ ) from the fitting and through Tauc-Lorentz method and the  $\chi^2$  error obtained from the curves fittings are also summarized in Table 5.5.

As the deposited AlN films are quite thick (650 to 1850 nm) the ellipsometry spectra present a large number of interference fringes. Adding to that, most of the AlN films start to present an important absorption for photon energy greater than 4.5 eV, which makes relatively difficult to obtain a good fit with the described structural and mathematical models. For that reason, the obtained  $\chi^2$  error values (58 - 153) were relatively high compared with the values (3.2 - 4.3) described in the literature. (KHAN *et al.*, 2015)

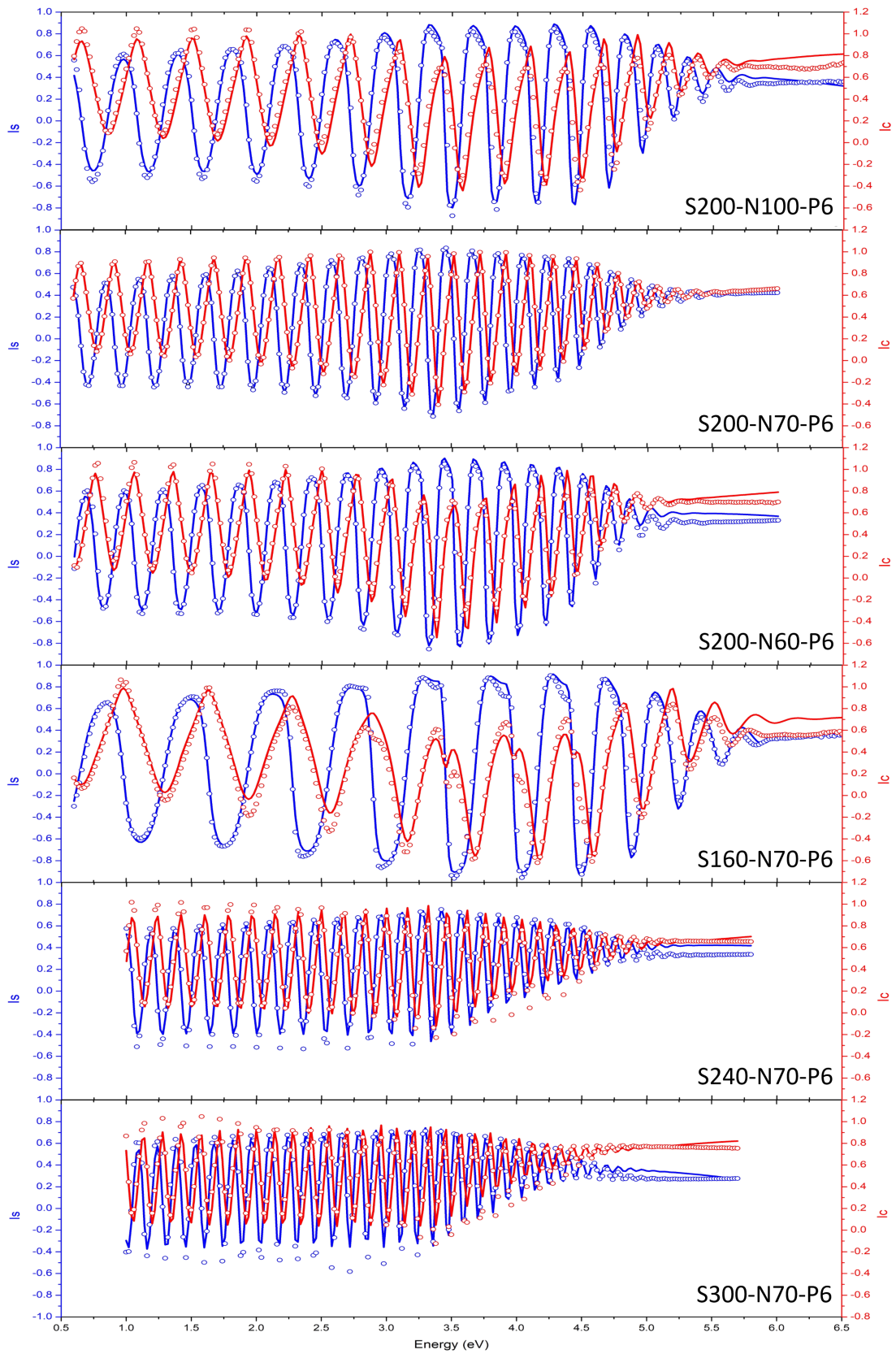


FIGURE 5.11 – Spectroscopic ellipsometry experimental data measured  $I_s$  (blue symbols) and  $I_c$  (red symbols) with the curve fit (lines) versus the energy for the AlN films of samples S200-N100-P6 to S300-N70-P6.

TABLE 5.5 – Ellipsometry data from the spectra and mathematical model of the samples of AlN film varying deposition parameters.

Sample	$\chi^2$	n	Bandgap - Ellipsometry (eV)	Bandgap - Tauc-Lorentz (eV)
S200-N100-P6	153	2.15	4.85±0.08	6.15
S200-N70-P6	103	2.21	5.08±0.07	5.59
S200-N60-P6	58	2.08	5.20±0.04	5.48
S160-N70-P6	126	1.80	5.78±0.07	5.98
S240-N70-P6	81	2.28	4.57±0.08	5.47
S300-N70-P6	128	2.30	4.57±0.11	5.34

Nevertheless, most of the literature studies only analyze the spectra up to 2.3 and 4.0 eV, that means the region free of the film absorption. Even so, it was possible to obtain AlN properties values that are reasonably in agreement with the expected values.

The thickness and surface roughness values obtained by VASE for all AlN films analyzed have the same behavior of the measured values obtained by profilometry. It must be pointed out here that the deposition system does not have a rotating substrate holder, which implies that the film thickness presents some non-uniformity across its surface. This is evidenced during the profilometry measurement and the values presented here are the mean values of eight measurements at a different position on the sample surface. The VASE analysis was performed in only one point on the coating surface, which may naturally expect a small thickness difference that is added to the mathematical model fitting procedure.

Figure 5.12 presents the film thickness obtained by VASE and profilometry. Despite the above mentioned differences and simplicity of the used models, the results obtained by VASE have the same behavior of the results obtained by other methodologies.

The bandgap energy values obtained by VASE presented values relatively lower than the expected values ( $E_g = 5.9 - 6.2$  eV) for the AlN thin films. The main reason for that must be related with the mathematical model used that do not completely takes into account the effect of the film absorption for high photon energy ( $> 4.5 - 4.0$  eV) and then underestimating the bandgap energy values. This means that more work needs to be done in order to improve the mathematical model to reliably represent the deposited AlN thin films. The bandgap values obtained by the Tauc-Lorentz method Figure 5.13 presented values closer to the expected values for the AlN films, indicating that the grown AlN films are with good quality as already confirmed by the XRD and Raman analysis. For a better comparison, Figure 5.13 presents a plot with the bandgap energy obtained by VASE and Tauc-Lorentz method.

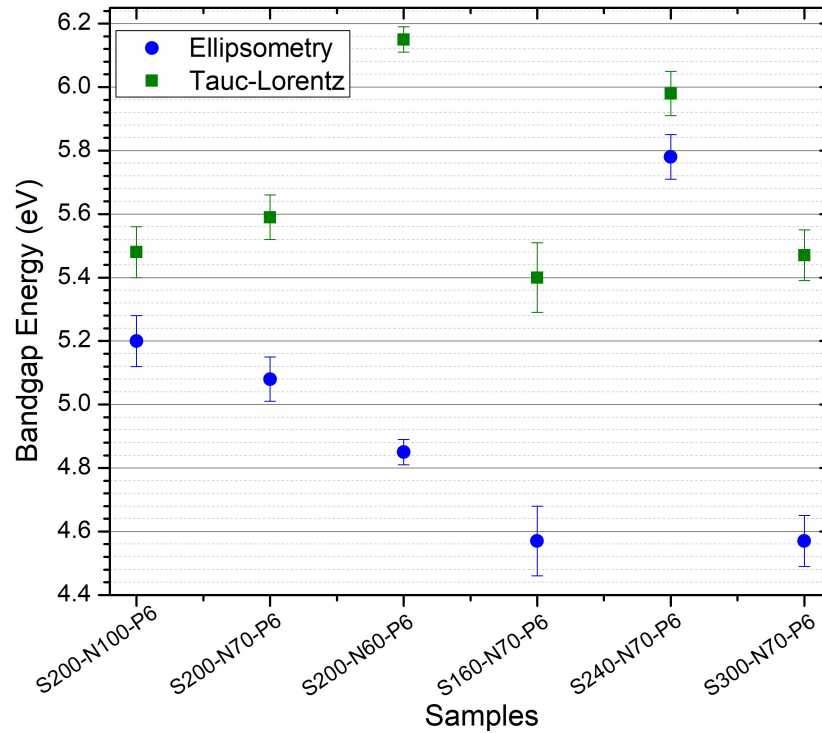


FIGURE 5.12 – Thickness comparison between profilometry and ellipsometry technique.

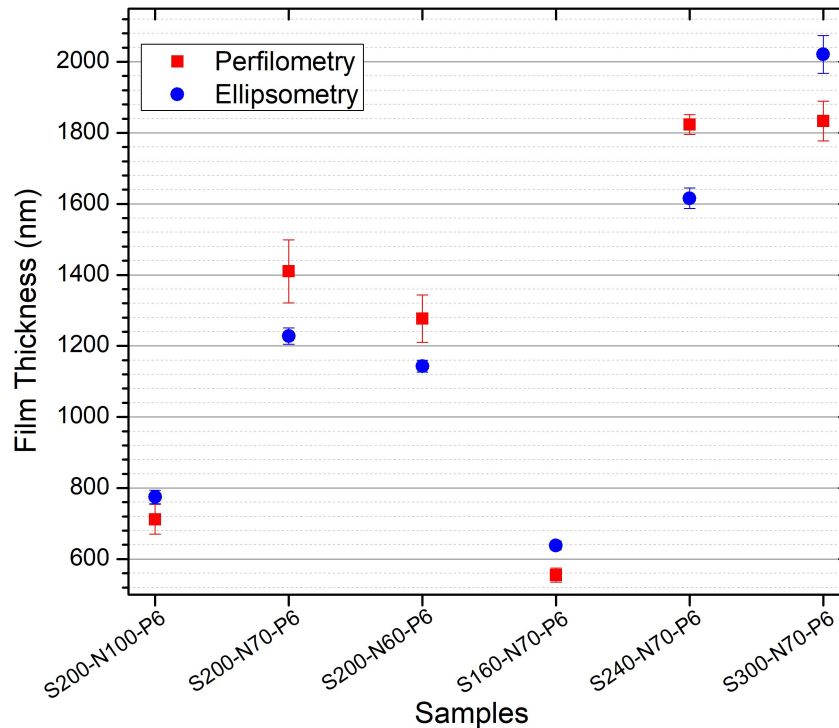


FIGURE 5.13 – Bandgap energy analyzing through the ellipsometry and the Tauc-Lorentz method.

Figure 5.14 presents the plot of the refractive index ( $n(\lambda)$ ) as function of the wavelength ( $\lambda$ ). The graphic presents the typical behavior of the refractive index. In most of the reference the refractive index ( $n$ ) is described in one standardized wavelength value (that

was defined for the red radiation with frequency  $f = 4.7376 \times 10^{14} Hz$  and wavelength  $\lambda = 623.8nm$ ). This wavelength is highlighted in Figures 5.14.

Then the obtained values for  $n$  at 632.8 nm for the AlN films deposited on the samples S200-N100-P6 to S300-N70-P6 are between 1.8 to 2.3, which are in good agreement with the values described in the literature (1.9 to 2.1). In the case of the  $n = 2.3$  for the sample S300-N70-P6, it may be overestimated due to the lack of good model fitting ( $\chi^2$  error of 128). Nevertheless, this range of values can be associated with the AlN films properties that were discussed in the XRD and Raman analysis that are mainly related with the structure and level of contamination of these films. The curves also show that the optical response of films grown by sputtering is strongly influenced by the structural disorder present either by amorphous regions or by grain boundaries or by stresses within the crystalline regions.

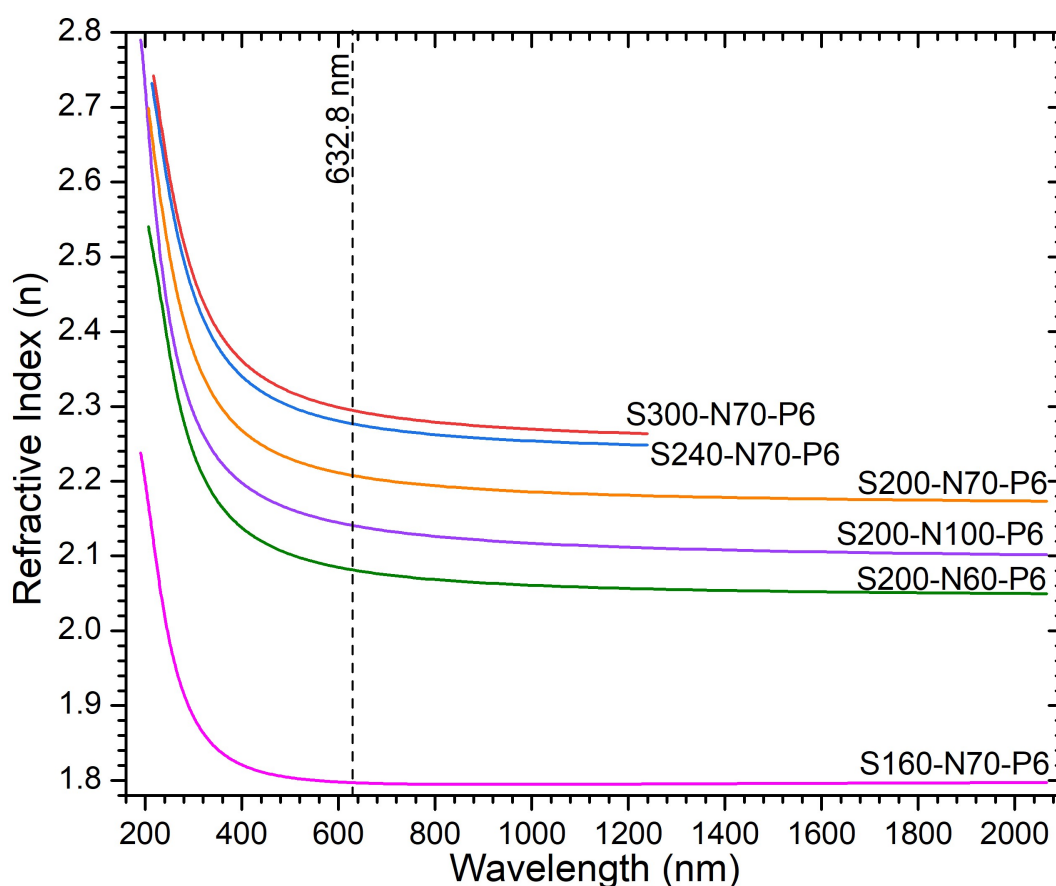


FIGURE 5.14 – Refractive index ( $n$ ) versus the wavelength for the AlN films of samples S200-N100-P6 to S300-N70-P6.

# Chapter 6

## Conclusions

In this work was reported a systematic study of the reactive sputtering process to deposit AlN thin films on (100) p-type silicon wafers aiming applications on surface acoustic wave sensors. Two conditions of residual pressures ( $5 \times 10^5$  Torr and  $2 \times 10^6$  Torr) in the plasma reactor were addressed in order to determine the sensibility of the contaminating in the formation of crystalline AlN films. The deposition at these two conditions with different nitrogen content in the gas mixture and different RF plasma power was well succeeded and the best conditions for deposition of crystalline AlN films for SAW applications were determined.

All AlN thin films deposited on the condition of high residual pressure presented high oxygen content ( $> 30\%$ ) indicating that the deposited films are an oxynitride film instead of aluminum nitride. These films presented an amorphous structure which is not desirable for applications in SAW devices.

All films deposited at lower residual pressure in the plasma reactor presented composition of AlN with lower content of oxygen ( $< 3\%$ ) and were crystalline presenting hexagonal wurtzite structure with preferential orientation (002).

The nitrogen content in the gas mixture does not affect the crystallinity of the deposited films, however, high nitrogen content (100%) reduce at about 50% the deposition rate of the AlN due to the target poisoning. 70% of nitrogen in the gas mixture proved to be the favorable condition to deposit well oriented hexagonal crystalline AlN with high deposition rate for the temperature and target to substrate distance used.

The crystalline structures were improved with the increase of the RF power applied in the range of 160 to 300W. The coating thickness and the surface roughness also increase with the increase of the RF power.

The refractive index,  $n$ , values for the crystalline AlN films obtained by spectroscopic ellipsometry are in good agreement and also in agreement with the values described in

the literature. The values of  $n$  increase with the increase of the applied RF power, that is, increase with the crystallinity improvement.

The bandgap energy obtained by spectroscopic ellipsometry is slightly lower than the values obtained by the Tauc-Lorentz method. This difference is related to the relatively poor quality of the curve fitting between the experimental data and the mathematical model used. Although the mathematical model takes into account a theoretical absorption of the AlN thin films for photon energy greater than 4.5 eV the structural and/or the mathematical model must be improved.

## 6.1 Future Directions

Despite the good results obtained in this work, there are some works to be done, in order to clarify some points aiming the improvement of the deposition methodology for AlN thin films as well as, for its characterization. Among then we have the need of:

- To investigate other parameters of thin film deposition such as working pressure, deposition temperature and the effect of the AlN film annealing after the deposition;
- Characterization of the deposited AlN film by XPS and RBS to see the real chemical composition;
- More work in the spectroscopic ellipsometry model to take into account the absorption model;
- Build SAW devices to test the piezoelectric properties of the films.

# Bibliography

ADACHI, H.; WASA, K.; KANNO, I.; KOTERA, H. **Handbook of sputter deposition technology : fundamentals and applications for functional thin films, nano-materials and MEMS**. [S.l.]: William Andrew, 2012. ISBN 9781437734836.

ADACHI, S. **Properties of Group-IV,III-V and II-VI Semiconductors**. Chichester: British Library, 2005. ISSN 9780470743690 0470743697. ISBN 0470090324.

AISSA, K. A.; ACHOUR, A.; ELMAZRIA, O.; SIMON, Q.; ELHOSNI, M.; BOULET, P.; ROBERT, S.; DJOUADI, M. A. AlN films deposited by dc magnetron sputtering and high power impulse magnetron sputtering for SAW applications. **J. Phys. D. Appl. Phys.**, IOP Publishing, v. 48, n. 14, p. 145307, 2015. ISSN 13616463.

AKASAKI, I.; AMANO, H. Crystal Growth and Conductivity Control of Group III Nitride Semiconductors and Their Application to Short Wavelength Light Emitters. **Jpn. J. Appl. Phys.**, IOP Publishing, v. 36, n. Part 1, No. 9A, p. 5393–5408, sep 1997. ISSN 0021-4922.

ALRASHDAN, M. H.; HAMZAH, A. A.; MAJLIS, B. Y.; AZIZ, M. F. Aluminum nitride thin film deposition using DC sputtering. **IEEE Int. Conf. Semicond. Electron. Proceedings, ICSE**, p. 72–75, 2014.

BRAY, R. C.; JOHNSEN, C. A.; BOGWELL, T. L.; ISHAK, W. S. **Polyimide damper for surface acoustic wave device**. 1987.

BRITO, F. S. **Fabricação e Caracterização de Sensores Baseados em Ondas Acústicas de Superfície**. 104 p. Tese (Dissertação de mestrado) — Instituto Tecnológico de Aeronáutica, 2014.

BUMBRAH, G. S.; SHARMA, R. M. Raman spectroscopy - Basic principle, instrumentation and selected applications for the characterization of drugs of abuse. **Egypt. J. Forensic Sci.**, v. 6, p. 209–215, 2015.

CHANG, S.-L. **Multiple diffraction of x-rays in crystals**. [S.l.]: Springer-Verlag, 1984. 300 p. ISBN 3540129553.

CHEN, L. xian; LIU, H.; LIU, S.; LI, C. ming; WANG, Y. chao; AN, K.; HUA, C. yi; LIU, J. long; WEI, J. jun; HEI, L. fu; LV, F. xiu. Growth of high quality AlN films on CVD diamond by RF reactive magnetron sputtering. **Appl. Surf. Sci.**, Elsevier B.V., v. 431, p. 152–159, 2018. ISSN 01694332.

- CHENG, C.; CHEN, Y.; WANG, H.; CHEN, W. Low-temperature growth of aluminum nitride thin films on silicon by reactive radio frequency magnetron sputtering. **J. Vac. Sci. Technol. A Vacuum, Surfaces, Film.**, v. 14, n. 4, p. 2238–2242, jul 1996. ISSN 0734-2101.
- CLEMENT, M.; VERGARA, L.; SANGRADOR, J.; IBORRA, E.; SANZ-HERVÁS, A. SAW characteristics of AlN films sputtered on silicon substrates. **Ultrasonics**, Elsevier, v. 42, n. 1-9, p. 403–407, apr 2004. ISSN 0041-624X.
- COTTON, F. A.; WILKINSON, G. W. **Advanced Inorganic Chemistry: A Comprehensive Text**. 1972. 657–669 p.
- COVACEVICE, A. C. T. **Sensores baseados em ondas acústicas : introdução e aplicações**. 57 p. Tese (Doutorado) — Universidade Estadual de Campinas, 2012.
- CULLITY, B. **Elements of X-RAY DIFFRACTION Second Edition**. [S.l.]: Addison, 1978. 569 p. ISSN 03207102. ISBN 0-201-01174-3.
- DAVYDOV, V. Y.; KITAEV, Y. E.; GONCHARUK, I.; SMIRNOV, A.; GRAUL, J.; SEMCHINOVA, O.; UFFMANN, D. Phonon dispersion and Raman scattering in hexagonal GaN and AlN. **Phys. Rev. B - Condens. Matter Mater. Phys.**, v. 58, n. 19, p. 12899–12907, 1998. ISSN 1550235X.
- DUARTE, D. A. **Crescimento de Filmes Finos de Dióxido de Titânio por Sistemas Magnetron Sputtering**. 141 p. Tese (Dissertação de Mestrado) — Instituto Tecnológico de Aeronáutica, 2010.
- DUQUENNE, C.; POPESCU, B.; TESSIER, P. Y.; BESLAND, M. P.; SCUDELLER, Y.; BRYLINSKI, C.; DELAGE, S.; DJOUADI, M. A. Magnetron sputtering of aluminium nitride thin films for thermal management. **Plasma Process. Polym.**, v. 4, n. SUPPL.1, p. 1–5, 2007. ISSN 16128869.
- EDGAR, J. H. **Properties of group III nitrides**. London: INSPEC, Institution of Electrical Engineers, 1994. 302 p. ISBN 0852968183.
- EIRAS, J. A. **Materiais Piezoelétricos**. Tese (Doutorado) — UFSCar, São Carlos, 2004.
- ELMAZRIA, O.; BÉNÉDIC, F.; El Hakiki, M.; MOUBCHIR, H.; ASSOUAR, M.; SILVA, F. Nanocrystalline diamond films for surface acoustic wave devices. **Diam. Relat. Mater.**, Elsevier, v. 15, n. 2-3, p. 193–198, feb 2006. ISSN 0925-9635.
- FILIPPIDIS, L.; SIEGLE, H.; HOFFMANN, A.; THOMSEN, C.; KARCH, K.; BECHSTEDT, F. Raman Frequencies and Angular Dispersion of Polar Modes in Aluminum Nitride and Gallium Nitride. **Phys. status solidi**, v. 198, n. 2, p. 621–627, dec 1996. ISSN 03701972.
- FIREK, P.; WÁSKIEWICZ, M.; STONIO, B.; SZMIDT, J. Properties of AlN thin films deposited by means of magnetron sputtering for ISFET applications. **Mater. Sci. Pol.**, v. 33, n. 4, p. 669–676, 2015. ISSN 2083134X.
- FITZ, T. **Ion nitriding of aluminium**. 115 p. Tese (Dissertation) — Universitat Dresden, 2002.

- FU, Y.; LUO, J.; NGUYEN, N.; WALTON, A.; FLEWITT, A.; ZU, X.; LI, Y.; MCHALE, G.; MATTHEWS, A.; IBORRA, E.; DU, H.; MILNE, W. Advances in piezoelectric thin films for acoustic biosensors, acoustofluidics and lab-on-chip applications. **Prog. Mater. Sci.**, v. 89, p. 31–91, aug 2017. ISSN 00796425.
- GEROVA, E.; IVANOV, N.; KIROV, K. Deposition of AlN thin films by magnetron reactive sputtering. **Thin Solid Films**, Elsevier, v. 81, n. 3, p. 201–206, jul 1981.
- GUPTA, M. N.; SUMAN; YADAV, S. K. **Electricity Generation Due to Vibration of Moving Vehicles Using Piezoelectric Effect**. 2014.
- HORIBA, J. Y. **Elipsometria - Google Drive**. [S.l.: s.n.], 2008. 294 p.
- HRIBŠEK, M. F.; TOŠIĆ, D. V.; RADOSAVLJEVIĆ, M. R. Surface Acoustic Wave Sensors in Mechanical Engineering. **FME Trans.**, v. 38, p. 8, 2010.
- IBORRA, E.; OLIVARES, J.; CLEMENT, M.; VERGARA, L.; SANZ-HERVÁS, A.; SANGRADOR, J. Piezoelectric properties and residual stress of sputtered AlN thin films for MEMS applications. **Sensors Actuators A Phys.**, Elsevier, v. 115, n. 2-3, p. 501–507, sep 2004. ISSN 0924-4247.
- ICHIKAWA, R. U. **Aplicações do Método de Warren-Averbach de Análise de Perfis de Difração**. 108 p. Tese (Dissertation) — IPEN, 2013.
- INTERRANTE, L. V.; LEE, W.; MCCONNELL, M.; LEWIS, N.; HALL, E. Preparation and Properties of Aluminum Nitride Films Using an Organometallic Precursor. **J. Electrochem. Soc.**, v. 136, n. 2, p. 472–478, 1989. ISSN 19457111.
- IRIARTE, G.; RODRÍGUEZ, J.; CALLE, F. Synthesis of c-axis oriented AlN thin films on different substrates: A review. **Mater. Res. Bull.**, Pergamon, v. 45, n. 9, p. 1039–1045, sep 2010. ISSN 0025-5408.
- IWATA, S.; NANJO, Y.; OKUNO, T.; KURAI, S.; TAGUCHI, T. Growth and optical properties of AlN homoepitaxial layers grown by ammonia-source molecular beam epitaxy. **J. Cryst. Growth**, North-Holland, v. 301-302, p. 461–464, apr 2007. ISSN 0022-0248.
- JOO, H. Y.; KIM, H. J.; KIM, S. J.; KIM, S. Y. Optical and structural properties of AlN thin films characterized by spectroscopic ellipsometry. **Thin Solid Films**, v. 368, n. 1, p. 67–73, 2000. ISSN 00406090.
- KANG, Y.; QIU, Y.; LEI, Z.; HU, M. An application of Raman spectroscopy on the measurement of residual stress in porous silicon. **Opt. Lasers Eng.**, v. 43, n. 8, p. 847–855, aug 2005.
- KHAN, S.; SHAHID, M.; MAHMOOD, A.; SHAH, A.; AHMED, I.; MEHMOOD, M.; AZIZ, U.; RAZA, Q.; ALAM, M. Texture of the nano-crystalline AlN thin films and the growth conditions in DC magnetron sputtering. **Prog. Nat. Sci. Mater. Int.**, Elsevier, v. 25, n. 4, p. 282–290, 2015. ISSN 10020071.
- KIM, S.; VEDAM, K. Simultaneous determination of dispersion relation and depth profile of thorium fluoride thin film by spectroscopic ellipsometry. **Thin Solid Films**, Elsevier, v. 166, p. 325–334, dec 1988. ISSN 0040-6090.

- KIRSCHNER, J. **Surface Acoustic Wave Sensors (SAWS): Design for Application**. [S.l.], 2010.
- KUBALL, M.; HAYES, J. M.; SHI, Y.; EDGAR, J. H. Phonon lifetimes in bulk AlN and their temperature dependence. **Appl. Phys. Lett.**, American Institute of Physics, v. 77, n. 13, p. 1958–1960, sep 2000.
- KUMARI, N.; SINGH, A. K.; BARHAI, P. K. Study of Properties of AlN Thin Films Deposited by Reactive Magnetron Sputtering. **Int. J. Thin Film. Sci. Technol.**, v. 3, n. 2, p. 43–49, 2014. ISSN 2090-9519.
- LANGFORD, J. I.; CERNIK, R. J.; LOUËR, D.; IUCR. The breadth and shape of instrumental line profiles in high-resolution powder diffraction. **J. Appl. Crystallogr.**, International Union of Crystallography, v. 24, n. 5, p. 913–919, oct 1991.
- LANGFORD, J. I.; WILSON, A. J. C. Scherrer after sixty years: A survey and some new results in the determination of crystallite size. **J. Appl. Crystallogr.**, International Union of Crystallography (IUCr), v. 11, n. 2, p. 102–113, apr 1978. ISSN 0021-8898.
- LÓPEZ, J. L. M. V. Ferroelectricidad y piezoelectricidad. p. 1–19, 2016.
- LOSURDO, M.; HINGERL, K. **Ellipsometry at the nanoscale**. 1. ed. [S.l.]: Springer, 2013. 730 p. ISBN 9783642339561.
- LUGHI, V.; CLARKE, D. R. Defect and stress characterization of AlN films by Raman spectroscopy. **Appl. Phys. Lett.**, v. 89, n. 24, p. 241911, dec 2006. ISSN 0003-6951.
- MAHMOOD, A.; MACHORRO, R.; MUHL, S.; HEIRAS, J.; CASTILLON, F.; FARIAS, M.; ANDRADE, E. Optical and surface analysis of DC-reactive sputtered AlN films. **Diam. Relat. Mater.**, Elsevier, v. 12, n. 8, p. 1315–1321, aug 2003.
- MATSUMOTO, T.; KIUCHI, M. Zinc-blende aluminum nitride formation using low-energy ion beam assisted deposition. **Nucl. Instruments Methods Phys. Res. Sect. B Beam Interact. with Mater. Atoms**, North-Holland, v. 242, n. 1-2, p. 424–426, jan 2006. ISSN 0168-583X.
- MCNEIL, L. E.; GRIMSDITCH, M.; FRENCH, R. H. Vibrational Spectroscopy of Aluminum Nitride. **J. Am. Ceram. Soc.**, John Wiley Sons, Ltd (10.1111), v. 76, n. 5, p. 1132–1136, may 1993. ISSN 0002-7820.
- MEDEIROS, H. d. S. **Obtenção de Filmes Finos de SiC, SiCN e AlN por Magnetron Sputtering para Aplicação em Microsensores**. 136 p. Tese (Dissertação) — Instituto Tecnológico de Aeronáutica, 2012.
- MENG, W. J.; SELL, J. A.; PERRY, T. A.; EESLEY, G. L. Real time stress measurements and elastic constant of aluminum nitride thin films on Si(111). **J. Vac. Sci. Technol. A Vacuum, Surfaces, Film.**, American Vacuum Society, v. 11, n. 4, p. 1377–1382, jul 1993. ISSN 0734-2101.
- MONROY, E.; S, F. O.; CALLE, F. Wide-bandgap semiconductor ultraviolet photodetectors. **Semicond. Sci. Technol.**, IOP Publishing, v. 18, n. 4, p. R33–R51, apr 2003. ISSN 0268-1242.

- MOURA, J. A. d. S. **Filmes Nanométricos de FeN e AlN Crescidos por Sputtering e Aplicações do Efeito Peltier**. 147 p. Tese (Doutorado) — Universidade Federal do Rio Grande do Norte, 2010.
- NAKAMURA, S. In Situ Monitoring of GaN Growth Using Interference Effects. **Jpn. J. Appl. Phys.**, IOP Publishing, v. 30, n. Part 1, No. 8, p. 1620–1627, aug 1991. ISSN 0021-4922.
- NANOPHOTON. What is Raman Spectroscopy? | Nanophoton. 2018.
- NOYAN, I. C.; COHEN, J. B. **Residual Stress: Measurement by Diffraction and Interpretation**. New York, NY: Springer New York, 1987. 247 p. ISBN 978-1-4613-9571-3.
- NOYAN, M. A. Fabrication and Characterization of Zinc Oxide Based Surface Acoustic Wave Devices. 2013.
- OLIVEIRA, I. C. **Estudo das propriedades de filmes finos de nitreto de alumínio produzidos por processo de âmagnetron sputtering em regimes contínuo (DC) e alternado (RF)**. 2004. 126 p. Tese (Doutorado) — Instituto Tecnológico de Aeronáutica (ITA), 2004.
- OLIVEIRA, I. C.; OTANI, C.; MACIEL, H. S.; NODA, L. K.; TEMPERINI, M. L. A. Raman active E2 modes in aluminum nitride films. **J. Mater. Sci. Mater. Electron.**, v. 2, n. 2, p. 5–9, 2001.
- PASTRÁK, J.; ROSKOVCOVÁ, L. Optical Absorption Edge of AlN Single Crystals. **Phys. Status Solidi**, John Wiley Sons, Ltd, v. 26, n. 2, p. 591–597, jan 1968. ISSN 03701972.
- PELEGRINI, M.; ALVARADO, M.; ALAYO, M.; PEREYRA, I. Deposition and characterization of AlN thin films obtained by radio frequency reactive magnetron sputtering. **Can. J. Phys.**, NRC Research Press, v. 92, n. 7/8, p. 940–942, jul 2014. ISSN 0008-4204.
- PELEGRINI, M. V. **Estudo de materiais piezoelétricos da família iii-v obtidos por sputtering reativo visando sua aplicação em sensores e mems**. 128 p. Tese (Dissertação) — USP, 2010.
- PELEGRINI, M. V.; PEREYRA, I. Characterization of AlN films deposited by r.f. reactive sputtering aiming MEMS applications. **Phys. status solidi**, p. NA–NA, feb 2010. ISSN 18626351.
- PERLIN, P.; POLIAN, A.; SUSKI, T. Raman-scattering studies of aluminum nitride at high pressure. **Phys. Rev. B**, American Physical Society, v. 47, n. 5, p. 2874–2877, feb 1993.
- PHILLIPS, J. C. Ionicity of the Chemical Bond in Crystals. **Rev. Mod. Phys.**, American Physical Society, v. 42, n. 3, p. 317–356, jul 1970. ISSN 0034-6861.
- PIERSON, H. O. **Handbook of refractory carbides and nitrides : properties, characteristics, processing, and applications**. [S.l.]: Noyes Publications, 1996. 340 p. ISBN 9780815513926.

QUAY, R. **Gallium Nitride Electronics**. Freiburg: Springer, 2007. 470 p. ISBN 9783540718925.

ROBATTO, L. B. **Residual Stress Heterogeneity Assessment of High Performance Powder Metallurgy Gears**. 101 p. Tese (Dissertation) — Instituto Tecnológico de Aeronáutica, 2017.

RODRÍGUEZ-CLEMENTE, R.; ASPAR, B.; AZEMA, N.; ARMAS, B.; COMBESCURE, C.; DURAND, J.; FIGUERAS, A. Morphological properties of chemical vapour deposited AlN films. **J. Cryst. Growth**, North-Holland, v. 133, n. 1-2, p. 59–70, oct 1993. ISSN 0022-0248.

SATO, A.; AZUMADA, K.; ATSUMORI, T.; HARA, K. Characterization of AlN:Mn thin film phosphors prepared by metalorganic chemical vapor deposition. **J. Cryst. Growth**, North-Holland, v. 298, p. 379–382, jan 2007. ISSN 0022-0248.

SCIENCEDIRECT. **ScienceDirect.com | Science, health and medical journals, full text articles and books**. 2018. Disponível em: <<https://www.sciencedirect.com/>>.

SMITH, E.; DENT, G. **Modern Raman spectroscopy : a practical approach**. [S.l.]: Wiley, 2005. ISBN 1118681320.

STRITE, S. GaN, AlN, and InN: A review. **J. Vac. Sci. Technol. B Microelectron. Nanom. Struct.**, v. 10, n. 4, p. 1237, 1992. ISSN 0734211X.

SURESH, A.; MUTH, J. F. Bias stress stability of indium gallium zinc oxide channel based transparent thin film transistors. **Appl. Phys. Lett.**, v. 92, n. 3, 2008. ISSN 00036951.

TOMPKINS, H. G.; IRENE, E. A.; HILL, C.; CAROLINA, N. **Handybook of Ellipsometry**. 1. ed. Norwich: Springer, 2005. 870 p. ISBN 0815514999.

TROLIER-MCKINSTRY, S.; MURALT, P. Thin Film Piezoelectrics for MEMS. **J. Electroceramics**, Kluwer Academic Publishers, v. 12, n. 1/2, p. 7–17, jan 2004. ISSN 1385-3449.

TSUBOUCHI, K.; MIKOSHIBA, N. Zero-Temperature-Coefficient SAW Devices on AlN Epitaxial Films. **IEEE Trans. Sonics Ultrason.**, v. 32, n. 5, p. 634–644, sep 1985. ISSN 0018-9537.

VENKATARAJ, S.; SEVERIN, D.; DRESE, R.; KOERFER, F.; WUTTIG, M. Structural, optical and mechanical properties of aluminium nitride films prepared by reactive DC magnetron sputtering. **Thin Solid Films**, Elsevier, v. 502, n. 1-2, p. 235–239, apr 2006.

WANG, J.; CHEN, D.; XU, Y.; LIU, Q.; ZHANG, L. Influence of the Crystal Texture on Raman Spectroscopy of the AlN Films Prepared by Pulse Laser Deposition. **J. Spectrosc.**, v. 2013, p. 1–6, 2013. ISSN 2314-4920.

WARREN, B. X-ray studies of deformed metals. **Prog. Met. Phys.**, Pergamon, v. 8, p. 147–202, jan 1959.

WEIGEL, R.; MORGAN, D.; OWENS, J.; BALLATO, A.; LAKIN, K.; HASHIMOTO, K.; RUPPEL, C. Microwave acoustic materials, devices, and applications. **IEEE Trans. Microw. Theory Tech.**, v. 50, n. 3, p. 738–749, mar 2002. ISSN 00189480.

WHITE, R. M.; VOLTMER, F. W. Direct Piezoelectric Coupling to Surface Elastic Waves. **Appl. Phys. Lett.**, American Institute of Physics, v. 7, n. 12, p. 314–316, dec 1965. ISSN 0003-6951.

WRIGHT, A. F. Elastic properties of zinc-blende and wurtzite AlN, GaN, and InN. **J. Appl. Phys.**, American Institute of Physics, v. 82, n. 6, p. 2833, aug 1998. ISSN 0021-8979.

XU, X. H.; WU, H. S.; ZHANG, C. J.; JIN, Z. H. Morphological properties of AlN piezoelectric thin films deposited by DC reactive magnetron sputtering. **Thin Solid Films**, v. 388, n. 1-2, p. 62–67, 2001. ISSN 00406090.

YODER, M. Wide bandgap semiconductor materials and devices. **IEEE Trans. Electron Devices**, v. 43, n. 10, p. 1633–1636, 1996. ISSN 00189383.

ZACHARIASEN, W. H. W. H. **Theory of X-ray diffraction in crystals**. [S.l.]: Dover Publications, 2004. 255 p. ISBN 9780486495675.

ZHANG, Y.; CHEN, D. **Multilayer integrated film bulk acoustic resonators**. [S.l.]: Springer, 2013. 152 p. ISBN 9783642317767.

## FOLHA DE REGISTRO DO DOCUMENTO

1. CLASSIFICAÇÃO/TIPO DM	2. DATA 07 de março de 2019	3. DOCUMENTO Nº DCTA/ITA/DM-011/2019	4. Nº DE PÁGINAS 95
5. TÍTULO E SUBTÍTULO: Deposition and Characterization of AlN Thin Films for Application in SAW Devices			
6. AUTORA(ES): <b>Lauren de Carvalho Leme</b>			
7. INSTITUIÇÃO(ÕES)/ÓRGÃO(S) INTERNO(S)/DIVISÃO(ÕES): Instituto Tecnológico de Aeronáutica – ITA			
8. PALAVRAS-CHAVE SUGERIDAS PELA AUTORA: AlN; Magnetron Sputtering; Plasma; SAW			
9. PALAVRAS-CHAVE RESULTANTES DE INDEXAÇÃO: Dispositivos de ondas acústicas superficiais; Filmes finos; Microscopia eletrônica; Pulverização por magnétron; Física.			
10. APRESENTAÇÃO: <span style="float: right;"><input checked="" type="checkbox"/> Nacional    <input type="checkbox"/> Internacional</span> ITA, São José dos Campos. Curso de Mestrado. Programa de Pós-Graduação em Física. Área Física de Plasmas. Orientador: Prof. Dr. Argemiro Soares da Silva Sobrinho. Defesa em 22/02/2019. Publicada em 2019.			
11. RESUMO: The present work reports the growth of aluminum nitride (AlN) thin film aiming its application in the manufacturing of microsensors devices based on surface acoustic waves (SAW). The AlN thin films were deposited on p-type silicon (100) substrate by radio frequency magnetron sputtering technique. The plasma parameters were varied in order to investigate the best plasma conditions to growth AlN thin films for application in SAW devices. The parameters explored were residual pressure, nitrogen concentration and applied RF power. These parameters had strong influence in the structure and composition of the deposited AlN films. The deposition rate and morphology were characterized by mechanical and optical profilometries and the field emission gun scanning electron microscopy, respectively. The deposition rate linearly increases with the increase of the RF power up to about 240W. For higher RF power the deposition rate presents a less accentuated increase probably due to the retro-sputtering of the growing film caused by the high energetic species impinging the film surface. High nitrogen content (100%) in the gas mixture decreases the deposition rate by about 50% due to the target poisoning and the absence of argon. The crystalline structures of the deposited AlN thin films were analyzed by X-ray diffraction, Raman spectroscopy and variable angle spectroscopic ellipsometry. The film crystallinity and composition are tightly influenced by the residual pressure in the deposition chamber due to the elevated concentration of impurities, mainly oxygen. The increase of the applied RF power favors the growth of well oriented h-(002) hexagonal wurtzite type structure. The refractive index values obtained are in good agreement with the values described in the literature and the values increase with the improvement of the AlN crystallinity, that occurs with the increasing of the applied RF power. The bandgap energies values obtained by ellipsometry was slightly low compared with the bandgap energy values obtained by the Tauc-Lorentz method that is closer to the values cited in the literature. This difference was caused by the lack of good mathematical and/or geometrical model fit. The AlN film with the best set of properties for SAW application was grown with lower residual pressure in the plasma chamber, gas mixture containing 70% of N <sub>2</sub> and an RF power of 240W.			
12. GRAU DE SIGILO: <input checked="" type="checkbox"/> OSTENSIVO <input type="checkbox"/> RESERVADO <input type="checkbox"/> SECRETO			